Università degli Studi di Cassino e del Lazio Meridionale
Corso di Dottorato in Metodi, Modelli e Tecnologie per l'Ingegneria
Dipartimento di Ingegneria Elettrica e dell'Informazione

Design and development of sensors, measurement systems, and measurement methods in the NDE 4.0 framework.

Alessandro Sardellitti

alessandro.sardellitti@unicas.it

In Partial Fulfillment of the Requirements for the Degree of

PHILOSOPHIAE DOCTOR in

Electrical and Information Engineering

16/01/2023

TUTORS
Prof. L. Ferrigno, Prof. A. Tamburrino

COORDINATOR
Prof. F. Marignetti

UNIVERSITÀ DEGLI STUDI DI CASSINO E DEL LAZIO MERIDIONALE

CORSO DI DOTTORATO IN METODI, MODELLI E TECNOLOGIE PER L'INGEGNERIA

Date: **16/01/2023**

Author: **Alessandro Sardellitti**

Title: **Design and development of sensors, measurement systems, and measurement methods in the NDE 4.0 framework.**

Department: **DIPARTIMENTO DI INGEGNERIA ELETTRICA E DELL'INFORMAZIONE**

Degree: **PHILOSOPHIAE DOCTOR**

Contents

List of Figures

List of Tables

Chapter 1

Introduction

Industry 4.0 represents the integration of advanced technologies, data analysis and real-time monitoring to transform manufacturing processes [1, 2].

In recent years, production processes have developed increasingly stringent quality standards and there is a growing need to carry out not just spot inspections, but continuous and comprehensive checks on the produced samples. Quality control methods ensure that metallic and composite products meets the specified parameters, minimizing variations and defects. The real strength lies in the early detection of defects; indeed, using IoT sensors, artificial intelligence and data analysis, deviations from design or project parameters can be quickly identified, preventing problems from arising and reducing waste [3].

Process optimization is crucial in this environment. Sensors accurately track factors such as temperature, pressure, composition and sample geometry during production, and subsequent data analysis leads to adjusted process parameters that produce optimal material properties and minimal defects.

Another important factor is predictive maintenance, it ensures the reliability of production machinery. Sensors and data analysis work together to predict maintenance needs, avoiding unplanned downtime that could interrupt production and compromise quality [4].

Industry 4.0's focus on efficient customization is based on quality inspection's ability to adapt processes to meet the unique requirements of samples while maintaining demanding quality standards. In this context, cost savings emerge as a natural consequence. Defect reduction, optimized processes and reduction of rejection rates translate to substantial savings that can be reinvested into process enhancements.

Essentially, quality control is the foundation of Industry 4.0. By merging advanced technologies and data analysis, manufacturers can not only meet stringent

quality requirements in the production of metallic and composite materials but also unlock efficiency, minimize defects and secure a competitive edge in the modern manufacturing scenario.

In the framework of quality control, Non-Destructive Testing and Evaluation (NDT&E) methods play a key role. The importance of NDT&E lies in its ability to detect defects, imperfections or irregularities that could compromise the performance of products or systems without altering the physical and chemical characteristics of the product being analyzed [5, 6]. Through the application of these methods, the integrity, safety and reliability of materials, components and structures is ensured.

Many parameters can be analyzed using these methods:

- geometrical parameters of the sample. For example, the thickness parameter is indicative of how the mechanical forming process is performing (such as pressing processes, rolling etc.) and determines the structural characteristics of the produced sample [7–9];
- parameters that define the chemical composition of the sample. For instance, the electrical conductivity determines the quality of the part in the molding (in the case of metallic materials) [10–12] and curing (in the case of composite materials) processes [13, 14];
- parameters that indicate the degradation of the sample, an example is the loss of material that occurs in the case of corrosion processes [15–17];
- the presence of superficial or subsurface cracks [18–20] or delamination [21, 22] that may occur during the production or working phase.

All these parameters determine the quality and remaining lifetime of the sample under analysis.

These issues have been studied within the NDE community for a long time and there are now many technologies and methodologies that provide good accuracy. The challenge that this research project aims to solve is to identify methodologies that are in line with the context of NDE 4.0. This context is made of very low-cost sensors, based on minimizing the use of human operators then with sensors integrated into automated measurement systems that can manage the measurement process and optimize measurement time and processing [23–25].

In conclusion, the challenge of the research project was to create sensors, measurement systems, and methodologies that have the purpose of applicability in the NDE 4.0 context.

In the first phase of the research project, the study of the geometric parameters of greatest interest in the industrial and research area was realized. In this context,

the thickness of metallic samples was observed to be an important parameter in the context of industrial quality control.

Thickness measurements have a key role in many industrial applications related to metallic plates because they provide information about the quality of both the manufacturing process and the realized product in term of structural strength and elasticity. These aspects are fundamental in all those application fields, such as in automotive, aerospace or civil, where the integrity of the metallic plates components has a direct impact on the safety of human beings.

Methods currently used in quality control in industry were studied; at the meantime, methods that showed the greatest potential in terms of measurement accuracy and integrability in automated measurement systems were identified.

In the actual industrial practice, some metrological checks are carried out by using touch-trigger probes [26]. These measurements are time-consuming and unsuitable for integration within the in-line and real-time quality control measurement systems. Other options concern laser-based measurement methods, we highlight that they allow in-situ measurements with very good measurement accuracies, but the higher cost of the instrumentation has a major impact on the overall product cost [27, 28]. Ultrasound methods are usually adopted in quality control procedures. These methods allow to obtain good measurement accuracies but they usually require the coupling materials (e.g. water, gel etc.) that impose an expensive procedure for cleaning the sample, the use of expensive measurement systems [7, 29–31] and the presence of qualified technicians to perform the test. All these aspects make this kind of test not suitable for inline thickness monitoring during the manufacturing phase. Several research groups are investigating the possibility offered by Eddy-Current (EC) methods, which typically assure low costs, simple probes, and easy integration to online, real-time, and automated measurement systems.

Inside the broad field of the EC methods proposed in the literature, there are several methods that allow the estimation of thickness by means of a multi-frequency analysis [7–9, 32–34] or pulsed eddy current analysis [35–37].

In particular, in [32–34], Yin *et al.* proposed and optimized measurement probes and processing algorithms suitably developed for non-magnetic materials able to give accuracy compatible with industrial quality standards and a good robustness to lift-off variations. In detail, using different combinations of coils to perform the generation and detection of the excitation and reaction magnetic flux respectively, Yin *et al.* compared measurements performed both in air and on the sample under test to estimate the thickness of planar samples. Although the methods proposed [32–34] appear to be promising, they have some limitations in terms of applicability in the aforementioned context of real-time, in-line measurements with good,

constant measurement accuracy over the entire range of thicknesses analyzed.

Firstly, the method proposed in [32] is highly efficient, but it relies on the constancy of a certain parameter (α_0). Unfortunately, as discussed in next Sections, this parameter is highly dependent on the thickness of the analyzed metallic plates, and it can be maintained constantly only asymptotically for thicknesses much smaller than the size of the eddy current probe. This makes the method not applicable for thick samples or in the presence of curved surfaces. For instance, in the latter case, there are two main constraints: *(i)* the probe has to be much larger than the thickness of the samples and *(ii)* the probe has to be much smaller than the curvature of the samples, to approximate the surface of the sample by means of its tangent plane, in a neighborhood of the probe itself.

Secondly, in [32–34], the key feature for estimating the thickness of plates is the value of the frequency where a proper quantity achieves its minimum value ($\Delta R/\omega$). To get proper accuracy in measuring the thickness of the sample under test, this minimum needs to be located in an accurate manner. In turn, this requires several measurements at different frequencies with high frequency resolution which makes the approach time-consuming and not suitable for almost real-time applications.

In order to solve the first limitation, in [38, 39] was provided a deep, complete, and more general theoretical framework for the method proposed in [32], allowing it to be extended to a broader class of thickness measurements. From the technical perspective, it was proved that the critical constant parameter α_0 has to be replaced by a new function $\alpha = \alpha(\Delta)$, which depends on the thickness (Δ). With this "minimal" modification, the method's range of applicability was extended while identifying its underlying physical limit. Two algorithms were developed to make the optimal use of the identified variable $\alpha = \alpha(\Delta)$. The first algorithm is iterative and is conceived for applications where the unknown thickness ranges from 0 up to the theoretical limit of the method. The second algorithm is based on a polynomial approximation of $\alpha(\Delta)$ and provides the thickness as the solution of an algebraic equation of the same degree as the approximating polynomial.

For the second limitation, in [40] was proposed a strategy with a multi-tone and interpolation combination. In particular, a multisine excitation signal approach was applied to collect the data onto a proper set of frequencies then appropiate techniques were applied in order to interpolate the data at all the frequencies required to locate accurately the minimum of the response. The combination of the multisine signal to allocate efficiently the measurement frequencies with the data interpolation results in a reduction of the number of required measurements and, in the ultimate analysis, of the overall measurement time. Specifically, the measurement time for a typical situation was reduced from 13 to 2.66 seconds with a similar level of accuracy to that represented in [32].

For the optimization proposed in [38–40], in view of its applicability in an industrial context, a patent application was also submitted [41].

From the knowledge acquired during the first part of the research project, in the second part, more attention was paid to the variables that usually influence the estimation of thickness and in general in the context of NDT&E.

Problems related to NDT&E typically involve several variables. As a matter of fact, the result of an NDT&E test depends on *(j)* the probe's parameters (geometry, materials, ...), *(jj)* the geometrical and the physical characteristics of the sample under testing (e.g. thickness, electrical conductivity, magnetic permeability etc.) and *(jjj)* the parameters describing the geometrical relationship between the probe and the sample under testing (e.g. lift-off, tilt angle etc.). From the experience gathered in this context [38–40], the number of variables involved and the correlated nature of these variables (e.g., excitation frequency or electrical conductivity and thickness of the sample) make an NDT&E problem difficult to handle.

To this purpose, a methodology that can systematically reduce the analysis complexity of the problems by decreasing the number of variables involved can play a very important role. For instance, this reduction of the number of variables has a major impact when a physical problem is modelled either via a numerical approach or via a machine learning approach [42–44]. In both cases, there is an exponential reduction in the number of required numerical simulations or the size of the training database.

In this context, dimensional analysis is a mathematical tool for analyzing problems involving physical quantities [45, 46]. Dimensional analysis can be used to simplify complex equations by highlighting the fundamental quantities that describe a problem. In particular, by analyzing only the physical dimensions of the variables involved in an equation, a smaller number of fundamental quantities describing the original problem can be determined. This simplifies the calculation of the solution to the original problem.

Among the various tools available, the Buckingham's π theorem represents a widely used tool in the literature [47–50]. It states that a certain physical relation of n variables can be rewritten in terms of p dimensionless parameters, defined as π groups, where $p = n - k$, with k number of physical dimensions involved [51].

This research activity brought the application of the Buckingham π theorem to the NDT&E community for the first time [52–54].

In addition to an initial study of the method's applicability in the context of NDT&E using ultrasonic methods, several advantages were also shown in the case study of the simultaneous estimation of the thickness and electrical conductivity of metallic materials. In particular:

- Buckingham's theorem makes it possible to reduce the number of variables to

be considered, thus leading to a reduction in the computational complexity of the problem;

- it makes it possible to establish the structure of the relationships existing between the variables involved;

- the proposed procedure is compatible with applications in which simultaneous estimation is required under on-line and real-time industrial conditions with excellent accuracy.

This specific application was chosen because the thickness estimation methods usually presented in the literature require a priori knowledge of the electrical conductivity of the metallic sample [32], which is not always known. In addition, the electrical conductivity of metallic material is a good feature to estimate the goodness of the heat treatment and it is related to mechanical characteristics such as hardness, toughness, and tensile strength [10–12].

In particular, the research activity has given to the NDT&E community these major contributions:

- a proper relationship in terms of dimensionless groups among the measured quantity and the physical variables affecting it, in a frequency domain EC experiment. It was assumed that the measured quantity is the self or mutual impedance of the probe. This assumption is not restrictive of the generality of the method;

- a method together with its algorithm counterpart for the simultaneous estimation of the thickness and electrical conductivity by using dimensionless groups;

- a versatile experimental set–up for the simultaneous estimation of the thickness and electrical conductivity, based on single-frequency or multi-frequency measurements.

Also in this activity, for the methods proposed and results shown in [52–54], in view of its suitability in an industrial context, a patent application was submitted [55].

It is useful to make a few brief remarks regarding the applicability of the two measurement systems and methods described previously.

The measurement systems suggested by optimizing Yin *et al.* techniques and employing dimensional analysis can be seen as complementary and can find suitable applications within industrial settings. Concerning the measurement system recommended through the optimization of Yin *et al.* methods, it allows for the

realization of a portable measurement system, as the analysis of metal samples can be conducted through experimental calibration.

On the other hand, the measurement system proposed by dimensional analysis entails an initial numerical simulation phase in which the boundaries are established. Consequently, this system also relies on the support of a numerical simulator. As a result, the measuring system could be tailored for use within an automated production facility.

In the final part of the project, a research activity was carried out in collaboration with the Sensors and NDT lab of the School of Electrical and Electronic Engineering of Newcastle University, Newcastle upon Tyne, United Kingdom.

The activity concerns the detection and characterization of atmospheric corrosion on mild steel materials [56]. Corrosion is a widespread problem in various industrial and civil environments. It refers to the deterioration of materials, usually metals, caused by chemical reactions with the surrounding environment [15–17]. It is a massive and costly problem that can lead to structural failure, safety hazards, environmental contamination and significant financial losses [57].

Early detection and characterization of corrosion are crucial in various sectors and applications for several reasons and they are the basis of the Structural Health Monitoring (SHM) concept [58, 59]. One of the main reasons is safety, in fact, in sectors such as aerospace, transport and oil and gas, corrosion can compromise the structural integrity of equipment, vehicles and infrastructure. Early detection of corrosion can help prevent accidents, equipment failures and potential disasters. Other significant factors include cost savings, environmental conservation, longevity of infrastructure and products, etc.

In order to realize low-cost and low-power sensors suitable for continuous or periodic remote monitoring, EC methods show to be suitable with the required characteristics as the measurement systems need low-cost sensors with low-power consumption and they can perform non-contact measurements with an easy readiness to realize sensor arrays that can cover larger areas.

In this research activity, the focus was on the hardware section of the measurement system usually adopted in EC methods while the measurement method was based on the swept-frequency approach as described in the previous research activities. In particular, the aim was to develop a low-cost optimized sensor that can estimate the early stages of superficial and hidden corrosion with good accuracy and low-power consumption. To this purpose, an innovative eddy current pot-cored sensor was proposed.

The pot-cored consists of a magnetic shielding ferrite core that has a closed magnetic path. It is used to concentrate the magnetic flux on the surface of the sample under test by decreasing the magnetic flux leakage into the air. In addition,

it reduces the edge effects that usually affect the results in EC methods [60–63].

In particular, the major contributions of this activity were related to:

- a numerical and experimental analysis in which a comparison was carried out between a common air-cored sensor and the proposed pot-cored sensor;
- a complete characterization of the proposed pot-cored sensor under different analysis conditions including superficial corrosion, hidden corrosion and corrosion under insulating layers;
- an experimental set–up for the estimation of the corrosion state, based on single-frequency or multi-frequency measurements.

Compared with the scientific works already established in the literature, the sensor proposed in this research activity offers two main advantages. The first one is related to the excitation current required to achieve good measurement capability. In fact, it is much lower with respect to commonly used air-cored sensors. This aspect gives the possibility of using a single-frequency excitation approach allowing the sensor to be easily integrated into remote monitoring systems. The second one is the integration of a Tunnel Magneto Resistance (TMR) sensor allows the measurement system to carry out analysis of very low excitation frequencies, thus enabling analysis with a greater depth of penetration.

The thesis is structured as follow: Chapter 2 describes the state of the art related to the NDT methods, concepts relating to NDT&E 4.0 and the basics of quality control are described. The optimization methods for thickness estimation are extensively described in Chapter 3, while Chapter 4 shows the dimensional analysis in case studies of interest. In Chapter 5, the sensor and measurement method development related to the detection and characterization of corrosion states is described. Finally, in Chapter 6 there are the conclusions of the research project.

Chapter 2

State of the Art

2.1 Quality control concept

In today's industrial scenario, the concept of quality control has taken on a whole new dimension with the advent of Industry 4.0. This transformation era, characterized by the integration of cutting-edge technologies, data-driven decision-making, and interconnected processes, has ushered in a revolution in the manufacturing sector. Quality control, long considered a cornerstone of production, has been redefined and elevated to unprecedented levels of precision, efficiency, and effectiveness. As industries worldwide embrace the potential of Industry 4.0, the way products are inspected, validated, and optimized is undergoing a depth transformation.

Quality control has always been an essential aspect of manufacturing. It involves a series of systematic processes and measures implemented to ensure that products meet or exceed specified standards and customer expectations. Historically, quality control was primarily reliant on manual inspections, sampling techniques, and statistical analysis. While these traditional methods have been successful in maintaining product quality, they often suffered from limitations such as time-consuming inspections, human errors, and the inability to detect subtle defects in complex products.

The advent of Industry 4.0, driven by technologies like the Internet of Things (IoT), artificial intelligence (AI), machine learning, and big data analytics, has revolutionized the landscape of quality control. These technologies have enabled the creation of smart factories where machines, equipment, and systems communicate with each other in real-time. Sensors and connected devices collect vast amounts of data throughout the production process, providing manufacturers with unprecedented insights into their operations.

One of the most significant transformations brought about by Industry 4.0 is predictive quality control. Instead of relying solely on post-production inspections, manufacturers can now anticipate and prevent defects before they occur [1, 2]. Machine learning algorithms analyze real-time data to identify deviations from the norm, enabling proactive adjustments to manufacturing processes. This not only reduces the likelihood of defective products reaching customers but also optimizes resource utilization and minimizes waste [3, 4].

Furthermore, the concept of "zero-defect manufacturing "has become a tangible goal in the Industry 4.0 era. Through continuous monitoring and real-time feedback loops, manufacturers can maintain consistent product quality throughout the production cycle. Automated quality control systems can perform complex inspections with unmatched precision, detecting defects at microscopic levels that were previously impossible to identify. This level of accuracy enhances product reliability and safety, essential in industries like aerospace, automotive, and healthcare.

Industry 4.0 has also elevated quality control to the role of customer focus. With increased connectivity, manufacturers can gather valuable feedback from end users, incorporating their preferences and suggestions into product design and production processes. This level of customer engagement not only fosters brand loyalty, but also allows for agile adaptation to changing market demands.

In conclusion, the integration of Industry 4.0 technologies into quality control processes represents a paradigm shift in manufacturing. The era of smart factories, predictive quality control, and customer-centric production has dawned, offering manufacturers unprecedented opportunities to enhance product quality, reduce costs, and stay competitive in an increasingly dynamic global marketplace. This transformation underscores the importance of embracing and harnessing the power of Industry 4.0 to redefine the way we approach and achieve quality control in modern industry. As we enter this revolution, we must explore the nuances, challenges and limitless possibilities that await us on the road to manufacturing excellence.

2.2 Typology of defects

Defects occurring within materials are numerous and may depend on the most different causes; they may pre-exist within the material, be a consequence of the processing to which they are subjected, or they may depend on the operation to which they are disposed. The wide variety of defects highlights the difficulties encountered by operators in the field and underlines the constant development of multiple investigation techniques, each with its own specific characteristics and therefore with the natural predisposition to be applied to the particular case. De-

fects can creep into the production process, giving rise to two distinct types of defects: manufacturing defects and operating defects. Understanding the shades of these defects is crucial to maintaining product quality, ensuring safety and maintaining consumer confidence.

Production defects are essentially the unwanted intruders that enter the product creation process, often unbeknownst to those responsible for its creation. These defects occur during the various stages of production, from initial design and material selection to manufacturing, assembly and quality control. They can result from a multitude of factors, including human error, equipment malfunction or material deficiencies [64]. A common source of production defects is the lack of adherence to established quality control measures. When these guidelines are not strictly followed, even the most well-conceived designs can be marred by defects. For example, a small oversight in the calibration of a cutting machine can cause uneven edges on a metal component, rendering it unfit for its intended purpose.

In addition, material defects can also play a significant role in manufacturing defects. Materials that do not conform to required standards can cause structural weaknesses, corrosion or other vulnerabilities in the final product. This is of particular concern in sectors where safety is paramount, such as aerospace or automotive.

On the other hand, operating defects are latent issues that become apparent only when a product is in use. Unlike manufacturing defects, which are inherent to the product's creation, operating defects may remain dormant for an extended period, escaping detection during quality control checks. These defects can be caused by various factors, including wear and tear, design limitations, or environmental conditions [65]. Operating defects can also emerge due to unexpected interactions between components. In complex systems such as computers or industrial machinery, the interaction between numerous parts can lead to unforeseen defects that were not apparent during the production phase of the product. Identifying and correcting these defects often requires extensive diagnostic procedures and specialised expertise.

In conclusion, different defect types can be detected and characterized in industrial scenario. In order to detect defects in an invasive, non-destructive manner, thus reducing costs and the amount of discarded material, the tests usually applied involve the world of Non-Destructive methods. The next subsection will give a brief overview of the most commonly used methods in industry environment.

2.3 Main methods in NDT&E framework

The considerable variety of defects coupled with the different nature of the materials used to produce the final products, which have the most varied shapes, has led to the development of a considerable number of NDT&E investigation methods. Therefore, making a detailed distinction on the applicability of each NDT, depending on the field of use, is a very onerous and arduous task to undertake. In fact, it is often preferred to classify NDT&E investigation techniques according to the performance they can guarantee. In this respect, a broad classification can be made into:

- techniques for superficial investigations: suitable for examining materials only at a superficial level (for example [13, 14, 19, 20];
- techniques for volumetric investigations: suitable for detecting discontinuities within materials (for example [29–31];
- techniques for global investigations: suitable for verifying the state of a component as a whole (for example [66, 67]).

Another conditioning factor is related to the kind of material tested, as not all methods are suitable for investigating the wide range of materials used in all fields requiring NDT&E investigation. The following is an overview of the most commonly used techniques in the various industrial sectors.

2.3.1 Thermographic methods

Thermography is a sophisticated and versatile inspection method that utilises the principles of heat transfer to detect and assess defects and anomalies in a wide range of materials and structures. This non-invasive technique has been widely accepted in various industries, including aerospace, manufacturing, construction and preventive maintenance, due to its ability to provide valuable information on the integrity and performance of components and systems.

At its core, thermographic NDT relies on the fact that materials respond differently to heat, and variations in temperature can be indicative of underlying defects. The key principles involved in this method include:

- Heat generation: an external heat source, such as a heat lamp, infrared heater, or even natural sunlight, is used to heat the surface of the material or structure under inspection;

Figure 2.1: General representation of the results obtain trough the thermographic instrumentation.

- Thermal conductivity: different materials conduct heat at different rates. Internal flaws, such as cracks, delaminations, or voids, often have different thermal conductivities than the surrounding material. This leads to variations in heat flow at defect locations;
- Infrared detection: an infrared camera or thermal imaging device is employed to capture the temperature distribution on the surface of the material. These devices can detect even minor temperature differences with high precision.
- Data analysis: the thermal images are analyzed using specialized software. Variations in temperature are processed and visualized as thermal patterns or anomalies, which can indicate the presence and location of defects.

All the procedures and instrumentation that can be used for certified thermografic NDT&E are represented in the standards UNI ISO 18434-1:2011 and UNI EN 16714-2:2016 [68, 69].

This method has certain advantages. For example, it is a non-contact method, i.e. it does not damage the material or structure being inspected during testing. Furthermore, the method provides rapid results that make it suitable for both production environments and field inspections. The method's wide applicability has recently been demonstrated; it is adopted in all sectors, from automotive to civil.

2.3.2 Visual inspections

Probably the most important method of non-destructive investigation of any object is visual examination. In fact, in a broad sense, all results of any method of investigation must be visualized by the operator for recording and interpretation.

However, visual examination only means the inspection of objects with the naked eye or with the aid of low-magnification lenses or endoscopes.

The principle is based on the use of light as a means of detecting defects. By analyzing the direction, amplitude and phase of light reflected or scattered from the surface of an opaque object, or transmitted within a transparent medium, information on the physical state of the object under examination can be obtained. Although it is the most natural method, it requires a fair amount of observational aptitude and considerable experience to reveal all potentially useful information to the operator. Examination with the naked eye alone is also much more complex than one would think and requires a good knowledge of optics and illumination.

Figure 2.2: Non-destructive inspection using the visual inspection technique.

Visual inspections, as also suggested by the reference standard UNI EN 13018 [70], are generally divided into:

- direct visual examinations: used when there is the possibility of visual access (with the naked eyes) at a distance of no more than approximately 60 cm from the surface under examination and at an angle of no less than 30°;
- remote visual examinations: used when there is no possibility of direct access to the surface under examination. More or less sophisticated equipment is used for this purpose, such as mirrors, telescopes, endoscopes, fibre optics, video cameras, etc. In any case, whatever the means used, the instruments must have a resolution at least equivalent to that of the human eye.

This method is advantageous, as it allows for the identification of a significant number of defects such as cracks, corrosion, colour changes due to overheating,

erosion, deformation, irregularities in surface finish, assembly errors of mechanical systems, dimensional variations, etc. On the other hand, one of the main limitations is that only surface defects can be detected, and the technical competence and experience of the inspection personnel are essential to ensure the sensitivity and reliability of the result.

2.3.3 Liquid penetrant methods

Liquid penetrant (LP) methods are between the simplest and least expensive NDT for detecting discontinuities and cracks of various types. It proves to be a very practical method, as it can be applied to any type of non-porous material. It consists of spreading a special liquid on the surface under examination, usually oily and of variable and/or fluorescent colour, with low surface tension, good "wettability " and special physical properties that allow it to penetrate discontinuities by capillarity. After removing the excess liquid from the piece under examination, by washing it with cold running water, a special absorbent material, known as a detector, is applied to the entire surface to be examined. An absorbent material, called a detector, which carries the liquid introduced into the discontinuity in such a way as to leave a more visible mark than the defect that generated it and thus provide an indication of the same.

Compared to visual inspection, this method makes it easier for the operator to assess defects, essentially because the indications provided are significantly larger than the size of the defect. significantly larger than the size of the defect, which makes it possible to detect even cracks that are below the resolution threshold. The normative reference for the liquid penetrant technique is UNI ISO 3452-1:2021 [71]; it defines the test execution steps in detail (see Fig.2.3):

- Surface preparation: the first step is to thoroughly clean the surface of the material being tested. Any contaminants, such as dirt, grease, oil, or paint, must be removed to ensure the penetrant can properly access the defects;
- Application of penetrant: a colored or fluorescent liquid penetrant, often called the "penetrant," is applied to the surface of the material. This penetrant is highly visible and can seep into any open or surface-breaking defects;
- Dwell time: the penetrant is allowed to dwell on the surface for a specified period, typically 10 to 30 minutes. During this time, the penetrant is drawn into any cracks, voids, or other imperfections via capillary action;
- Excess penetrant removal: after the dwell time, excess penetrant is carefully removed from the surface. This is usually done by wiping or rinsing with a solvent. The penetrant that has entered defects remains in place;

- Developer application: a white, absorbent developer is then applied to the surface. The developer draws the trapped penetrant out of any defects, causing it to bleed onto the surface. This makes the defects visible and forms a contrasting background against the penetrant;
- Inspection: the surface is inspected visually under appropriate lighting conditions. Defects are identified as colored indications against the white developer background or as fluorescent indications under ultraviolet (UV) light when a fluorescent penetrant is used;
- Evaluation: the size, shape, and location of the indications are carefully examined and evaluated to determine their significance. Not all indications found may be defects; some may be harmless surface anomalies;
- Documentation: the findings are documented, and a report is generated, detailing the location and characteristics of any defects found during the inspection.

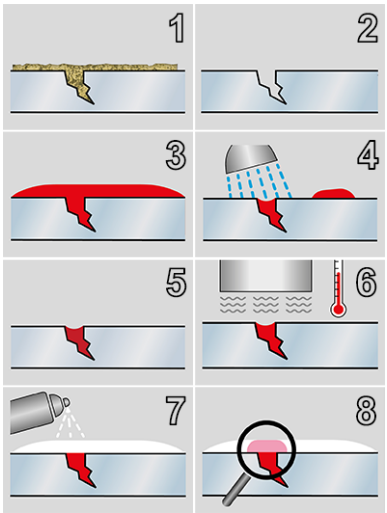

Figure 2.3: Procedure related to liquid penetrant method.

Surface preparation is one of the most critical steps, as any traces of water, oil, grease or other substances that may impede or limit the access of the penetrating liquid inside the defects must be completely removed. The Standard imposes certain precautions to be taken in the different stages of inspection, for example for example, the penetration time must be between 5 and 60 minutes, depending

on the specific depending on the specific characteristics of the product used and is variable depending on function of the type of application being carried out.

This technique is very sensitive to small surface discontinuities, has a low application cost, easy execution and interpretation of the result. On the other hand, only surface defects can be detected, it requires careful preparation of the surface to be tested, the time required is high, and the quality of the test depends on the experience of the operator.

2.3.4 Eddy Current methods

The eddy current method (ECT) is one of the main NDT methods and is used on an industrial level for the inspection of metallic materials both in the semi-product state (bars, tubes, etc.) and of finished parts from mechanical processing. Various types of examinations can be carried out using eddy currents:

- detecting of surface and subsurface defects;
- sorting of materials for differences in composition or structure;
- measuring the thickness of a product or a protective coatings;
- measuring the electrical and magnetic properties of the product.

Depending on the specific type of examination and use (on manufactured or semi-manufactured products), the equipment used has a greater or lesser instrumentation complexity.

The operating principle of the method basically consists of inducing an alternating magnetic field, created by means of special coils, in the part under examination. In accordance with Lenz's law, the material becomes the site of an induced electromagnetic field which, acting in a medium with electrical conductivity $\sigma > 0$, causes an electric current to circulate on the sample itself (eddy current).

The flow direction of this current will in turn produce a magnetic field opposite to that of the external magnetising field (see Fig. 2.4).

The magnetic field associated with the object under test varies in relation to the geometrical, electrical and magnetic characteristics of the object itself and is analyzed by evaluating its effects on the current or voltage of the inducing coil or on the current or voltage induced in another coil also located close to the surface of the object under test (in this case, the second coil is referred to as the 'pick-up coil').

Eddy Current method is frequently utilized as a surface inspection method but can also be used to analyze the thickness of a sample or the presence of internal defects in its structure. This can be defined due to the skin effect: in a flat

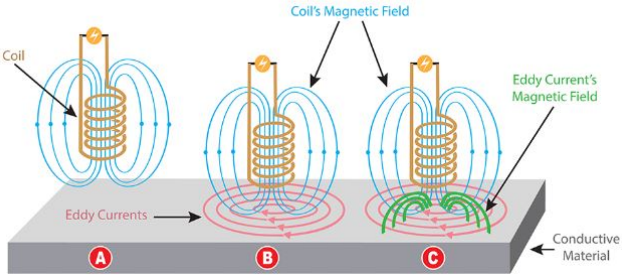

Figure 2.4: Eddy current physical principle. It represents: (a) the magnetic flux when the probe is too far from the conductive sample; (b) the generation of the eddy currents on the surface of the conductive plate; (c) the generation of the reaction magnetic flux from the eddy currents.

conductor, the current intensity decreases exponentially with penetration and, in general, the lower the excitation frequency (f), magnetic permeability (μ) and electrical conductivity (σ), the greater the penetration depth (δ) (see Fig.2.5). If we consider a one-dimensional geometry where the half-space $x > 0$ is occupied by homogeneous conducting material, the modulus of induced currents follows the law reported in Eq. 2.1.

$$J(x) = J_0 \cdot e^{-\frac{\delta}{x}} \tag{2.1}$$

Where:

- $\delta = \frac{1}{\sqrt{\pi \cdot f \cdot \sigma \cdot \mu}}$ is the skin depth (or penetration depth);
- $J(x)$ is the module of the current density vector as a function of depth x;
- J_0 is the module of the current density on the conductor surface (e.g. x=0).

The current module is approximately 37% of the current module related to the surface when the depth $x = \delta$. The δ value presents an important decrease when the excitation frequency increase. As the frequency of the reaction field increases and all other conditions being equal, the amplitude of the currents increases. In this case, it is important to note how the SNR can be improved for higher frequencies and it could be an important issue in case of low frequencies. Therefore, depending on the type of examination to be performed, higher or lower frequencies will be chosen.

It is also important to emphasise the dependence of the penetration depth on the electrical (σ) and magnetic parameters (μ) that describe the material under

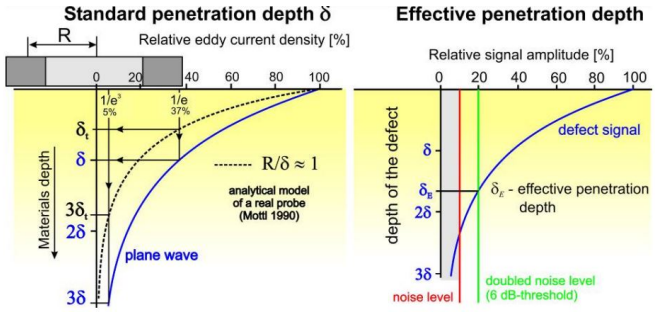

Figure 2.5: Depth penetration principle [72].

test. Depending on the value of these parameters, it will be necessary to design the necessary excitation frequencies for the analysis to be performed.

This concept will be analyzed extensively in the following Chapters as penetration depth (δ) will play a key role in estimating thickness (Chapter 3 and Chapter 4) and hidden corrosion (Chapter 5).

2.3.5 Tomographic methods

Tomography has become a useful instrumentation technology that can provide a cross-sectional image of a measuring object or process. Unlike conventional sensing techniques, which can only provide a measurement value of a single point, tomographic sensing techniques can provide additional information representing the true condition of the measured object [73].

The conventional application of tomography is the field of medical diagnosis, which involves scanning the static human body [66, 67].

Different tomography techniques use different forms of penetrating waves to detect changes in the properties of an object. For example, X-ray tomography uses high-frequency energetic electromagnetic radiation to detect material density; magnetic resonance tomography uses a strong magnetic field and radio waves to detect hydrogen atoms in the body.

Tomography techniques use different physical phenomena and, consequently, their target applications will also be different. A typical tomography system often consists of several transmitters and receivers, with the aim of collecting as much projection data as possible. The data measured from different projection angles are then fed into a reconstruction algorithm to convert the measurements into a "tomogram ", the cross-sectional image of the object.

Computed tomography (CT) scanning, often referred to simply as CT or CAT

(Computerized Axial Tomography) scanning, is a powerful imaging technique used in both medical diagnostics and industrial NDT (see Fig. 2.6). CT scanning allows for the creation of detailed cross-sectional images or "slices"of an object or a patient's body without the need for invasive procedures or disassembly.

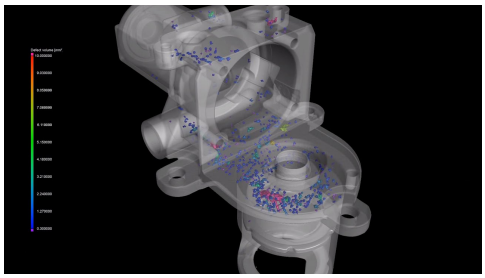

Figure 2.6: Representation of the scanning results using computed tomography.

One of the main problems with CT scanning is exposure to ionising radiation. X-rays are used to create the images and repeated or excessive CT scans can lead to cumulative radiation doses that can increase the risk of cancer. In addition, CT scanners are complex and expensive machines, and the cost of both acquiring and maintaining them can be substantial.

In the recent years, other typologies of tomography are developing. In particular, Electrical tomography is a relatively new form of tomography that can be applied in many industrial applications. This method uses low-frequency electromagnetic waves (kHz–MHz) to sense the passive electrical properties of an object, such as conductivity, permittivity and permeability. Its electrically sensitive property allows it to be applied in many applications. Since the method was proposed, its low cost, non-intrusive and non-invasive features have made the technique extremely attractive compared with conventional X-ray/γ-ray tomography systems.

Its biggest advantage is its ability to be applied to large-scale processes, which cannot be achieved using other hard-field techniques such as magnetic resonance imaging and ultrafast X-ray. However, the biggest drawback of the electrical tomography technique is its low spatial resolution because of its severely ill-posed nature. Owing to this drawback, electrical tomography techniques are often more applicable to industrial applications, as high spatial resolution is more vital for medical diagnosis applications.

In relation of the quantity of interest, different electrical tomography are available; in the recent years were proposed electrical impedance tomography [74–76], electrical resistive tomography [77–79] and electrical capacitance tomography [80, 81].

2.3.6 Ultrasonic methods

Ultrasonic methods are highly effective and widely utilized techniques in various industries for inspecting materials and structures without causing any damage. These methods employ high-frequency acoustic waves to detect and characterize internal flaws, defects, and anomalies, making it invaluable for ensuring the integrity, safety, and quality of critical components (see Fig. 2.7).

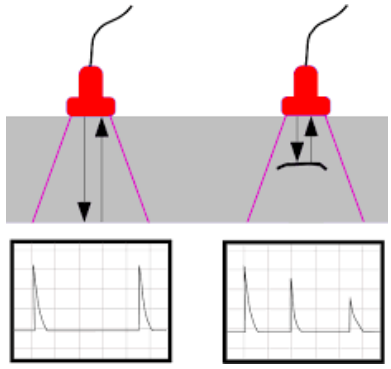

Figure 2.7: Schematic representation of ultrasonic principle.

Ultrasonic NDT offers several key advantages, including exceptional sensitivity to both surface and subsurface defects, the ability to penetrate deep into materials, precise sizing and positioning of flaws, real-time inspection capabilities, and non-destructive nature. These qualities make it suitable for a wide range of applications, from weld inspections in critical industries like aerospace and oil and gas to assessing the quality of manufacturing components and ensuring the safety of infrastructure in construction [29–31].

The core principles of ultrasonic methods involve the generation of acoustic waves using specialized transducers, their propagation through the material being examined, and the analysis of the waves upon their return. By evaluating factors such as wave reflections, refractions, and time delays, ultrasonic testing systems can produce visual representations of the material's internal structure [82].

The ultrasonic wave consists essentially of vibrational energy that is introduced into a certain number of particles in the medium; these in turn transmit it to adjacent particles and so on, giving rise to the propagation of the ultrasonic wave. There are thus two parameters: the direction of propagation and the direction of vibration, which, being independent of each other, give rise to different types of waves, the most common of which, used for the detection of discontinuities, are shown below:

- Longitudinal waves: in longitudinal or compression waves, the direction of vibration of the particles is parallel to the direction of propagation. Imagine that the particles of the medium on which the elastic wave arrives are arranged in planes perpendicular to the direction of propagation and regularly spaced apart from each other; the longitudinal wave causes all the particles in this plane to vibrate with forward and backward displacements with respect to their rest position; in this way they cyclically decrease and increase their distance from the next plane, communicating to the particles lying on the latter the motion and creating at the same time zones of pressure and depression. Longitudinal waves are the most commonly used and propagate in solid, liquid and aeriform material (see Fig. 2.8 (a));
- Transversal waves: in transverse or shear waves, the direction of vibration of the particles is perpendicular to the direction of propagation, i.e. each plane of particles oscillates parallel to itself, being subjected to a shear stress. In this case, it is not possible to associate a pressure with the wave as in the previous case; in fact, the stress is represented by a shear stress. Since gases and liquids do not withstand shear stress, transverse waves propagate only in solids (see Fig. 2.8 (b));
- Rayleigh waves: surface waves, or Rayleigh waves, propagate only in the surface layers of solids and the vibration of individual particles occurs in practically elliptical orbits; one particle transmits motion to the next, thus generating wave motion. Surface waves follow the shape of the material's surface, being reflected by surface edges and discontinuities. In addition, they are particularly sensitive to impurities, oil droplets, etc., along the way, which is why they are rarely used in the surface of solids (see Fig. 2.8 (c)).
- Lamb waves: lamb waves, or bending waves, are generated when an elastic wave propagates in a layer of solid material having a thickness of the order of the wavelength. They are divided into two classes depending on the mode of vibration: symmetrical mode waves, or antisymmetrical mode waves. Furthermore, for each of the two modes there are waves of order 0, 1, 2 etc (see Fig. 2.8 (d) and (e) respectively).

In conclusion, these types of waves and the different transmitting techniques enable this method to estimate internal and sub-surface defects. In the most usual application, an ultrasonic pulse is emitted which, as it propagates through the material to be examined, is partly reflected by any discontinuities present, partly absorbed by the material and partly passes through it completely. By analyzing these contributions, it is therefore possible to highlight the presence of a possible defect. This operation involves two possible methods of implementation:

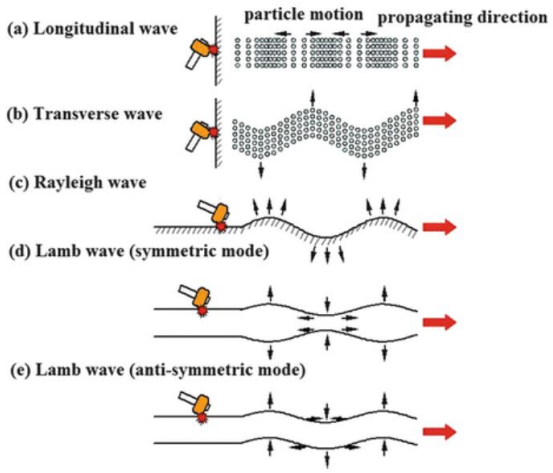

Figure 2.8: Graphical representation of ultrasonic wave propagation (a) longitudinal, (b) transverse, (c) superficial, Lamb's (d) symmetrical and (e) antisymmetrical.

- Reflection method: a single transducer is used to both emit sound waves and receive the reflected acoustic energy;
- Transmission method: the reception of acoustic energy is carried out by a transducer other than the transmission transducer.

The application of one or the other method is subject to considerations regarding the shape and geometry of the parts, the type and orientation of the defects to be detected, operational simplicity and the required inspection speed. UT methods are widely applied as they are very sensitive to most of the discontinuities present in different types of materials and allow inspection of thick samples ($\geq$ 20mm) (see [7, 29–31]).

However, there are still numerous disadvantages associated with this investigative method, such as:

- the need to use probe couplants (water or gels);
- the loss of sensitivity to thin defects parallel to the direction of propagation of the ultrasonic beam;
- instrument calibration procedures to obtain an easily recognisable defect response;
- challanging identification of specific defect type;

- highly qualified operators capable of interpreting the test result, providing a measurement indication based on their experience.

2.4 Introduction of NDE 4.0 concept

Non-Destructive Evaluation (NDE) has been an essential part of industries like manufacturing, aerospace, and construction for decades. It involves inspecting materials, components, and structures without causing any damage to them. As we move further into the Fourth Industrial Revolution, NDE is undergoing a significant transformation, commonly referred to as NDE 4.0. This concept integrates advanced technologies and data-driven approaches to enhance the efficiency, accuracy, and overall impact of NDE [23–25].

NDE 4.0 represents a shift towards the smart, connected, and data-centric practices that define Industry 4.0. Here are the key components of this concept:

- Robotics and automation: robots and autonomous systems are increasingly utilized for NDE tasks, especially in hazardous or hard-to-reach environments. These machines can perform inspections with precision and consistency, reducing human error and improving safety;
- Remote inspection: NDE 4.0 enables remote inspections, allowing experts to assess assets from anywhere in the world. Sensors with low-power consumption useful for remote and stand-alone applications. This is particularly valuable for global organizations with distributed operations;
- Sensors and IoT Integration: in NDE 4.0, sensors are deployed extensively to collect real-time data from various equipment and components. IoT devices are used to connect these sensors to centralized systems, enabling continuous monitoring and analysis of assets. This ensures that anomalies are detected early, reducing the risk of unexpected failures;
- Advanced imaging techniques: traditional NDE methods such as radiography, ultrasonic testing, and magnetic particle testing are being enhanced with cutting-edge imaging technologies. For example, digital radiography and computed tomography (CT) scanning provide high-resolution images for improved defect detection and characterization;
- Machine learning and artificial intelligence: machine learning and AI algorithms are applied to the vast amounts of data collected during NDE processes. These algorithms can identify patterns, recognize defects, and predict potential failures with remarkable accuracy. This proactive approach helps in predictive maintenance and reduces downtime;

- Environmental sustainability: NDE 4.0 also places a strong emphasis on sustainability by reducing waste and energy consumption. By optimizing inspection processes, industries can minimize the environmental impact of NDE activities;
- Data analytics and Big Data: NDE 4.0 relies heavily on data analytics to derive meaningful insights from the data generated. Big data platforms are employed to store, process, and analyze large volumes of NDE data, enabling informed decision-making and optimization of inspection processes.

In conclusion, NDE 4.0 represents a paradigm shift in NDT&E framework, taking advantage of the latest technology to make inspections more efficient, precise and proactive. It enhances asset reliability, safety, and overall operational excellence. As industries continue to adopt NDE 4.0 practices, they can expect reduced downtime, increased asset lifespan, and improved quality control, ultimately contributing to their competitive advantage in an ever-evolving industrial landscape.

2.5 Comments and rationale of the reaseach project

In this Chapter, different typologies of defects were described and analyzed. Among the many factors that contribute to the quality of a product, in this research activity our focus was on thickness measurement.

The ability to accurately measure and control the thickness of materials is not only a fundamental aspect of quality control, but also a key to ensuring the reliability, performance and safety of countless products we encounter in our daily lives. The importance of accurate thickness measurement cannot be overstated, as it impacts a wide spectrum of industries ranging from aerospace, automotive, construction to electronics, packaging, oil & gas and pharmaceuticals.

Thickness defects, whether excessive or inadequate, can have dangerous consequences. For example, in the aerospace industry, where every component must meet stringent safety standards, the incorrect thickness of a critical part can lead to failure. The pharmaceutical industry, on the other hand, depends on precise thickness measurements to ensure the effectiveness and safety of drug delivery systems. Furthermore, thickness measurement plays an essential role in optimising production processes. By monitoring the thickness of materials at various stages of production, companies can identify trends and make real-time changes to maintain consistency and reduce waste. In the automotive industry, for example, accurate thickness measurement of coatings ensures that vehicles have a uniform finish.

In addition, another type of defect analyzed in this research activity is corrosion on metallic materials. The importance of early corrosion detection cannot

be overstated, as it not only safeguards valuable assets but also preserves the integrity and longevity of critical infrastructure, from towering bridges to essential pipelines. Corrosion, the gradual degradation of metals through chemical or electrochemical reactions with the surrounding environment, is an insidious problem. It erodes structures from the inside, weakening their structural integrity, compromising safety and leading to high maintenance and replacement costs. If left unchecked, corrosion can lead to dangerous failures, with possible consequences for public safety and the economy.

As already discussed within this Chapter, the NDT&E methods have a key role in the quality control. Among the advantages of NDT&E methods is its ability to detect and characterise defects, imperfections or corrosion non-invasively and without destroying the sample under examination. By identifying these imperfections early in the production process, NDT&E methods allow industries to correct problems earlier, improving product safety and longevity.

In addition, in recent years, the concept of NDE 4.0 has emerged. The main objective of NDE 4.0 is to identify defects and anomalies without damaging or compromising the integrity of the material or product being tested as the classic NDT&E methods. The novelty lies in the fact that it is based on the use of advanced tools, smart and low-cost sensors and advanced data analysis to carry out increasingly precise, timely and efficient inspections.

Of the different NDT&E methods shown, the Eddy Current method is among the most promising. In addition to having low operating costs, it can only be used with conductive materials, but this is not a major limitation, as most products with high mechanical and corrosion resistance requirements are made of metal. Therefore, all objects made of iron or steel, aluminium or aluminium alloy, even non-metallic but conductive materials such as graphite or composite materials can be tested. It is possible to introduce these sensors into automated processes because it is possible to measure products without physical contact between the probe and the surface under examination; this makes it possible to inspect moving products and components characterised by special geometries or high surface temperatures. In addition to a wide variety of applications, it offers numerous other advantages: high examination sensitivity (understood as the ability to detect small defects and measure geometric characteristics of products with great precision), great reliability and speed of execution. In order to solve the problems associated with other measurement methods (measurement time and costs, need for measurements in contact with the sample under test, etc.), the potentials of measurement methods using Eddy Current were analyzed and developed.

In the following Chapters, the methods, experimental set–ups and sensors developed in the application field of thickness measurements and the detection and

characterization of corrosion states will be shown.

Chapter 3

Eddy Current methods for thickness estimation of metallic plates: proposed optimizations

Thickness measurements play a very important role in many industrial applications related to metallic plates. Indeed, they provide information about the quality of the production, the capability of crash energy absorption, the safety of parts. These aspects are crucial in application fields such as automotive and aerospace, where the integrity of the metal plates has a direct impact on the safety of human beings. In the actual industrial practice, some metrological checks are carried out by using touch-trigger probes [26]. Unfortunately, such measurements are time-consuming and not suitable for integration within the production processes. Other options are laser and ultrasound methods. Concerning laser-based measurement methods, we highlight that they allow in-situ measurements with very good measurement accuracies, but the higher cost of the equipment has a major impact on the overall product cost [27, 28]. Concerning ultrasound methods, they represent a possible alternative to optical methods, as far as the measurement accuracy are concerned, but they usually require the coupling gel that imposes an expensive procedure for cleaning the sample, the use of expensive measurement systems [7, 29–31] and the presence of qualified technicians to perform the test. All these aspects make this kind of test not suitable for inline thickness monitoring during the manufacturing stage.

Thickness measurement methods based on Eddy Current Testing (ECT) can

be usefully used in all those applications in which it is important to measure the thickness of metal plates (e.g., automotive, aerospace, etc.). These methods can be an excellent solution to this purpose thanks to: *(i)* the high accuracies, *(ii)* the high repeatability and sensitivity, *(iii)* the possibility to automatize the test, *(iv)* the immunity to non-conductive materials present on the sample (e.g., dust, painting, insulating cover), *(v)* the possibility to carry out measurements without physical contact with the sample, and *(vi)* the cheapness of the probe as already discussed in subsection 2.3.4.

The thickness measurement methods by using ECT can be divided into two main classes: the multi-frequency (MF) methods [7–9, 32–34] and the Pulsed Eddy Current Testing (PECT) methods [35–37].

PECT methods achieve their best performances when the thickness to be measured is estimated via a proper feature from time domain data. As a matter of fact, PECT signals can be used to get swept-frequency data but may result to be not optimal. Indeed, the harmonic content of the applied signal decay fast with the order of the harmonic itself. For instances, in the case of the widely used rectangular pulse, the energy of the harmonics decays as $1/n^2$, with impact on the signal-to-noise ratio. Another potential issue is that the tones of PECT signals are allocated at frequencies which are multiple of the inverse of the fundamental period of the (periodic) waveform. This specific distribution of the tones may be not optimal for a specific application as the present one. With SF methods, a suitable set of discrete frequencies of interest is chosen to allocate the signal energy in a controlled manner. Compared to PECT, measurement times may be longer, but the MF technique promises the possibility of optimisation of the excitation signal.

Using the MF technique, in [32–34] Yin *et al.* proposed and optimized measurement probes and processing algorithms developed ad-hoc for the measurement of the thickness of non-magnetic materials by means of Eddy Current Testing. Specifically, their method gives an accuracy compatible with industrial production standards and proper immunity to lift-off variations. In detail, thanks to the Dodd and Deeds model [83], they were able to relate the thickness of a planar and infinite plate to the frequency where the minimum of a proper quantity is achieved. They proved experimentally the effectiveness of the method [32–34], showing that it exhibits very good accuracies in-line with those required for industrial manufacturing standards [84].

Unfortunately, as introduced in Chapter 1, this method has two main limits related to the measurement accuracy for the range of thicknesses analyzed and the measurement times.

About the first limit, the method proposed in [32] relies on the constancy of a certain parameter (α_0). Unfortunately, this parameter is highly dependent on the

thickness of the sample, and it can be maintained constantly only asymptotically for thicknesses much smaller than the size of the probe. This makes the method impractical for thick samples or in the presence of curved surfaces. For instance, in the latter case, there are two conflicting constraints: *(i)* the probe has to be much larger than the thickness of the sample and *(ii)* the probe has to be much smaller than the curvature of the sample, so as to approximate the surface of the sample by means of its tangent plane, in a neighborhood of the probe itself.

The aim of the research activity was to provide a deep, complete and more general theoretical framework for the method proposed in [32], allowing it to be extended to a broader class of thickness measurements [38, 39]. From the technical perspective, it was proposed that the critical constant parameter α_0 has to be replaced by a new function $\alpha = \alpha(\Delta)$ which depends on the thickness Δ. Through this modification, it was extended the method's range of applicability, while identifying its underlying physical limits.

In addition to the study of theoretical fundamentals, two different algorithms for performing thickness measurements were proposed. The first algorithm is iterative and is conceived for applications where the unknown thickness ranges from 0 up to the theoretical limit of the method. This approach requires the knowledge of the function $\alpha(\cdot)$, for a given probe. The second algorithm is based on a polynomial approximation of $\alpha(\cdot)$ and provides the thickness as the solution of an algebraic equation of the same degree as the approximating polynomial. Computationally, this is extremely efficient when the polynomial approximation is up to the third order, since the related algebraic equation can be quickly solved in closed form. A higher computational cost is required when increasing the degree of the polynomial approximation. The resulting measurement method is very efficient in terms of measurement and computational times, and suitable for low-cost measurement architectures, thus ensuring the possibility to get online and real-time measurement instruments for industrial needs.

Related to the second limit, the method proposed in [32] identifies the thickness of the sample by considering the real part of the variation of either the self-impedance or the mutual impedance due to the presence of the sample divided by the angular frequency ($\Delta R/\omega$). The thickness is associated with the angular frequency at which the quantity reaches $\Delta R/\omega$ its minimum value. To warrant the desired measurement accuracies, the method proposed in [32], requires measurements with very narrow frequency resolutions. This is a major issue when the nominal width of the sample under test is unknown, because the method requires the analysis of a large frequency range (few hertz to some kilohertz) with a very narrow frequency resolution. These two aspects lead to an increase of the measurement time that might reach tens of seconds or more, making it not suitable for

in-line and real-time industrial applications.

With the aim of minimizing the measurement time but keeping the required measurement accuracy, several optimizations of the measurement method were proposed. In detail, the optimizations were carried out along two main routes: *(a)* the use of smart excitation strategies able to minimize the measurement time, and *(aa)* the use of improved processing algorithms able to warrant the desired accuracy even in presence of a minimal set of measured signals. In detail, regarding *(a)*, a dual-stage measurement procedure based on optimized multi-frequency signals has been implemented to reduce the measurement time [85, 86]. Concerning *(aa)*, proper interpolations have been implemented to achieve the required measurement accuracies. A huge experimental campaign confirmed that the proposed optimized measurement method minimizes the overall measurement time while keeping the required measurement accuracy [40].

In order to show in depth the solutions made to the described limits, the following Sections are devoted to describing the theoretical framework and proposed solutions.

In particular, Section 3.1 will describe the theoretical framework underlying the method proposed in [32]. In Section 3.2, the limits related to the non-constancy of the α_0 parameter when varying the analyzed thickness and the consequent decrease in measurement accuracy are shown. Section 3.3 shows the limits related to the measurement times required for the method proposed in [32] to achieve good measurement accuracy. The algorithms used for improving the measurement accuracy and extending the range of applicability of the method proposed in [32] are shown in Section 3.4. The multi-tone signal excitation technique and related interpolation techniques are shown in Section 3.5. The measurement set-up and case studies used to experimentally show the potential of the proposed methods are shown and described in Section 3.6. Finally, the experimental results of the proposed methods are shown and discussed in subsection 3.7. Final discussions are carried out in Section 3.8.

3.1 Theoretical framework of the analyzed method

Analytical solutions for axially symmetric eddy-current problems have been proposed and discussed in the scientific literature. Specifically, in a well-known paper by Dodd and Deeds [83] it is given a semi-analytical model for the eddy current computation for a coil above a single or multiple planar (infinite) conductive plates of finite thickness and different electrical conductivity.

Starting from this semi-analytical model, in [32–34] the authors proposed different probes, methods and processing algorithms, suitably developed for estimating

the thickness of non-magnetic materials. The proposed solutions are able to obtain thickness measurement accuracies compatible with industrial production standards [84] and low sensitivity to lift-off variations. Without loss of generality, the attention was focused on the double coaxial coil proposed in [33].

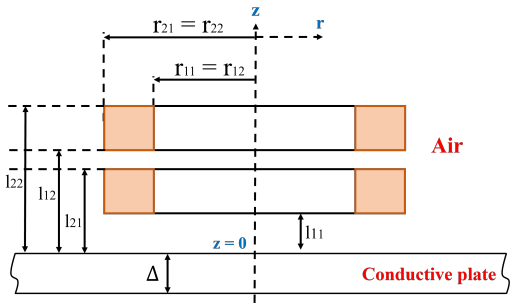

Figure 3.1: Representation of the axis-symmetrical coils placed on the infinite, planar and metallic plate [40].

In particular, it was considered a measuring system involving the use of two coils: one excitation coil and one pick-up coil. Given the geometry shown in Fig. 3.1, it is possible to calculate the mutual impedance between the two coils when they are placed on the plate ($\dot{Z}_{m,plate}$) or in the air ($\dot{Z}_{m,air}$), by the Dodd and Deeds model. Specifically, $\dot{Z}_{m,air}$ and $\dot{Z}_{m,plate}$ are given in Equation 3.1 and Equation 3.2:

$$\dot{Z}_{m,air} = K \int_0^\infty LCF \, d\alpha \tag{3.1}$$

$$\dot{Z}_{m,plate} = K \int_0^\infty L[C(F + \frac{EN}{D})] \, d\alpha \tag{3.2}$$

Where:

$$K = \frac{j\omega\pi\mu_0 N_1 N_2}{(l_{22} - l_{12})(l_{21} - l_{11})(r_{21} - r_{11})(r_{22} - r_{12})} \tag{3.3}$$

$$L = \frac{I(r_{11}, r_{21}) \cdot I(r_{12}, r_{22})}{\alpha^6} \tag{3.4}$$

$$C = e^{-\alpha l_{12}} - e^{-\alpha l_{22}} \tag{3.5}$$

$$F = e^{\alpha l_{21}} - e^{\alpha l_{11}} \tag{3.6}$$

$$E = -(e^{-\alpha l_{21}} - e^{-\alpha l_{11}}) \tag{3.7}$$

$$N = (\alpha\mu_R + \alpha_1)(\alpha_1 - \alpha\mu_R) + (\alpha\mu_r - \alpha_1)(\alpha_1 + \alpha\mu_r)e^{2\alpha_1\Delta} \tag{3.8}$$

$$D = (\alpha\mu_R - \alpha_1)(\alpha_1 - \alpha\mu_R) + (\alpha\mu_r + \alpha_1)(\alpha_1 + \alpha\mu_r)e^{2\alpha_1\Delta} \tag{3.9}$$

$$\alpha_1 = \sqrt{\alpha^2 + j\omega\sigma\mu_0} \tag{3.10}$$

N_1 and N_2 are the number of turns of the lower coil and the upper coil, respectively, $\omega = 2\pi f$ is the angular frequency being f the frequency of the excitation signal, σ is the electrical conductivity of the material, μ_0 is the magnetic permeability of the vacuum, μ_R is the relative magnetic permeability of the material, α is the spatial frequency, and Δ is the thickness of the sample. All the relevant geometrical parameters $l_{11}, l_{12}, l_{21}, l_{22}, r_{11}, r_{12}, r_{21}$ and r_{22} are described in Fig. 3.1. Starting from these formulas, Yin *et al.* related the thickness of a planar sample to a proper frequency. Specifically, in [32, 33] the authors proposed to identify the thickness of the sample by considering the real part of the variation of either the self-impedance or the mutual impedance due to the presence of the sample, divided by the angular frequency $2\pi f$, i.e. by considering

$$\frac{\Delta R}{\omega} = Re(-\frac{\dot{Z}_{m,plate}(f) - \dot{Z}_{m,air}(f)}{\omega}). \tag{3.11}$$

The thickness Δ of the sample is related to the frequency f_{min} where $\frac{\Delta R}{\omega}$ achieves its minimum (as shown in Fig. 3.2), hereafter referred as the "peak frequency". Specifically, the thickness can be evaluated as discussed in [32]:

$$\Delta = \frac{2\alpha_0}{\sigma\mu_0\omega_{min}} \tag{3.12}$$

where α_0 is a proper constant related to the geometry of the probe, lift-off and tilting and it is defined as "characteristic spatial frequency". This quantity can be evaluated numerically or experimentally as it will be shown in the next Sections.

In the next sections the two limits of the method previously described are discussed. In particular, the non-constancy of the parameter α_0 is in-depth analyzed in the next Section (Section 3.2) [39], while the analysis related to the measurement times linked to the estimation of ω_{min} are shown in the Section 3.3 [40].

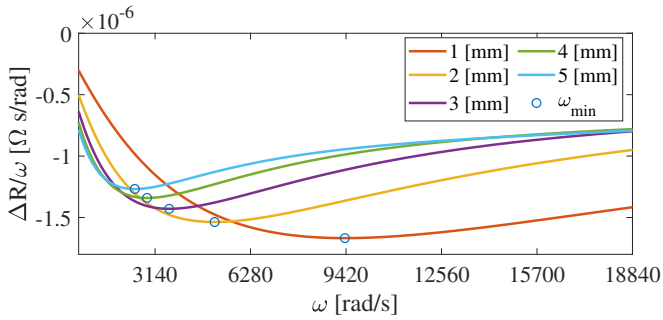

Figure 3.2: The $\Delta R/\omega$ ratio as a function of ω. Here $\sigma = 18.8$ MS/m and the probe is described in Section 3.6 [39].

3.2 The non-constancy of the α_0 parameter and the introduction of the critical thickness

3.2.1 The non-constancy of the α_0 parameter

Starting from the approach proposed by Dodd and Deeds [83], the Equation (3.12) (shown in [32]) was obtained by means of a stationary-phase approach applied to the analytical solution for the eddy current problem in a plate.

This approximation is valid as long as

$$\alpha_0 \Delta \ll 1, \tag{3.13}$$

a condition which is met when the probe coil diameter is much larger than Δ, as stated in [32]. This condition makes it necessary to change the probe size when measuring plates of different thicknesses. It is also a problem when measuring the thickness of thick plates. This requires a large coil, resulting in space requirements and other problems.

To overcome the intrinsic limits of (3.12), it was derived a new thickness estimation equation called the Fundamental Thickness Equation (FTE), with an entirely new and original approach based on the celebrated Buckingham's π theorem [39, 51]. The FTE considers all the relevant physics without any approximation, overcoming all the limits of the former. It only requires the knowledge of a function that can be easily evaluated once and for all through numerical simulations or experimental measurements.

Below it is defined δ_{min} as the skin-depth in the conducting material evaluated at the angular frequency ω_{min}

$$\delta_{min} = \sqrt{\frac{2}{\sigma \mu_0 \omega_{min}}}. \tag{3.14}$$

The following theorems are shown below; they are based on the results shown in [39].

Theorem 1. *Given the geometry of the probe described by the array of parameters* $\mathbf{p}$*, the probe lift-off* l_0 *and the tilting* θ *of the probe with respect to the plate, the thickness* Δ *satisfies the following equation*

$$\omega_{min} \sigma \mu_0 D^2 = h\left(\frac{\Delta}{D}, \frac{l_0}{D}, \theta, \mathbf{p}\right), \tag{3.15}$$

where D *is the size of the probe and* $h(\cdot)$ *a proper function.*

The (3.15) is defined as the Fundamental Thickness Equation. It is important to remark that the FTE (3.15) involves function $h(\cdot)$, which can be evaluated numerically. Specifically, given the probe geometry ($\mathbf{p}$ and D), the lift-off l_0 and the tilting θ, function $h(\cdot)$ depends only on thickness Δ and it may be precomputed and stored.

In addition, it is worth noting that the FTE (3.15) could be derived directly from the Dodd and Deeds analytical representation [83], but dealing with that analytical representation is somewhat involved. Moreover, the method proposed to derive (3.15) is completely general, independent of the underlying geometry, and it can be applied without major changes to other geometrical configurations, such as pipes.

Theorem 1 is complemented by the following results concerning the asymptotic behaviour for $\Delta/D \to 0^+$ and for $\Delta/D \to +\infty$.

Theorem 2. *Given the geometry of the probe described by the array of parameters* $\mathbf{p}$*, the probe lift-off* l_0 *and the tilting* θ *of the probe with respect to the plate,* ω_{min} *satisfies the following relationships*

$$\omega_{min} \sigma \mu_0 D \Delta \sim h_0\left(\frac{l_0}{D}, \theta, \mathbf{p}\right), \text{ for } \Delta/D \to 0^+, \tag{3.16}$$

$$\omega_{min} \sigma \mu_0 D^2 \sim h_\infty\left(\frac{l_0}{D}, \theta, \mathbf{p}\right), \text{ for } \Delta/D \to +\infty, \tag{3.17}$$

where D *is the size of the probe, and* $h_0(\cdot)$ *and* $h_\infty(\cdot)$ *proper functions.*

The proofs of Theorems 1 and 2 are given in [39]. The connection between Theorems 1 and 2 and equation (3.12) is obtained by multiplying both sides of (3.15) by Δ, which gives

$$\Delta = \delta_{min}^2 \alpha(\Delta), \tag{3.18}$$

where

$$\alpha(\Delta) = \frac{\Delta}{2D^2} h\left(\frac{\Delta}{D}, \frac{l_0}{D}, \theta, \mathbf{p}\right). \tag{3.19}$$

Hereafter, for the sake of simplicity, it is understood that $\alpha(\cdot)$ depends on Δ, D, $\mathbf{p}$, l_0 and θ. Equation (3.18) is simply (3.15) cast in a form close to (3.12). It replaces and generalizes (3.12).

Theorem 2 can be "translated" in terms of the function $\alpha(\cdot)$. Specifically, (3.16) combined with (3.18) gives

$$\alpha(\Delta) \sim \frac{1}{2D} h_0\left(\frac{l_0}{D}, \theta, \mathbf{p}\right), \text{ for } \Delta/D \to 0^+, \tag{3.20}$$

and, similarly, (3.17) gives

$$\alpha(\Delta) \sim \frac{\Delta}{2D^2} h_\infty\left(\frac{l_0}{D}, \theta, \mathbf{p}\right), \text{ for } \Delta/D \to +\infty. \tag{3.21}$$

Equation (3.20) implies that $\alpha(\Delta)$ approaches a constant limit for small Δ. This proves that (3.12) corresponds to (3.18) in the limit for $\Delta \ll D$. Equation (3.21) implies that $\alpha(\Delta)$ is proportional to Δ, for large Δ.

Fig. 3.3 shows the complete behaviour of $\alpha(\Delta)$ for a range of thicknesses of interest from 0.01 mm up to 25 mm, together with its constant approximation for $\Delta \ll D$. It is fairly evident that $\alpha(\cdot)$ cannot be retained constant with respect to the thickness Δ.

Moreover, it is worth noting that $\alpha(\cdot)$ does not depend on the electrical conductivity, as it clearly follows from (3.19).

Function $\alpha(\cdot)$ represents the "signature" of a given probe for a given lift-off and tilting. To compute it numerically, we express $\alpha(\Delta)$ as:

$$\alpha(\Delta) = \frac{\sigma \mu_0 \omega_{min} \Delta}{2}. \tag{3.22}$$

Then, it was numerically evaluated ω_{min} for different values of Δ and/or electrical conductivities σ, and plug these values into (3.22). In this case, the analysis was carried out numerically, by means of the well-known Dodd and Deeds semi-analytical model [83] but a generic numerical tool can also be adopted without loss of relevance.

It is worth noting that the FTE (3.15) or (3.18) allows a clear factorization of the effects due to the geometry and the material. Specifically, $h(\cdot)$ and $\alpha(\cdot)$

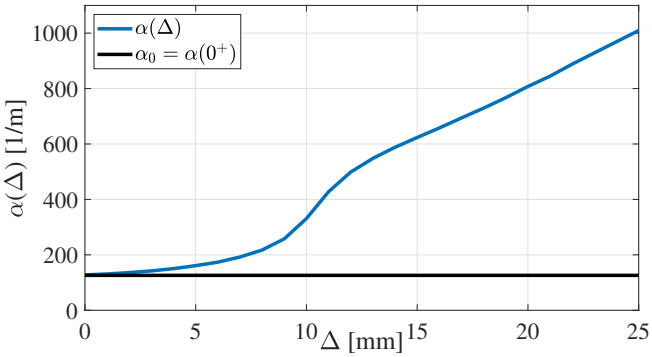

Figure 3.3: Complete behaviour of $\alpha(\Delta)$ for the probe of Section 3.6 (blue line), together with its constant approximation ($\alpha_0 = 126.28$ m^{-1}) valid for small Δ/D (black line) [39].

account for the geometry of the problem, whereas δ_{min} accounts for the material properties (σ and μ_0), other than the angular frequency ω_{min} where the minimum is achieved.

It is important to highlight that Equation (3.18) can be written as

$$\omega_{min} = \frac{\alpha(\Delta)}{2\mu_0\sigma\Delta}. \tag{3.23}$$

Equation (3.23), combined with the typical plot of Fig. 3.3 and the asymptotic behaviours of (3.20) and (3.21), shows that ω_{min} is inversely proportional to the unknown thickness Δ for $\Delta/D \ll 1$; then, ω_{min} decreases with Δ at a decreasing rate until it becomes constant for $\Delta/D \gg 1$. Moreover, if it is known a priori that the unknown thickness is in the range $[\Delta_1, \Delta_2]$, then the proper frequency range for collecting the measurements is $[\omega_1, \omega_2]$, where $\omega_k = \alpha(\Delta_k)/(2\mu_0\sigma\Delta_k)$.

3.2.2 The introduction of the critical thickness

The enhanced equation (3.18) makes it possible to evaluate the limits of applicability of the method proposed in [32–34].

To this purpose, we observe that solving (3.18) entails finding the intersection in the (Δ, α) plane between the straight line Δ/δ_{min}^2 and the function $\alpha(\Delta)$.

When the straight line is tangential to the graph of the function $\alpha(\Delta)$ (see Fig. 3.4 (a)), the abscissa of the tangent point defines a thickness value, termed the critical thickness Δ_c, and the skin-depth (δ_{min}) for the tangent line is termed as the critical skin-depth or, in short, δ_c.

In general, equation (3.18) admits a solution if and only if the slope of the straight line Δ/δ_{min}^2 is higher than that of the tangent line, i.e. if and only if $\delta_{min} < \delta_c$. In this case, the method gives multiple solutions (Δ_P and Δ_S shown Fig. 3.4 (b)). However, by restricting the method to the interval $(0, \Delta_c)$, the uniqueness of the solution is restored.

The critical thickness Δ_c is an important parameter because it represents the upper limit of applicability of the method. Δ_c depends on the function $\alpha(\cdot)$ which, in turns, depends on the probe. Δ_c can be used to properly select the probe, according to the range of thicknesses of interest.

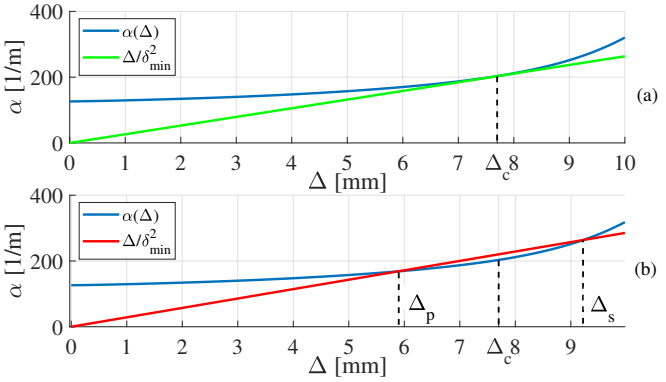

Figure 3.4: Geometrical definition of the critical thickness Δ_c (a); at any higher slope ($\delta_{min} < \delta_c$) of the straight line we have only one intersection in the interval $[0, \Delta_c]$ (b) [39].

Connected to the critical length Δ_c is the concept of critical angular frequency ω_c, which is defined as

$$\omega_c = \frac{\alpha(\Delta_c)}{2\mu_0\sigma\Delta_c}. \tag{3.24}$$

The critical angular frequency ω_c represents the smallest angular frequency where $\Delta R(\omega)/\omega$ may achieve its minimum. This value can be chosen to set the lower limit of the frequency range where the measurements need to be collected.

3.3 Analysis of measurement time

In order to obtain the good accuracies described in [32], the measurement time represents a major limitation in the in-line and real-time measurement scenario. Reasonable times to carry out a thickness measurement can be in the order of few

Table 3.1: Retive measurement error in thickness estimation obtained in [32].

Type of probe	Analyzed material	Actual thickness (Δ) [mm]	Relative measurement error (e_Δ) [%]
Air-cored Coil	Copper	0.022	0.40
		0.044	2.50
		0.066	1.89
		0.088	2.75
		0.110	-1.65
		0.132	-2.61
U-cored coil	Aluminum	1.000	-0.37
		2.000	-0.53
		3.000	-1.48
		4.000	0.59
		5.000	1.41

seconds. However, when the unknown thickness varies in a "extended" range, it can be necessary to perform a large frequency scan.

A measurement method based on swept-sine signal turn out to be time-consuming. Moreover, the typical measurement accuracy prescribed by standards [84] calls for a excitation frequency scan with a proper "small" step $\Delta f = \Delta\omega/2\pi$, requiring the use of a high number of tones to scan a large excitation frequency range. In [32], measurement results for copper and aluminum plates with constant lift-off value and different types of probes are discussed. The accuracy provided by these measurements are in the range of $\pm 3\%$, as shown in Table 3.1.

To evaluate the larger value for Δf which provides the prescribed metrological performances of [32], it was performed a parametric analysis. It was assumed a frequency range from 100 Hz to 5000 Hz with a frequency resolution of 5 Hz. This frequency range is suitable for samples with thicknesses ranging from 0.35 mm to 6 mm (at σ equal to 18 MS/m), or samples with thicknesses ranging from 0.1 mm to 5 mm (at σ equal to 59 MS/m), as one can find by means of the semi-analytical model by Dood and Deeds described in Section 3.1.

The thickness estimation error in the following analysis was evaluated by only taking into account the contribution due to effect of Δf in the estimation of the peak frequency $f_{min} = \omega_{min}/2\pi$, and considering negligible all the other effects (e.g., measurement setup and noise on the measured signals in the evaluation of $\Delta R/\omega$, and so on). Table 3.2 shows the percentage thickness estimation error (e_Δ) versus the frequency resolution, for ten different thickness values.

The e_Δ values have been estimated as detailed in the following:

- Given the actual thickness (Δ_{ac}) and the electrical conductivity (specifically 58.7 MS/m, typical electrical conductivity of copper, has been used), the peak frequency ($f_{min,ac}$) can be estimated by using the semi-analytical model and the geometrical system described in Section 3.1 (Equation 3.11);

Table 3.2: Analysis of the relative thickness estimation error (Δ_c) for different values of frequency resolution (Δf) considering a frequency range from 100 Hz to 5 kHz [40].

	Actual Thickness (Δ) [mm]					
		0.1	0.2	0.3	0.4	0.5
Frequency resolution (Δf) [Hz]	2	± 0.02 %	± 0.04 %	± 0.06 %	± 0.09 %	± 0.11 %
	5	± 0.06 %	± 0.11 %	± 0.17 %	± 0.22 %	± 0.27 %
	10	± 0.12 %	± 0.22 %	± 0.33 %	± 0.44 %	± 0.55 %
	Actual Thickness (Δ) [mm]					
		1	2	3	4	5
Frequency resolution (Δf) [Hz]	2	± 0.11 %	± 0.22 %	± 0.31 %	± 0.39 %	± 0.46 %
	5	± 0.28 %	± 0.54 %	± 0.78 %	± 0.98 %	± 1.14 %
	10	± 0.56 %	± 1.08 %	± 1.54 %	± 1.94 %	± 2.26 %

- Given the peak frequency $f_{min,ac}$, the new values $f_{min,1}$ and $f_{min,2}$ are evaluated by subtracting/adding the value of the considered frequency resolution ($f_{min,1} = f_{min,ac} - \Delta f$ and $f_{min,2} = f_{min,ac} + \Delta f$);
- Using Equation 3.18, the new thickness values ($\Delta_{min}(f_{min,2})$ and $\Delta_{max}(f_{min,1})$) are estimated;
- The relative thickness estimation errors are estimated as: $e_\Delta = \pm(\Delta_{max} - \Delta_{min})/\Delta_{min} \cdot 100$.

As confirmed by Table 3.2, the relative thickness estimation error increases with the frequency resolution and the thickness. Similar performances to those of Table 3.1 can be achieved by using a frequency resolution less than 5 Hz.

In view of practical applications, it is relevant to analyze the time required to carry out the whole measurement process. The analysis is made by considering two measurement solutions: *(b)* the impedance analyzer used in [32] to obtain the performances shown in Table 3.1 (similar results can be obtained considering other impedance analyzers), and *(bb)* a general-purpose device able to generate the excitation signal and acquire the desired quantities. The accuracy performance in the thickness measurement depends on the characteristics of the used device and on the adopted processing algorithm but the minimum measurement time can be independently estimated, as detailed in the following.

Regarding the first approach, that is the impedance analyzer of [32], the relevant parameters of the impedance analyzer are the delay time (Dl) and the integration time (IT). As sketched in Fig. 3.5, the Dl is the time needed to stabilize the response after the frequency change (it can be set from 0 to 105 s); the IT defines the time interval during which the analyzer measures the input signals. It is fun-

damental for the rejection of harmonics and noise (it can set from 10 ms to 105 s).

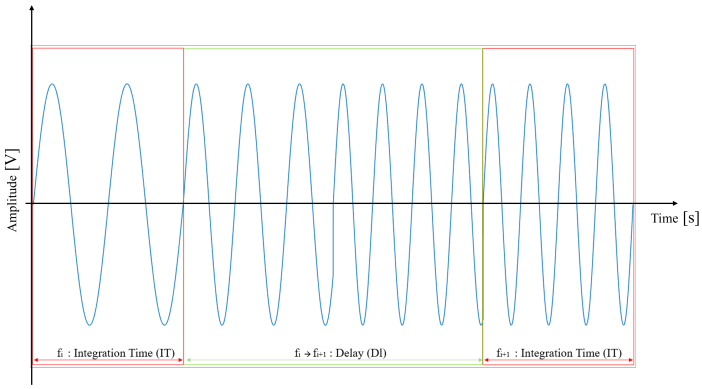

Figure 3.5: Representation of Integration Time (IT) and Delay (Dl) in a swept-sine application during the transition from the frequency f to the frequency $f + \Delta f$ (where Δf is the chosen frequency resolution) [40].

To compute the minimum time required to measure the thickness, it was considered a minimum value of 10 ms for the IT, a value of Dl corresponding to 4 periods of the excitation waveform, that represents the minimum number of periods to get a stable response after the frequency changes and excluding the time to acquire and process the signals. In [40], it was shown that the minimum thickness measurement time MMT_{IMP} using the impedance analyzer for 5 Hz of frequency resolution requires 12.96 s.

For the second approach, a delay time equal to the previous one and a variable integration time equal to two periods of the considered excitation frequency, corresponding to the minimum number of periods to extract the desired quantities from the signals, have been considered. Adopting these values for Dl and IT, the minimum thickness measurement time MMT_{GP}, using the general-purpose device, were about 9.1 s for a $\Delta f = 5$ Hz [40]. Despite these measurement times have been obtained under ideal conditions (e.g., considering minimum number of signal cycle to be processed, zero processing time, etc.), they cannot be considered proper in online controls in production processes.

3.4 Proposed measurement optimizations: iterative and analytical algorithms

In this Section, two algorithms are in-depth described in order to solve the FTE (3.18). This procedure was developed to make the approach suitable for the industrial environment, where automated measurements are required with minimal a priori knowledge of the nominal thickness of the metal plates.

Both algorithms are based on a preliminary evaluation of the $\alpha(\cdot)$ function in the thickness range of interest, for the given probe geometry, lift and tilt. This preliminary evaluation, done only once, can be done through an experimental, numerical or mixed procedure (i.e. considering both experimental and numerical points).

The first algorithm to solve (3.18) is iterative and it is described in the following subsection 3.4.1 while the second analytical algorithm is described in subsection 3.4.2 .

3.4.1 The iterative algorithm

The iterative approach is proposed in order to obtain the proper value of the unknown thickness Δ, taking into account the fundamental thickness equation (3.18), where $\alpha(\Delta)$ was introduced. As mentioned in Section 3.2, $\alpha(\cdot)$ is assumed to be available in the range of interest.

The estimated thickness via the iterative method is obtained by the following steps:

1. **Measurement**: measure ω_{min}, the angular frequency where $\Delta R(\omega)/\omega$ achieves its minimum.
2. **Initialization**: compute δ_{min} according to (3.14), set $i = 1$ and select an arbitrary Δ_1 in the interval $(0, \Delta_c)$.
3. **Update of Δ**: update Δ as
$$\Delta_{(i+1)} = \delta_{min}^2 \, \alpha(\Delta_i). \tag{3.25}$$
4. **Stopping criterion**: if $|\Delta_{(i+1)} - \Delta_{(i)}| < e$ set $\Delta = \Delta_{(i+1)}$ and exit. Otherwise, set $i = i + 1$ and go to step 3.

In step "*Stopping criterion*", $e > 0$ is an absolute error tolerance used for the stopping criterion.

The algorithm described in steps 1-4 is simply a fixed point method to solve the fixed point equation (3.18). In addition, it converges to the proper solution,

regardless of the choice of initial point $\Delta_1 \in (0, \Delta_c)$, as shown in Fig. 3.6 and discussed in [39].

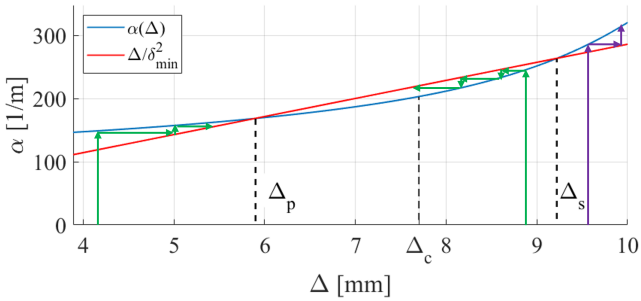

Figure 3.6: Evidence of the convergence of the iterative solution. For any initial point smaller than the second roots Δ_s the algorithm converges to the primary root $\Delta_p < \Delta_c$. After Δ_s the iterative scheme does not converge. Since the value of Δ_sn is not known, the iteration is initialized with $\Delta_1 < \Delta_c$ [39].

Few iterations are usually necessary to achieve a proper convergence. For example, considering the test conditions defined in Section 3.2 ($\Delta_{min} = 0.1$ mm, $\Delta_{max} = 7$ mm), and assuming an unknown thickness of 2 mm and a threshold e equal to 15 μm, Figure 3.7 shows that the correctly estimated thickness is obtained in only three steps. Specifically, starting with an initial error on the thickness estimation of 11.80%, the iterative solution is reduced to 0.78% in only three steps.

In short, the inclusion of this iterative solution in the proposed ECT-based thickness measurement method allows the accuracy of the final thickness measurement to be greatly improved with minimal computational effort. In fact, the time taken by the iterative solution can be considered negligible, as it depends on only a few accesses to a look-up table/interpolation rule that generates the $\alpha(\cdot)$ values.

3.4.2 The analytical algorithm

In this Section the proposed analytical algorithm is described and analyzed. This is based on a polynomial approximation of the function $\alpha(\cdot)$, the latter assumed to be known, as mentioned at the beginning of this Section. The minimum number of samples of $\alpha(\cdot)$ required to calculate the polynomial coefficients, depends on the degree of polynomial approximation.

In analytical terms, this is:

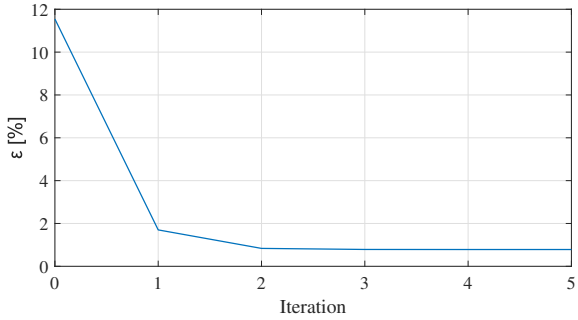

Figure 3.7: Plot of the percentage relative error on the estimate of the thickness, as a function of the number of iterations [39].

$$\alpha(\Delta) \approx \sum_{i=0}^{N} c_i \cdot (\Delta - \Delta_0)^i \tag{3.26}$$

where the c_is are the polynomial coefficients and Δ_0 is the point of expansion of this approximation. When $N = 0$ and $\Delta_0 = 0$ we have the approximation underlying (3.12) It is worth noting that Approximation (3.26) makes the FTE (3.18) an algebraic equation.

The thickness estimated by the analytical method is obtained through the following steps:

1. **Measurement**: measure ω_{min}, the angular frequency where $\Delta R(\omega)/\omega$ achieves its minimum.

2. **Initialization**: compute δ_{min} according to (3.14).

3. **Computation of** Δ: solve equation

$$\Delta = \delta_{min}^2 \sum_{i=0}^{N} c_i \cdot (\Delta - \Delta_0)^i. \tag{3.27}$$

It is interesting to note that the algebraic equation (3.27) can be solved in real time with current computational resources.

A very useful and interesting case is that of $N = 2$. In this case (3.27) for $\Delta_0 = 0$ reduces to:

$$\frac{\Delta}{\delta_{min}^2} = c_0 + c_1 \cdot \Delta + c_2 \cdot \Delta^2. \tag{3.28}$$

The analytical solution of (3.28) is:

$$\Delta = \frac{-\left(c_1 - \delta_{min}^{-2}\right) - \sqrt{\left(c_1 - \delta_{min}^{-2}\right)^2 - 4c_0c_2}}{2c_2}, \tag{3.29}$$

where the sign of the square root is chosen to have the physically admissible solution, which is smaller that Δ_c. Moreover, a simple calculation carried out under this second order approximation gives $\Delta_c = \sqrt{c_0/c_2}$.

From a general perspective, it is necessary to choose the degree N of the interpolant based on a compromise between the ease in computing the solution of (3.27) and the residual error in approximation (3.26). For this purpose, it is useful to calculate approximation errors in terms of the quadratic error (RMSE), defined as:

$$RMSE = \sqrt{\frac{\sum_{i=1}^{K}\left[\hat{\alpha}(\Delta_i) - \alpha(\Delta_i)\right]^2}{K}} \tag{3.30}$$

where $\hat{\alpha}(\cdot)$ is the approximating polynomial, Δ_i is the $i-$th sampling point, and K is the total number of samples.

Table 3.3 reports the RMSE for different values of the order of the polynomial approximation N, for the same case described above. It can be highlighted that for $N = 4$ (fourth order polynomial) the RMSE reaches its plateau, where the approximation error is not larger than the numerical errors in computing the function $\alpha(\cdot)$. A higher order polynomial would not improve the overall accuracy, despite requiring a higher computational cost.

Table 3.3: RMSE values obtained with the considered thickness range versus different degrees of the interpolating polynomial [39].

Polynomial degree	**RMSE [1/m]**
1	3.961
2	0.742
3	0.365
4	0.348
5	0.349
6	0.349

As a final comment, it is pointed out that the approximation (3.26) is very interesting when the function $\alpha(\cdot)$ is acquired experimentally. In fact, the c_i of the expansion (3.26) can be found through a minimum set of $N + 1$ measurements, performed on plates of known thickness and electrical properties. Furthermore,

this experimental characterisation does not require exact knowledge of the probe geometry, making this approach the only option when the $\alpha(\cdot)$ function cannot be calculated numerically, due to lack of knowledge of the probe or uncertain parameters.

3.5 Proposed measurement optimizations: multi-sine excitation and interpolation techniques

As shown in Section 3.3, in view of industrial applications, the method proposed in [32] has two main challenges: the measurement time and the measurement accuracy. The aim of this Section is to show the solutions developed to reduce measurement times while maintaining constant measurement accuracy. The optimisation strategy is proposed in subsection 3.5.1, while the design of the multi-tone excitation signal is explained in detail in subsection 3.5.2. Finally, the proposed interpolation techniques are shown and analyzed in subsection 3.5.3.

3.5.1 Proposed Dual-Stage strategy

In order to reduce the measurement time and improve accuracy in the evaluation of metal plate thickness, multi-sine signals can be adopted. However, the maximum number of tones to be used is limited by the total RMS value of the excitation signal, due to sensor heating and power consumption, which is a major disadvantage of battery-powered instrumentation. For these reasons, the choice of an appropriate number of tones, combined with frequency interpolation techniques, is mandatory. In particular, to account for the finite frequency resolution of multi-sine signals and improve the accuracy of the measurement method, several interpolating polynomials were analysed and applied in this work.

The final goal is to obtain a more accurate estimate of the peak frequency value. The proposed interpolation techniques were first developed and validated through numerical simulations and then tested experimentally.

For a further improvement of the thickness measurement accuracy, the use of a double-stage strategy of excitation and processing was proposed. In Fig. 3.8 is shown the flow chart that describe the proposed strategy.

In particular, the dual stage strategy is organized as follows:

- in a first stage, the goal is to find the range where the peak frequency ($f_{min,1}$) is located, by using a multi-sine signal with a wide frequency range (this first step is optional and can be jumped if the nominal thickness and, consequently, the ($f_{min,1}$) value is a priori known). In this stage the excitation frequencies are allocated on a logarithmic scale;

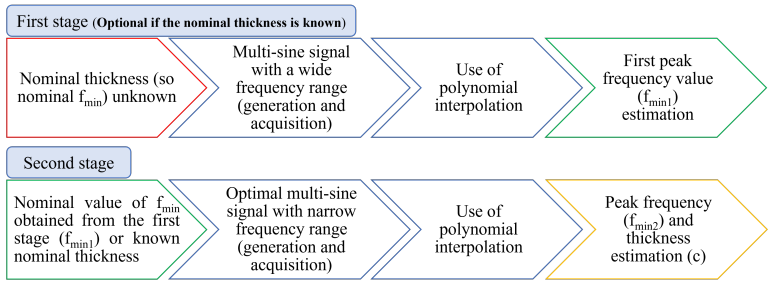

Figure 3.8: Operation flow-chart behind the dual stage strategy [40].

- in a second stage, another multi-sine signal over a narrow and optimized frequency range centered on the estimate of the peak frequency ($f_{min,1}$), obtained in the first step or known a priori from the knowledge of the nominal thickness of the sample. In this stage the excitation frequencies are distributed uniformly.

In both stages, interpolating polynomials are essential to filter the noisy measurements and interpolate the data to get an accurate estimate of the peak position. Adopting this dual-stage strategy, the resulting measurement time is less than 3 seconds.

3.5.2 Development and design of the multi-tone excitation signal

As mentioned also by the authors in [33], the solution to reduce the measurement time is the use of multi-frequency signals processed by Fast-Fourier Transform (FFT). The general expression of a multi-sine signal is:

$$I(t) = \sum_{k=1}^{N_s} \sqrt{2} \cdot I_k \cdot sin(2 \cdot \pi \cdot f_k \cdot t + \phi_k) \tag{3.31}$$

where I_k, f_k and ϕ_k are the Root Mean Square (RMS), frequency and phase of the $k-th$ sinusoid, and N_s is the total number of tones. Under the same conditions of the previous analysis (Section 3.3) of the measurement time (frequency range from 100 Hz to 5000 Hz and frequency resolution of 5 Hz), the multi-frequency excitation current signal is composed by a high number of tones (N_S=981). The total RMS value (I_{RMS}) of the excitation current is given by:

$$I_{RMS} = \sqrt{\sum_{k=1}^{N_s} I_k^2} \tag{3.32}$$

If the multi-sine excitation signal is composed by tones with equal RMS values, then the total RMS value of the excitation current is equal to $I_{RMS} = \sqrt{N_S} \cdot I_k$. This means that for a prescribed total RMS current value I_{RMS}, the RMS current value for each tone is equal to $I_k = I_{RMS}/\sqrt{N_S}$, for instance for I_{RMS}=100 mA we have $I_k \cong 3$ mA.

For this reason, multi-sine excitation signals aiming to reduce the measurement time must be carefully designed to achieve an adequate compromise between the number of tones, i.e. the frequency resolution, the maximum RMS value of the total excitation current and the minimum RMS value of each tone. It is also worth noting that the maximum RMS value is limited by the maximum current supported by both the excitation coil and the drive electronics, which is particularly important for battery-powered portable instruments. Similarly, the minimum RMS value for each tone is important in order to achieve adequate stimulation of the material at that specific tone.

From the research group's experience in this field [85, 86], the multi-sine excitation signal can be optimized varying the phase value shown in Equation 3.31 if the considered tones are linearly spaced. In particular, if the phase ϕ_k appearing in 3.31 is given by:

$$\phi_k = -\pi \cdot \frac{k(k-1)}{N_S}, \tag{3.33}$$

then the resulting signal has a fairly constant envelope, an essential feature to optimize both the peak amplitude of the current delivered to the exciter probe and the full scale of the analogue-to-digital converter of the acquisition board[85, 86].

The choice of the number of tones for each phase is intended to balance the energy content of the excitation signal (limited by the peak power of the probe and/or the entire measurement system) and the number of frequency points required to achieve adequate accuracy in estimating the peak frequency. In the first stage, a signal with a lower energy content was considered, as it is sufficient to estimate the frequency range in which the peak occurs. In contrast, in the second stage, the frequency range of interest is smaller, as is the number of tones required. Therefore, the RMS value for each individual tone of the excitation signal can be increased.

For the chosen configuration, two different excitation signals were designed. For the first stage, a 19-tone multisine signal was designed with a semi-logarithmic frequency distribution in the range 100 Hz - 5000 Hz. As already mentioned, this

frequency range is suitable for samples with thicknesses between 0.35 mm and 6 mm (at σ equal to 18 MS/m) or samples with thicknesses between 0.1 mm and 5 mm (at σ equal to 59 MS/m). For the second stage, an 11-tone multi-sine signal was designed. The center frequency of the multi-sine signal is that of the peak found either in the first stage, or that arising from the nominal value of the thickness. The multi-sine signal covers a frequency range from -30% to +30% of the center frequency.

3.5.3 Analysis of the proposed interpolation techniques

The reduction in the number of selected frequency points can be exploited by using appropriate interpolating polynomials. The selection of the optimal interpolating polynomial allows for higher performance in estimating the peak frequency value and, thus, the thickness of the sample.

In [40], four different types of interpolation techniques have been considered:

- Forth Order Interpolating Polynomial (FOIP);
- Forth Order Chebyshev Interpolating Polynomial (FOCIP);
- Modified Akima Interpolator Polynomial (MAIP);
- Piecewise Cubic Hermite Interpolator Polynomial (PCHIP).

Note that for the purposes of comparison, two different classes of interpolation techniques were considered. The first class (which includes FOIP and FOCIP) uses the entire dataset to determine the polynomial equation, whereas the second class (which includes MAIP and PCHIP) determines the polynomial equation not by considering the entire dataset, but by dividing it into many subsets in which the polynomial equation is determined (piecewise interpolation techniques). Below are some characteristics of the interpolation techniques analyzed.

A basic interpolating polynomial consists of interpolating a given data set with the lowest possible degree polynomial passing through all points in the data set. A FOIP was chosen for this study, given the number of points available for the data set and the resulting R-squared values (closest to unity) and lowest values of quadratic error. Consequently, the resulting fourth-order polynomial can be defined as:

$$p_4(x) = a_4x^4 + a_3x^3 + a_2x^2 + a_1x + a_0, \tag{3.34}$$

where $a_0, ..., a_4$ are the coefficients of the equation, x is the unknown variable and $p_4(x)$ is the interpolation polynomial.

The Chebyshev interpolating polynomial is a sequence of orthogonal polynomials related to De Moivre's formula [87], with several properties that make them extremely useful when approximating functions are investigated. A FOCIP has been chosen for this study, to compare same order polynomial interpolations. As a result, the FOCIP formulation is:

$$p_4(x) = U_4^*(x) = \frac{sin(5\theta)}{sin(\theta)}, \tag{3.35}$$

with:

$$cos(\theta) = \frac{2x - (a+b)}{b-a}, \tag{3.36}$$

where $\theta \in [0, \pi]$.

$U_4^*(x)$ is the second-kind Chebyshev polynomial of forth degree, and $x \in I$ is the unknown variable defined over the interval $I = [a, b]$.

The Akima interpolating algorithm performs cubic interpolations to realize piecewise polynomials with continuous first-order derivatives [88, 89]. The MAIP algorithm avoids excessive local ripples and, unlike the classic Akima algorithm, assigns an average weight to the points on both sides, to avoid possible undulation phenomena. The interpolating expression for a portion of curve between two consecutive points can be found in [88]. If we have an interval between two points $(x_1, y_1\ )$ and (x_2, y_2), being t_1, t_2 the slopes at these two points, a third-degree polynomial can be uniquely determined:

$$p(x) = a_0 + a_1(x - x_1) + a_2(x - x_1)^2 + a_3(x - x_1)^3, \tag{3.37}$$

where:

$$a_0 = y_1, \tag{3.38}$$

$$a_1 = t_1, \tag{3.39}$$

$$a_2 = \frac{[3(y_2 - y_1)/(x_2 - x_1) - -2t_1 - t_2]}{(x_2 - x_1)}, \tag{3.40}$$

$$a_3 = \frac{[t_1 + t_2 - 2(y_2 - y_1)/(x_2 - x_1)]}{(x_2 - x_1)^2}, \tag{3.41}$$

The cubic Hermite interpolator PCHIP is a spline where each piece is a specified third-degree polynomial in the form of Hermite, i.e. by its values and first derivatives at the end points of the corresponding domain interval [90]. Let $\pi : a = x_1 <$

$x_2 < ... < x_n = b$ be a partition of the interval $I = [a, b]$. Let $f_i : i = 1, 2, \ldots, n$ be a given set of monotone data values at the partition points. For instance, let us assume $f_i \leq f_{i+1} (i = 1, 2, \ldots, n-1)$. It can be constructed on π a piecewise cubic function $p(x)$, such that, in each sub-interval $I_i = [x_i, x_{i+1}]$, $p(x)$ is a cubic polynomial represented as:

$$p(x) = f_i H_1(x) + f_{i+1} H_2(x) + d_j H_3(x) + d_{j+1} H_4(x), \tag{3.42}$$

where:

$$d_j = p'(x_j) \tag{3.43}$$

for $j = i, i+1$ and $H_k(x)$ for $k = 1, ..., 4$ are the so-called cubic Hermite basis function for the interval I_i [90].

3.6 Measurement set-up and case studies

A schematic block diagram of the measurement set-up is shown in Fig. 3.9. The experimental set-up comprises by the following components: an Eddy Current Probe (ECP), a Waveform Generator, a data Acquisition Board, a Current Probe and two Signal Amplifiers. The ECP consists of two coaxial coils, the upper coil used as the transmitting coil (Tx) and the lower coil as the receiving coil (Rx). The coils' geometry is shown in detail in Fig. 3.10; their dimensions are given in Table 3.4.

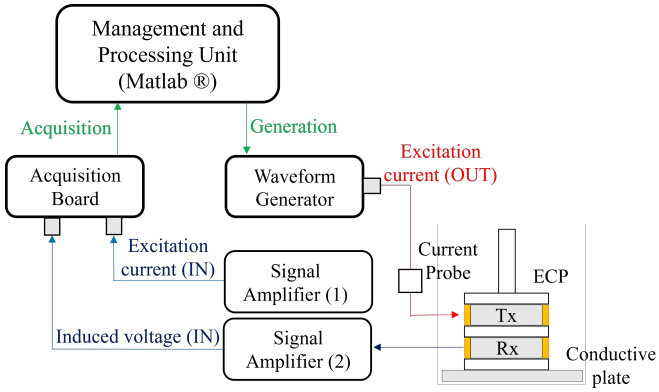

Figure 3.9: Block diagram of the adopted measurement set-up [39].

A Waveform Generator Agilent 33120A is used to provide the excitation current to the Tx. The excitation current has been sensed by means of a current probe

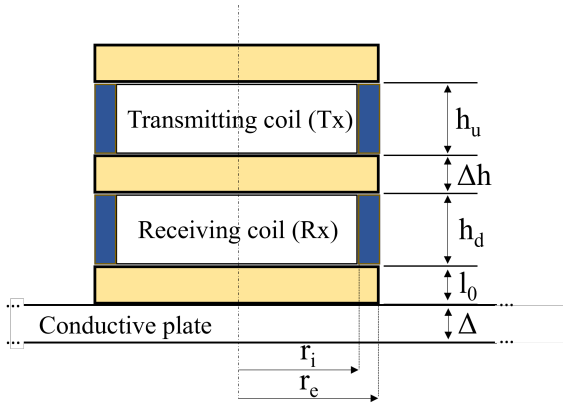

Figure 3.10: Eddy Current Probe geometry. The coil windings (blue) together with the plastic holder in (yellow) [39].

Table 3.4: Geometric parameters of the adopted Eddy Current Probe [39].

r_i [mm]	11.8
r_e [mm]	12.2
$h_u = h_d$ [mm]	3
Δh (gap) [mm]	1
l_0 (lift-off) [mm]	0.5
$N1 = N2$ (number of turns)	20

Tektronix TCP202A, and both the sensed excitation current and the induced voltage on the receiving coil Rx were conditioned using two SR560 Stanford Research System low-noise amplifiers, which amplify and filter the signals. An Acquisition board TIE-PIE Engineering Handyscope HS5-540XMS-W5(TM) is used to acquire both the conditioned signals with a sampling frequency of 1000 times the frequency of the exciting signal and 14 bits of resolution. The tests were carried out by feeding the exciting coil with a sinusoidal frequency-swept signal. The range of frequencies of interest was from 200 Hz to 3 kHz, with a resolution of 2 Hz and with a root mean square current value of 135 mA. The Management and Processing unit includes a MATLAB algorithm running on a dual-core PC for processing the acquired data, managing both the Waveform Generator and the acquisition board TIE-PIE.

The experimental tests were carried out considering six reference aluminum plates, whose nominal thickness values, electrical conductivities, and dimensions are given in Table 3.5. A 2024T3 aluminum plate with thickness of 2.003 mm and

five EN AW-1050A aluminum plates with different thicknesses from 0.5 mm to 4 mm, have been considered in this study.

Table 3.5: Characteristics of the considered case studies [39].

Metal alloy	**Nominal thickness (Δ) [mm]**	**Electrical conductivity (σ) [MS/m]**	**Plate dimensions [cm x cm]**
EN AW-1050A (Metallog)	0.469	35.4	13 x 18
	1.035	35.3	25 x 25
	1.969	35.0	25 x 50
	2.912	35.3	25 x 25
	3.994	34.5	25 x 25
2024T3 (Casoni)	2.003	18.8	20 x 20

3.7 Experimental results achieved with the proposed optimizations

In this Section, the experimental results achieved by using the proposed optimizations are presented and discussed. In particular, the subsection 3.7.1 is devoted to the description of the experimental results by using the iterative and the analytical algorithms while in subsection 3.7.2 are described the results obtained by using the dual-stage strategy with all the proposed interpolation technique.

3.7.1 Experimental results achieved with the iterative and analytical algorithms

The experimental campaign was carried out using the measurement set-up, the sample plates and the frequency-swept excitation described in Section 3.6. The aim was to analyze the accuracy of the proposed algorithms based on the Fundamental Thickness Equation (3.18).

The experimental results were organised in terms of a comparison between the following strategies:

(a) estimating Δ assuming the a priori knowledge of $\alpha(\cdot)$, evaluated at Δ;

(b) estimating Δ through the approach of [32];

(c) estimating Δ through the iterative approach with $e = 15\ \mu m$;

(d) estimating Δ through the analytical approach with a second-degree polynomial (minimum degree necessary);

(e) estimating Δ through the analytical approach with a fourth-degree polynomial (which have furnished the lowest RMSE (see Table 3.3).

Approach (a) corresponds to a thought experiment, since it requires the knowledge of $\alpha(\cdot)$ at the unknown thickness value, which is not available in a practical setting. However, this approach provides the best accuracy that can be achieved. In fact, the errors are only due to the uncertainty of the experimental set-up and the accuracy in calculating $\alpha(\cdot)$. The value of Δ used in evaluating function $\alpha(\cdot)$ at the r.h.s. of (3.18) is that of the nominal thickness shown in Table 3.5.

Thickness estimation performance has been compared in terms of the Relative Thickness Error (RTE), defined as:

$$RTE = \frac{\Delta_e - \Delta_a}{\Delta_a} \cdot 100 \tag{3.44}$$

where Δ_a is the actual thickness of the sample and Δ_e is the estimated thickness. Table 3.6 summarizes the obtained experimental results for the configurations of Table 3.5.

As expected, the smallest RTEs were observed by adopting approach (a), with RTEs lower than 1% except for the sample with a thickness of 0.469 mm, for which an RTE of 1.35% was found. For the original approach of [32], based on equation (3.12), the RTE significantly worsened, rising to 14%. The smallest error (2.68%) is obtained for a thickness equal to 1 mm. The new approaches of Section 3.4, namely (c), (d) and (e), yield an excellent performance. Indeed, the RTEs are always lower than 2.5% and, in several cases, are comparable with the "ideal" values obtained by using the a priori knowledge of $\alpha(\cdot)$, i.e. the thought experiment.

Table 3.6: Comparison between the thicknesses obtained by using the true value of $\alpha(\Delta)$, the α_0 value referred to Δ_{REF} and the two proposed solutions [39].

Actual thickness [mm]	**(a) Solution via the thought experiment**		**(b) Solution via the approach of [32]**		**(c) Solution via the iterative method**		**(d) Solution via the analytical method (second-degree)**		**(e) Solution via the analytical method (fourth-degree)**	
	Estimated thickness [mm]	RTE [%]	Estimated thickness [mm]	RTE [%]	Estimated thickness [mm]	RTE [%]	Estimated thickness [mm]	RTE [%]	Estimated thickness [mm]	RTE [%]
0.469	0.463	1.35	0.453	3.50	0.463	1.35	0.465	0.85	0.463	1.35
1.035	1.041	0.61	1.007	2.68	1.047	1.16	1.046	1.13	1.047	1.16
1.969	1.952	0.86	1.813	7.91	1.949	1.02	1.937	1.60	1.948	1.06
2.003	2.006	0.16	1.863	6.97	2.007	0.19	1.995	0.38	2.007	0.19
2.912	2.901	0.38	2.588	11.12	2.899	0.43	2.886	0.89	2.902	0.36
3.994	4.001	0.18	3.416	14.48	4.073	1.96	4.091	2.43	4.084	2.24

3.7.2 Experimental results achieved with the dual-stage strategy

In this section, the experimental results achieved by using the proposed dual-stage strategy are presented and discussed. Also in this case, the experimental campaign was made using the measurement station and the samples described in Section 3.6.

Table 3.7: Experimental performance achieved by using the 19-tone multi-sine signal (first-stage) [40]

	FOIP			FOCIP		
Actual thickness [mm]	Estimated thickness [mm]	RTE_M [%]	SD_{RTE} [%]	Estimated thickness [mm]	RTE_M [%]	SD_{RTE} [%]
0.469	0.487	3.84	0.04	0.486	3.67	0.03
1.035	0.871	-15.84	0.09	0.805	-22.18	0.05
1.969	1.395	-29.14	0.28	1.106	-43.82	0.13
2.003	1.666	-16.71	0.15	1.544	-22.79	0.10
2.912	3.479	19.49	3.75	1.813	-37.74	1.07
3.994	8.819	120.82	0	8.819	120.82	0
	MAIP			PCHIP		
Actual thickness [mm]	Estimated thickness [mm]	RTE_M [%]	SD_{RTE} [%]	Estimated thickness [mm]	RTE_M [%]	SD_{RTE} [%]
0.469	0.527	12.43	0.05	0.526	12.17	0
1.035	1.097	5.95	0.04	1.077	4.01	0
1.969	2.043	3.76	0.52	1.991	1.12	0.57
2.003	2.118	5.74	0.05	2.094	4.53	0
2.912	2.995	2.84	1.27	2.892	-0.68	1.26
3.994	3.923	-1.77	1.45	3.921	-1.83	1.47

Table 3.8: Experimental performance achieved by using the 11-tone multi-sine signal (second-stage) [40]

	FOIP			FOCIP		
Actual thickness [mm]	Estimated thickness [mm]	RTE_M [%]	SD_{RTE} [%]	Estimated thickness [mm]	RTE_M [%]	SD_{RTE} [%]
0.469	0.479	2.22	0.13	0.461	-1.62	0.13
1.035	1.068	3.19	0.12	1.063	2.70	0.12
1.969	1.993	1.23	0.22	1.977	0.42	0.21
2.003	2.045	2.08	0.12	2.036	1.63	0.11
2.912	2.868	-1.52	0.06	2.901	-0.39	0.09
3.994	4.009	0.37	0.57	3.923	-1.77	0.74
	MAIP			PCHIP		
Actual thickness [mm]	Estimated thickness [mm]	RTE_M [%]	SD_{RTE} [%]	Estimated thickness [mm]	RTE_M [%]	SD_{RTE} [%]
0.469	0.461	-1.62	0.56	0.460	-1.92	0.12
1.035	1.069	3.28	0.38	1.073	3.68	0
1.969	2.008	1.97	0.36	2.007	1.94	0.61
2.003	2.054	2.69	0.12	2.087	4.33	0
2.912	2.884	-0.96	0.14	2.884	-0.96	0
3.994	4.098	2.61	0.74	4.160	4.16	1.14

From the numerical results obtained in [40], it was possible to state that MAIP and PCHIP techniques performed better than FOIP and FOCIP techniques in the case of the first-stage. On the other hand, FOIP and FOCIP techniques performed better than MAIP and PCHIP techniques in the second-stage. This results was confirmed in optimal numerical case and in the simulation with measurement noise [40].

For this reason, MAIP and PCHIP techniques were applied at the first-stage, while FOIP and FOCIP were applied at the second-stage. Each test was repeated 100 times and both the mean relative error value (RTE_M) and the standard deviation of the relative error (SD_{RTE}) were evaluated. Experimental results for the first and second stage are shown in Tables 3.7 and 3.8 by using all the interpolating techniques, respectively. The results confirm performances predicted on numerical data with noise presented in [40].

From Table 3.7 it follows that MAIP and PCHIP have similar performances in

Table 3.9: Measurement time perfomance of the proposed dual-stage strategy [40]

Generation and acquisition – first stage	1.41 s
Elaboration – first stage	0.06 s
Generation and acquisition – second stage	1.14 s
Elaboration – second stage	0.05 s
Total Time	2.66 s

terms of both the RTEM and the SDRTE. Then, the peak frequency estimated by using MAIP, was used as center frequency for the second stage. Similar results can be achieved by means of PCHIP. From Table 3.8 it follows that FOIP and FOCIP have similar performances at the second stage. More precisely, FOCIP interpolating polynomials appears to show slightly better performances with maximum RTE lower than 2.7 %, and a maximum standard deviation of 0.7 %.

Eventually, an analysis of the measurement time is showed in Table 3.9. The time required to each elementary phase is evaluated: generation, acquisition and processing time for both the first and the second stages. It worth noting that the measurement of $\dot{Z}_{m,air}(f)$ can be carried out once for all, before the signal generation and/or acquisition. From the measurement time showed in Table 3.9, it follows that the proposed method requires up to 2.66 s, when using the double stage approach.

Moreover, the accuracy obtained by applying the proposed method, after the second measurement stage, are in line with both the requirements of the quality standard [84] and the results shown in [32]. These results have been achieved for treating automatically a "large" range of thicknesses of interest (from 0.4 mm to 4 mm, about), where the double stage procedure is mandatory to get a proper accuracy. In these conditions (large thicknesses range, two stage procedure), the proposed method requires less than 2.7 s, suitable for the on line test during typical production processes. When the nominal thickness value is given, then only the second stage can be applied. This requires a measurement time lower than 1.2 s.

3.8 Final considerations

This chapter was involved to present some novelties and optimizations applied for the thickness estimation of metallic plates. The methods are specifically designed for accurate, inline and real-time applications.

Firstly, it was explained the theory underlying the proposed method for the transfer characteristic, i.e. the relationship between the measured quantity ω_{min} and the unknown thickness Δ, for arbitrary thicknesses $0 < \Delta < +\infty$.

The complete knowledge of the transfer characteristic made it possible to find the physical limit of the probe, namely the critical thickness Δ_c: the measurement of any thickness smaller than Δ_c can be carried out safely, i.e. the solution of the Fundamental Thickness Equation (3.18) exists, is unique and depends continuously upon the data.

Complementary to the theory, this optimizations consists of two algorithms for estimating the unknown thickness. The first algorithm is based on an iterative method for which a proof of its convergence has been provided. The second algorithm is an analytical method, where the thickness is found as the solution of an algebraic equation, and is based on a local (polynomial) approximation of function $\alpha(\cdot)$. From a general perspective, the iterative algorithm may be preferred for applications where the probe is used on the full range, from 0 to the critical thickness Δ_c, whereas the analytical algorithm may be preferred when the target thicknesses vary in a local neighborhood where the polynomial approximation can be made accurate with only a few terms.

The experimental results confirmed the accuracy of the proposed approaches, with relative errors lower than 2.5%, and comparable with the ideal ones, that can be obtained in a thought experiment exploiting the knowledge of the unknown thickness.

Secondly, the proposed optimization allows to improve the performance in terms of measurement time: with the dual stage strategy, the first one can treat thickness in a wider range. In particular, the first-stage provides a coarse estimate of the thickness, whereas the second one provides its accurate estimate. Interpolating polynomial and multi-frequency signals played a relevant role in reducing the overall measurement time.

These activities (described in detail in [38–40]) led to the realization of a measurement system that could be applied in an industrial environment thanks to the good accuracy and low measurement times. The applicability of the method led to the realisation of an Italian patent and subsequently to the extension of a European patent. Currently, the application status is patent pending [41].

Chapter 4

Introduction of dimensional analysis in Nondestructive Testing and Evaluation

4.1 Theoretical framework and rationale behind the study

Problems related to Non–Destructive Testing and Evaluation (NDT&E) generally involve several variables. As a matter of fact, the outcome of a NDT&E test depends on *(i)* the parameters describing the probe (geometry, size, shape, materials, ...), *(ii)* the physical and geometrical parameters of the sample under testing (electrical conductivity, magnetic permeability, thickness, ...) and *(iii)* the geometrical parameters describing the position of the probe with respect to the sample under testing (lift-off, tilt angle, ...). The number of variables involved and the correlated nature of these variables (e.g., excitation frequency and thickness estimation as shown in Chapter 3) make an NDT&E problem difficult to handle. To this purpose, a methodology that can systematically reduce the complexity of problems by reducing the number of variables involved plays a very important role. For example, this reduction of number of variables has a major impact when a physical problem is modelled either via a machine learning approach or via a numerical approach [42–44]. In both cases there is an exponential reduction of the number of required numerical simulations or the size of the training database.

To this aim, dimensional analysis is a mathematical technique for analyzing problems involving physical quantities [91]. Dimensional analysis can be used to

simplify complex equations by highlighting the fundamental quantities that describe a problem. In particular, by analyzing only the physical dimensions of the variables involved in an equation, it is possible to determine a smaller number of fundamental quantities that describe the original problem. This simplify the computation of the solution of the original problem [92]. Dimensional analysis is commonly used in physics, engineering and other sciences to derive equations and verify experimental results [49, 50, 93].

Within dimensional analysis, Buckingham's π theorem plays a important role. Buckingham's π theorem has its roots in the concept that the equations of physics cannot be affected by the choice of the units of the physical quantities [51]. It states that any physical law can be written in terms of dimensionless groups and provides a procedure for finding these dimensionless parameters, also called π groups. The key is that the number of π groups is smaller than the number of the original variables. For instance, if a physical problem is modelled by an equation of the type $g(q_1, \ldots, q_n) = 0$ and the physical dimensions of the q_is are expressed by a set of k fundamental dimensions, then the Buckingham's π theorem allows to cast the original physical problem as $G(\pi_1, \ldots, \pi_p) = 0$, where $p = n - k$ and $\pi_1, \ldots, \pi_p$ are the dimensionless group [52–54]. The Buckingham's π theorem brings a problem to its fundamental form through the π groups [50], reducing the quantities involved [94] and decreasing the mathematical complexity of the problem of interest.

In the scientific literature, there are many original applications where the Buckingham's π theorem has been applied. For example, in [94], dimensional analysis was applied to processing the biological cells by using microfluidic devices. In [95], methods were developed based on the use of Buckingham's π theorem for optimizing tests inside wind tunnels. In [49] using dimensionless groups, the authors studied the characteristics of different bearing parameters as the temperature varies. Furthermore, in [93] π groups were adopted for a most effective description of the characteristic parameters of the thermal balance for the energy demand evaluation of a high-performance non-residential building. The creation of a rapid impedance model for proton exchange membrane fuel cells using physical and geometric parameters was analyzed in [96]. It is suggested to define dimensionless groups according to Buckingham's π theorem so that the relationships between the fundamental dimensions and the physical variables involved in the process under discussion can be adequately described. This strategy was helpful in solving issues where first-principles models are unknown, challenging to build, or impossible to compute. In [97] a comparative study on the wire electrical discharge machining of reinforcement materials was realized by means of Buckingham's π theorem. The theorem was used to model the input variables and thermophysical characteristics of wire electric discharge machining on the material removal rate and surface

roughness of aluminum and steel.

Without loss of generality, the Buckingham's π theorem appears to have the potential to simplify problems related to the large number of variables usually present in NDT&E problems. In this context, for the first time in the history of the NDT&E world, the application of this theorem was proposed to solve problems of various natures.

Specifically, the research activity focused on an initial application of this theorem on the main NDT&E methods like ultrasonic methods and EC methods. For the first case, the potential of the application of dimensional analysis in the case study of the simultaneous estimation of coating thickness and longitudinal transmission velocity was shown analytically. Appendix A shows the analytical procedures of the application of Buckingham's π theorem and shows how the analyzed variables are reduced from a number of ten dimensional variables to a number of six dimensionless variables.

For the second case, an intensive analysis was carried out. The simultaneous estimation of thickness and electrical conductivity of metallic materials was studied and analyzed. The effects of the dimensional analysis are shown in Section 4.3 where the results obtained analytically, numerically and experimentally were in-depth analyzed.

This activity (described in detail in [52–54]) also led to the realization of a measurement system that can be applied in an industrial environment due to its good accuracy and low measurement times. The applicability of the method led to the deposit of an Italian patent, which is currently pending [55].

4.2 The Buckingham's π theorem

The dimensional analysis includes the set of all methods useful to reduce the complexity of a physical problem, before carrying out its quantitative analysis. Buckingham's π theorem (1914) is a fundamental "tool" to achieve this result [51]. Its root lies in previous publications by Lord Rayleigh (1877), J. Bertrand (1878), A. Vaschy (1892) and D. Riabouchinsky (1911). In its essence, Buckingham's π theorem states that any physical law can be expressed in terms of dimensionless parameters, called "π groups" , since physical laws are independent from the system of units.

Buckingham's π theorem is stated as follows. Let a physical problem involving n dimensional scalar variables be modeled by a scalar equation of the type:

$$g\left(q_1, q_2, q_3, \ldots, q_n\right) = 0. \tag{4.1}$$

Let the physical dimensions of all variables expressed in term of a set of k fundamental dimensions $D_1, \ldots, D_k$:

$$\dim q_i = D_1^{a_{i1}} \times \ldots \times D_k^{a_{ik}},\ i = 1, \ldots, n, \tag{4.2}$$

then there exist $p = n - k$ dimensionless groups π_1, π_2, ... , π_p such that (4.1) can be cast in the form

$$G\left(\pi_1, \pi_2, \pi_3, \ldots, \pi_p\right) = 0. \tag{4.3}$$

This theorem extends trivially to other cases where the laws of physics are described by vectors (tensors) quantities and/or multiple equations.

The Buckingham's π theorem does not give the explicit expression for G, given g, but, rather, has to be derived explicitly, after the π groups have been computed.

An example of physical dimensions are those from the SI base units: T (time), L (length), M (mass), I (electric current), Θ (absolute temperature), N (amount of substance) and J (luminous intensity). However, any set of fundamental dimensions can be used in the Buckingham theorem.

The Buckingham's π theorem for the special case when there is one dependent variable, i.e. $q_1 = f\left(q_2, \ldots, q_n\right)$ gives

$$\pi_1 = F\left(\pi_2, \ldots, \pi_p\right). \tag{4.4}$$

The Buckingham's π theorem extent similarly for the case of two or more dependent variables.

From a general perspective, each π group can be expressed as

$$\pi_i = q_1^{\alpha_{i1}} \cdots q_j^{\alpha_{ij}} \cdots q_n^{\alpha_{in}} \tag{4.5}$$

where the exponents α_{ij}, $j = 1, 2, \ldots, n$, are rational numbers such that π_i is a dimensionless quantity.

To find the α_{ij}s, a set of k so called "repeating variables" chosen among the n dimensional quantities $q_1, \ldots, q_n$, has to be defined. The repeating variables must satisfy the following constraints: *(i)* their products, with proper exponents, give all the physical dimensions of the underlying problem; *(ii)* are independent; *(iii)* their arbitrary nontrivial products do not generate a dimensionless quantity; *(iv)* they should not be dependent variables of the problem, if any. Assuming the k repeating variables are $q_1, \ldots, q_k$, each π group is expressed as

$$\pi_i = q_1^{\alpha_{i1}} \times \ldots \times q_1^{\alpha_{ik}}\, q_{k+i},\ i = 1, \ldots, n-k, \tag{4.6}$$

and coefficients α_{ij}s are found by imposing each π group to be dimensionless.

The main advantage of the Buckingham's π theorem consists in the reduction of the number of relevant variables describing a problem from n to p, being $p = n - k$.

This approach is very effective especially when n is of the order of few units. This is because k is of the order of few units, $k \leq 7$ in the SI, thus making p a fraction of n when n is of the order of few units. For instance, in analyzing the RLC circuit, the problem has $n = 6$ and $k = 3$, thus yielding $p = 3$, that is one-half of n. This has a major impact in reducing the amount of experimental and/or numerical data required to make correlations of physical variables.

Indeed, for fully characterizing the function f appearing in [52] for the RLC circuit example, the parameters array $\left(\bar{E}, \omega, R, L, C\right)$ has to be varied in $\mathbb{C} \times \mathbb{R}^4$, whereas the full characterization of the function F in [52] requires the parameters array (π_2, π_3) to be varied in $\mathbb{R}^2$. This latter option (evaluation of F) is definitely less expensive, in terms of number of experimental test or numerical simulation, if compared to the first one (evaluation of f). Summing up, dimensional analysis is a very powerful technique for formulating physics problems in their most basic forms, by minimizing the degrees of freedom of the problem.

Another advantage offered by Buckingham's π theorem is that its application does not require the a priori knowledge of the law relating the key physical quantities. It can be applied starting from only the knowledge of the physical variables describing the phenomenon. This is very important when the laws constraining the physical quantities are unknown, and it provides a guide for finding such laws.

4.3 Buckingham's π theorem in an EC case study: simultaneous estimation of thickness and electrical conductivity of metallic samples.

In this Section, a new methodology to simultaneously estimate the thickness and the electrical conductivity of metallic samples is discussed. The proposed approach is based on the application of the EC method combined with the Buckingham's π theorem [51].

This specific applications is motivated by recognizing that the measurement of the value thickness and electrical conductivity of metallic materials is a crucial factor in all production and manufacturing processes (e.g., heat treatment, rolling and pressing). Indeed, these two quantities directly affect the quality properties of finished products, such as hardness, toughness, and tensile strength [10, 11, 13, 84]. Additionally, many methods in the literature relating to thickness measurement require a priori knowledge of the electrical conductivity of the analysed sample, which is not always available [32, 33]. In this scenario, accurate, real-time monitoring of the thickness and electrical conductivity of metallic materials is essential to improve production quality and efficiency. In-line measurement techniques are

essential because they enable automatic quality control during production, ensuring products or materials with appropriate accuracies, reasonable prices and reduced measurement times.

The possibility of applying EC methods to the simultaneous estimation of several parameters, such as thickness, electrical conductivity and lift-off, has been widely studied in the literature. For example, in [98] was proposed a method to simultaneously measure the thickness and electrical conductivity of the metallic sample, based on a single-frequency ECT method analyzing the phase of the mutual impedance. ECT sensing systems using anisotropic magnetoresistive sensors for simultaneous estimation of thickness and electrical conductivity was proposed in [99], while in [100] a new eddy current sensing method with a material-independent model for coupled-parameter estimation was proposed. Pulsed Eddy Current methods were also analyzed for multi-parametric estimation. For instance, in [101] the possibility to determine the thickness and electrical conductivity of conductive coatings on metallic samples was investigated using a PEC method, while in [102] a transient eddy-current measurement approach was proposed. Finally, an improved Newton iterative method to detect thickness, electrical conductivity, permeability, and lift-off of the metallic sample based on multi-frequency excitation ECT was developed in [103].

In this activity, the Buckingham's π theorem were applied in order to simultaneously estimate the thickness and electrical conductivity of metallic samples. With respect to the methods already found in the literature, the methodology proposed in this work offers certain advantages. Firstly, Buckingham's theorem makes it possible to reduce the number of variables to be considered, which reduces the computational complexity of the problem. Secondly, it allows the structure of the relationships existing between the variables involved to be established. Thirdly, the proposed procedure is compatible with applications in which simultaneous estimation is required in on-line and real-time industrial conditions. Fourthly, the proposed approach guarantees excellent accuracy.

The Section is organized as follows. In subsection 4.3.1 it was applied the Buckingham's π theorem to the specific problem and it was derived the essential structure of the relationship between the relevant variables in terms of π groups [52–54]. In subsection 4.3.2, it was provided the method for the simultaneous estimation of the thickness and electrical conductivity of a nonmagnetic sample. Subsection 4.3.5 and subsection 4.3.6 contains descriptions of the experimental set–up, case studies and experimental results respectively. Finally, in Section 4.5 is described an initial metrological characterization with respect of the single thickness estimation.

4.3.1 Dimensional analysis in Eddy Current method

An Eddy Current Probe (ECP) is usually made by an excitation coil, that generates a time-varying magnetic flux density inducing, in turn, a current density in a metallic material, and a receiver coil or field sensor to sense the reaction magnetic flux density due to the induced eddy currents as described in Chapter 2. Probes of different shape and arrangement can be adopted, which are based on a single or multiple coils for producing the excitation magnetic field and for measuring the response of the material under testing [98, 101–103], one coil for the excitation magnetic field and a magnetic flux density sensor for the sensing the response [99, 100], and so on. In all these EC scenarios, Buckingham's π theorem can be suitably applied for a deep understanding of the structure of the relationships between the variables describing the physical problem and for getting a simplification of the model thanks to the reduction of the number of degrees of freedom required to describe the system.

To shown the effectiveness of the Buckingham's π theorem for the simultaneous evaluation of thickness and conductivity via EC data, a specific case study was considered. Without loss of generality, it has been considered an ECP made of two coaxial coils (transmitter and receiver): the upper coil used as driving coil and the lower coil as pick-up coil. Coaxial coils and nonmagnetic materials have been assumed. Fig 4.1 shows the geometry of the problem, with both the metallic sample and the ECP.

In the case of interest, the measured quantity is $\Delta\dot{Z}_m = \dot{Z}_{m,sample} - \dot{Z}_{m,air}$, i.e. is the difference of the mutual impedance between the coils when the ECP is located on the sample ($\dot{Z}_{m,sample}$) and in air ($\dot{Z}_{m,air}$), respectively, at a prescribed angular frequency. Hereafter coaxial coils and nonmagnetic materials are defined. The key physical quantities determining $\Delta\dot{Z}_m(\omega)$ are (see Fig. 4.1):

- the parameters describing the geometry of the probe: the internal r_1 and external r_2 radii of the coils, the height h_1 and number of turns N_1 of the receiving coil, the height h_2 and number of turns N_2 of the driving coil and the separation between the coils d;
- the angular frequency ω of the driving current applied for the test;
- the thickness Δh and the electrical conductivity σ of the metallic sample;
- the magnetic permeability of the vacuum μ_0 and the corresponding magnetic reluctance $\nu_0 = 1/\mu_0$.
- the lift-off l_0 between the sample and the ECP and the tilting of the ECP probe w.r.t. the perpendicular to the sample.

The geometrical parameters of the ECP are normalized with respect to a length $D = r_2$ and are grouped in a dimensionless vector $\mathbf{t} = (r_1/D, h_1/D, h_2/D, d/D)$. The normalization constant D represents the size of the probe. Other choices for D can be equally made.

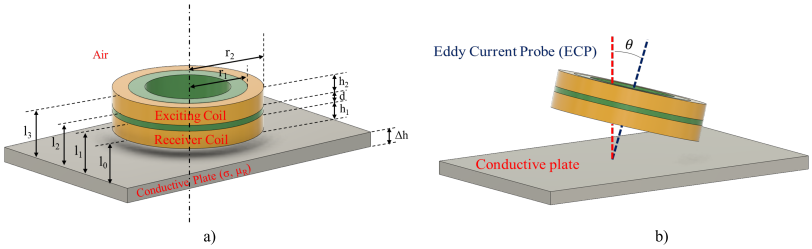

Figure 4.1: Representation of the axis-symmetrical ECP placed on the metallic sample with their geometrical characteristics [52].

All the listed parameters (geometry of the probe, number of turns of the coils, conductivity and thickness of the sample, lift-off and tilting of the ECP with respect to the sample) affect the mutual impedance between the transmitting and receiving coils, i.e.

$$\frac{\Delta \dot{Z}_m}{N_1 N_2} = f\left(\omega, \sigma, \nu_0, \Delta h, D, \mathbf{t}, l_0, \theta\right). \tag{4.7}$$

The evaluation of f, either by a numerical method or an experimental campaign, is not a trivial task, because its cost/time increases exponentially with the number of the arguments.

Equation (4.7) involves a total of nine variables ($n = 9$), with seven real-valued and scalar independent variables $\omega, \sigma, \Delta h, D, l_0, \theta, \nu_0$, one real-valued vector independent variable $\mathbf{t}$ and one complex-valued dependent variable $\Delta \dot{Z}_m/N_1 N_2$. Variables D and $\mathbf{t}$ correspond to five real-valued and scalar variables (r_1, r_2, h_1, h_2, d). All variables can be expressed in terms of three fundamental dimensions ($k = 3$), length L, time T and impedance Ω, as showed in Table 4.1.

Buckingham's π theorem allows to obtain six dimensionless groups ($p = n - k = 6$) as those listed in Table 4.2, where it has been assumed ν_0, ω and D as repeating variables. It is worth noting that each dimensionless variable of the original problem, as $\mathbf{t}$ and θ, is assigned to a dimensionless π group, i.e. $\pi_5 = \mathbf{t}$ and $\pi_6 = \theta$. Consequently, (4.7) can be expressed as $\pi_1 = F\left(\pi_2, \pi_3, \pi_4, \pi_5, \pi_6\right)$, that is

Table 4.1: Dimensional variables in the multi-parameter estimation problem, expressed in terms of fundamental dimensions [52].

Numbers	Parameters	Symbols	Fundamental dimensions
1	impedance variation	$\Delta\dot{Z}_m$	$[L^0T^0\Omega^1]$
2	electric conductivity	σ	$[L^{-1}T^0\Omega^{-1}]$
3	magnetic reluctance of the vacuum	ν_0	$[L^1T^{-1}\Omega^{-1}]$
4	angular frequency	ω	$[L^0T^{-1}\Omega^0]$
5	thickness	Δh	$[L^1T^0\Omega^0]$
6	lift-off	l_0	$[L^1T^0\Omega^0]$
7	ECP characteristic length	D	$[L^1T^0\Omega^0]$
8	ECP shape	$\mathbf{t}$	$[L^0T^0\Omega^0]$
9	probe orientation features	θ	$[L^0T^0\Omega^0]$

$$\frac{\Delta\dot{Z}_m\nu_0}{N_1N_2\omega D} = F\left(D\sqrt{\frac{\omega\sigma}{2\nu_0}}, \frac{\Delta h}{D}, \frac{l_0}{D}, \mathbf{t}, \theta\right) \tag{4.8}$$

$$= F\left(\frac{D}{\delta}, \frac{\Delta h}{D}, \frac{l_0}{D}, \mathbf{t}, \theta\right), \tag{4.9}$$

where F is a proper function and the skin-depth δ is equal to

$$\delta = \sqrt{\frac{2\nu_0}{\omega\sigma}}. \tag{4.10}$$

Table 4.2: List of the π groups for the case of interest [52–54]

Dimensionless groups		
$\bar{\pi}_1 = \frac{\Delta\dot{Z}_m\nu_0}{N_1N_2\omega D}$	$\pi_2 = D\sqrt{\frac{\omega\sigma}{2\nu_0}}$	$\pi_3 = \frac{\Delta h}{D}$
$\pi_4 = \frac{l_0}{D}$	$\pi_5 = \mathbf{t}$	$\pi_6 = \theta$

By taking into account that the purpose of this study is to measuring the thickness and the electrical conductivity of a metallic sample, given the characteristics $\mathbf{t}$ of the ECP and the lift-off l_0 and tilting θ, it is convenient to focus on groups $\bar{\pi}_1$, π_2 and π_3 since π_4, π_5 and π_6 are known. Consequently, the final dimensionless relationship under analysis is:

$$\frac{\Delta\dot{Z}_m\nu_0}{N_1N_2\omega D} = F\left(D\sqrt{\frac{\omega\sigma}{2\nu_0}}, \frac{\Delta h}{D}\right), \tag{4.11}$$

where, with a slight abuse of notations, the values of π_4, π_5 and π_6 are understood. Equation (4.11) has to be compared with the counterpart of (4.7) for prescribed (understood) $\mathbf{t}$, l_0 and θ:

$$\frac{\Delta \dot{Z}_m}{N_1 N_2} = f\left(\omega, \sigma, \nu_0, \Delta h, D\right). \tag{4.12}$$

The impact of the Buckingham's π Theorem is significant. Firstly, starting from (4.12) involving a complex function of five real arguments, it is possible to get an equivalent relationship requiring a complex function F of two real arguments, without the explicit knowledge of the original function f. The new (reduced) function F can be easily computed numerically of measured experimentally, since it is defined in $\mathbb{R}^2$ rather than in $\mathbb{R}^5$. Moreover, by combining (4.11), with the π groups of Table 4.2, it is easy to realize that f and F are tightly related:

$$f\left(\omega, \sigma, \nu_0, \Delta h, D\right) = \frac{\omega D}{\nu_0} F\left(D\sqrt{\frac{\omega\sigma}{2\nu_0}}, \frac{\Delta h}{D}\right), \tag{4.13}$$

thus the computation or experimental evaluation of F gives the values of f.

Secondly, the Buckingham's π Theorem allows to represent the inverse problem in the two-dimensional (π_2, π_3) plane, rather than in a five-dimensional space. This last remark is at the foundation of the method for the simultaneous estimate of Δ and σ via level curves, described in subsection 4.3.2.

It is important to remark that the same approach can be applied to the case of a single coil ECP or to the case when the reaction magnetic flux density is measured by a field sensor.

4.3.2 Simultaneous estimate of thickness and electrical conductivity

This subsection is organized in two parts. In the first part an approach based on level curves is proposed. Level curves can be easily introduced, thank to the π groups, that play a key role. The second part is devoted to show the physical limits of the method in terms of level curves.

Without loss of generality, a planar geometry has been considered for demonstrating the effectiveness of dimensional analysis. The same treatment can be applied to non-planar geometries like tubes and complex shapes.

Thanks to the abstract representation of (4.11), where the (complex) measured quantity $\bar{\pi}_1$ is a function defined in the (π_2, π_3) plane, it is possible to introduce a set of level curves with respect to $\bar{\pi}_1$. This is possible because the measured quantity $\dot{Z}_m$ and the unknowns σ and Δh are not mixing in the π groups.

To get a level curve in the (π_2, π_3) plane, it is required to prescribe the value of a real valued quantity. For instance, it is possible to chose either the real part, or the imaginary part, or the magnitude, or the phase of $\bar{\pi}_1$, or any other real function of $\bar{\pi}_1$. Fig. 4.2 shows the level curves for the four basic quantities: $\mathrm{Re}\{\bar{\pi}_1\}$, $\mathrm{Im}\{\bar{\pi}_1\}$, $|\bar{\pi}_1|$ and $\angle\bar{\pi}_1$, in the (π_2, π_3) plane. The parameters for the underlying ECP are provided in Table 4.3.

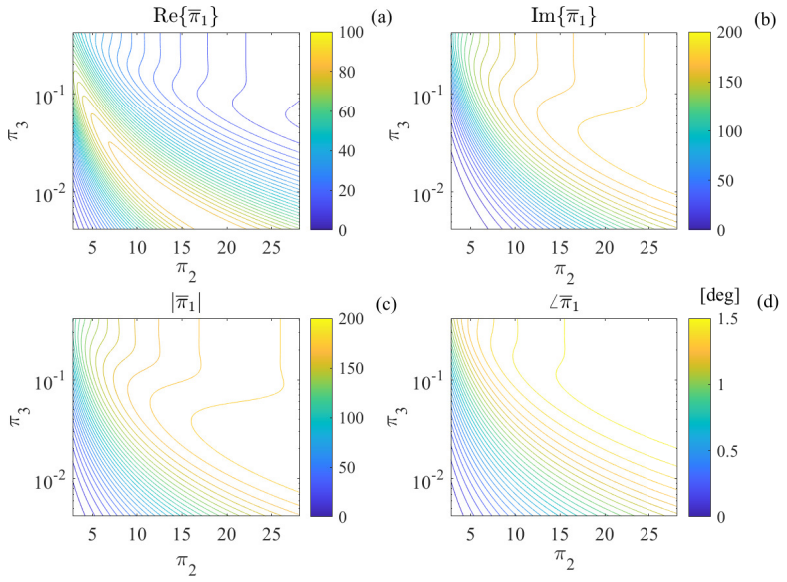

Figure 4.2: Level curves for $\bar{\pi}_1$: (a) $\mathrm{Re}\{\bar{\pi}_1\}$, (b) $\mathrm{Im}\{\bar{\pi}_1\}$, (c) $|\bar{\pi}_1|$, and (d) $\angle\bar{\pi}_1$. The level curves have been plotted at constant step, i.e. the difference between the values for two consecutive level curves is constant. Smaller gradients are found where the distance between the curves increases [52].

The level curves of Fig. 4.2 have been obtained from a numerical evaluation of $F(\pi_2, \pi_3)$ in a range of values for π_2 and π_3. The numerical evaluation has been carried out by evaluating $\Delta\dot{Z}_m$ via the the semi-analytic model by Dodd and Deeds [83]. π_2 has been varied in the range $[2.82;\ 28.2]$, whereas π_3 in the range $\left[4.2 \times 10^{-3};\ 42 \times 10^{-3}\right]$. These ranges have been obtained by retaining σ constant and varying Δh and ω, as in Table 4.4.

The level curves are a powerful tool to solve equation

$$F(\pi_2, \pi_3) = \bar{\pi}_1. \tag{4.14}$$

Specifically, from the measurement of $\dot{Z}_m$ at a prescribed angular frequency ω, it

Table 4.3: Values of the parameters of the ECP [52].

Parameter	Value
$h_1 = h_2$	6 [mm]
d	2.20 [mm]
r_1	23.60 [mm]
r_2	23.95 [mm]
l_0	1 [mm]
$N_1 = N_2$	17
θ	0 [°]

Table 4.4: The physical parameters used for the numerical evaluation of $F(\cdot, \cdot)$ [52].

Parameters	Value
σ	35 MS/m
Δh	[0.1 mm, 10 mm]
f	[100 Hz, 10000 Hz]

is possible to compute $\bar{\pi}_1$ as $\Delta\dot{Z}_m\nu_0/N_1N_2\omega D$. Then, from the specific value of $\bar{\pi}_1$, it is possible to solve (4.14) by finding the intersection point between the level curves from two or more different plots of Fig. 4.2, as shown in Fig. 4.3. Once π_2 and π_3 have been evaluated, the unknown electrical conductivity σ and thickness Δh can be evaluated as

$$\sigma = \frac{2\nu_0}{\omega}\left(\frac{\pi_2}{D}\right)^2 \tag{4.15}$$

$$\Delta h = D\pi_3. \tag{4.16}$$

The step-by-step algorithm is:

- Measure $\Delta\dot{Z}_m$ at a prescribed ω;
- compute $\bar{\pi}_1 = \Delta\dot{Z}_m\nu_0/N_1N_2\omega D$;
- find the level curves for at least two plots of Fig. 4.2;
- find the intersection point (π_2, π_3) for the selected level curves;
- compute σ and Δh via (4.15) and (4.16).

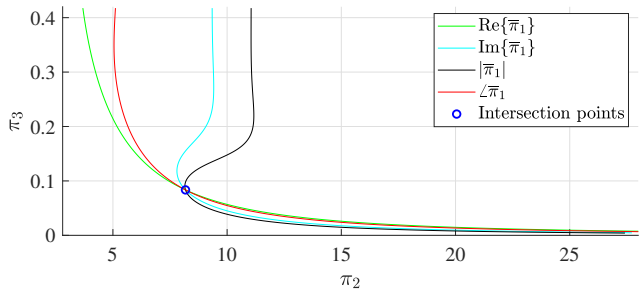

Figure 4.3: Intersection of level curves from the mutual impedance measured at an individual prescribed frequency. The sample has an electrical conductivity of 18 MS/m and a thickness of 2 mm. The frequency is 1650 Hz [52].

Summing up, dimensional analysis allows to cast the problem of retrieving Δh and σ in very simple terms as intersection of level curves in a plane. This is because the five primary parameters $(\omega, \sigma, \nu_0, \Delta h, D)$ influencing the measured data combine in the very compact form given by groups π_2 and π_3, rather than individually as in (4.12). For the same reason, i.e. that the influence parameters combine in a compact form, it is computationally feasible to compute numerically the function $F(\cdot, \cdot)$, that is a function of two parameters rather than $f(\cdot, \cdot, \cdot, \cdot, \cdot)$, that depends on five parameters. Finally, it is worth noting that the $F(\cdot, \cdot)$ can be pre-computed and stored once for all, given $\mathbf{t}$, l_0 and θ.

The noise is a major issue when dealing with experimental data. To increase the accuracy of the method, it is proper to process the impedance measured at multiple frequencies. In this case, the level curves intersection procedure has to be repeated at each angular frequency, thus obtaining a set of points in the (π_2, π_3) plane, as showed in Fig. 4.4.

Since π_2 is independent on ω, whereas π_3 depends on ω, being proportional to $\sqrt{\omega}$, the intersection points are distributed along a horizontal line. To each intersection point related to the impedance measured at the $i-$th angular frequency ω_i corresponds an estimate σ_i and Δh_i of the electrical conductivity and thickness of the sample. The final estimation of Δh and σ can be obtained by processing all the the Δh_is and σ_is at an improved robusteness since combines the information from different frequencies.

Alternatively, it is possible to plot the level curves on the $(\sigma, \Delta h)$ plane, by means of (4.15) and (4.16). This latter strategy is extremely convenient because *all* the level curves, regardless the angular frequency, intersect at the *same* point, as showed in Fig. 4.5. The intersection point gives directly the estimate of Δh and

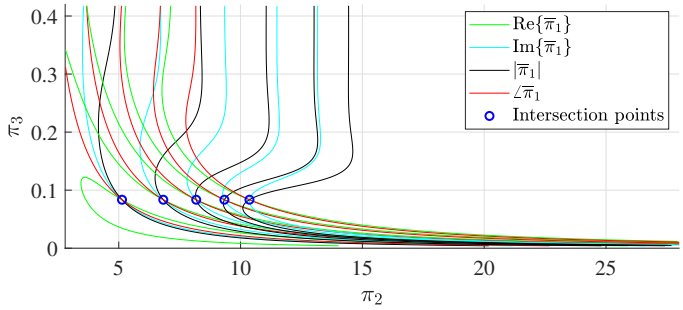

Figure 4.4: Intersection of level curves from the mutual impedance measured at five different frequencies. The sample has an electrical conductivity of 18 MS/m and a thickness of 2 mm. The frequencies are 650, 1150, 1650, 2150 and 2650 Hz [52].

σ.

The (π_2, π_3) plane can be divided in different regions, yielding to different information that be inferred from the measured data.

There are three basic conditions that have to be considered:

1. the skin-depth $\delta(\omega)$ is enough smaller than Δh. i.e. $\pi_2\pi_3$ is enough larger than 1;

2. the size of the probe D is much smaller than Δh, i.e. $\pi_3 \gg 1$;

3. the skin-depth $\delta(\omega)$ is much larger than Δh, i.e. $\pi_2\pi_3 \ll 1$ and the size of the probe D is much larger than Δh, i.e. $\pi_3 \ll 1$.

In the first case (regions (c), (f) and (i) of Fig. 4.7), the skin-depth is smaller than Δh and this prevents the thickness Δh to be retrieved from the data, i.e. the dimensionless impedance $\bar{\pi}_1$. This behaviour can be easily recognized in the plots of Fig. 4.2, where the level curves become almost vertical, meaning that the π_3 does not affect the measured data $\bar{\pi_1}$, i.e. Δh cannot be retrieved by the knowledge of $\bar{\pi_1}$. We found numerically that the region where the level curves are almost vertical corresponds to $\pi_2\pi_3 > 3$, as shown in Fig. 4.6. However, in these regions, the electrical conductivity can be still retrieved from $\bar{\pi}_1$, since a change in the electrical conductivity, i.e. in π_2, determines a change of $\bar{\pi}_1$.

In the second case (regions (a), (b) and (c) of Fig. 4.7), the probe is geometrically too small to interact with the bottom of the sample, regardless the skin-depth, i.e. regardless the value of $\pi_2 = D/\delta$. This prevents the thickness Δh to be re-

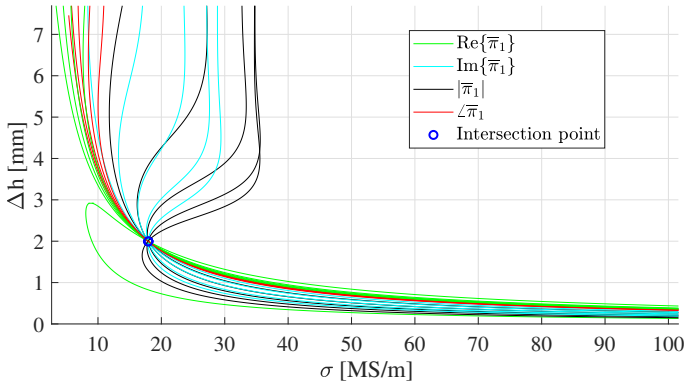

Figure 4.5: Representation on the normalized plane of the frequency measurements obtained in the case of sample with thickness of 2 mm and electrical conductivity of 18 MS/m for the level curves Re$\{\bar{\pi}_1\}$, Im$\{\bar{\pi}_1\}$, $|\bar{\pi}_1|$, and $\angle\bar{\pi}_1$ using five different excitation frequencies [52].

trieved from $\bar{\pi}_1$, but the electrical conductivity σ can be still retrieved. As for the previous case, the level curves are almost vertical in regions (a), (b) and (c).

In the third case (region (g) of Fig. 4.7), the probe is much larger than the thickness Δh and the sample is fully penetrated by the electromagnetic field. In this case is possible to retrieve only the surface electrical conductivity of the sample, i.e. the $\sigma\Delta h$ product [38].

In the remaining regions (d), (e) and (h) of Fig. 4.7, it is possible to retrieve both the electrical conductivity σ and the thickness Δh, starting from the dimensionless impedance $\bar{\pi}_1$. This is the so-called *feasibility* region, where the largest amount of information can be retrieved from the measured data. Region (h) deserves to be highlighted, because it opens to the possibility of measuring both the electrical conductivity and the thickness of thin and very thin samples.

The plots of the level curves provide another precious but less recognized information. Specifically, at the higher frequencies where the thicknesses cannot be retrieved (regions (c), (f) and (i) of Fig. 4.7), the spacing between the level curves increases, as showed in Fig. 4.2. This means that the gradient of the measured data $\bar{\pi}_1$ with respect to π_2 decreases for increasing π_2. In other terms, at large angular frequencies and/or electrical conductivities, the sensitivity of the measurement with respect to σ decreases, despite some authors claimed that it is convenient estimating the electrical conductivity in such conditions, because the data does not depend on the thickness Δh.

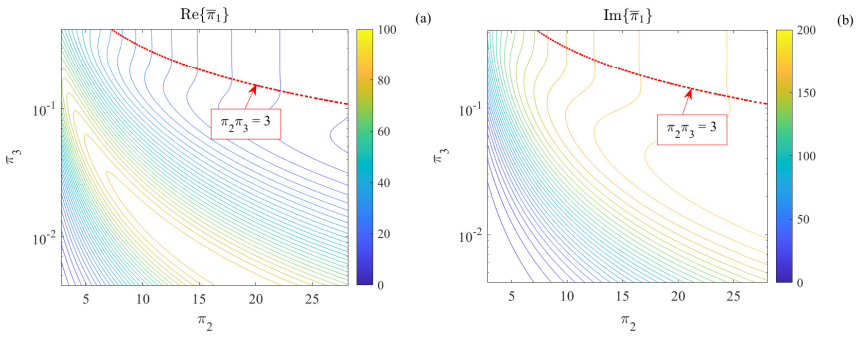

Figure 4.6: The level curves above the curve $\pi_2\pi_3 = 3$ are almost vertical [52].

4.3.3 A initial numerical validation of the proposed method

In this subsection, a preliminary application of the method in a numerical environment was carried out. Were considered three different samples, whose thickness and electrical conductivity are reported in Table 3.6, that are: common copper, aluminium for automotive application [104] and a different aluminium for aerospace applications [105].

The tests concern a simple single-coil sensor as shown in Figure 4.8. It was composed by a number of turns equal to 20, an external radius (R_{ext}) equal to 20 mm, an internal radius equal (R_{int}) to 19.60 mm, an height (H) equal to 3 mm and a lift-off (L_o) equal to 0.5 mm.

In order to observe the self-impedance trends, the analysis was carried out numerically by means of the Dodd and Deeds semi-analytical model [83]. The results of the model were also corrupted by synthetic noise. Specifically, let $\Delta\dot{Z}_n$ the noisy version of the simulated self-impedance, it was considered $\Delta\dot{Z}_n = \Delta\dot{Z} + N$, where N is the Gaussian Noise characterized by mean equal to 0 and standard deviation equal to σ_x. The application of the method on the various features of π_1 (related to self-impedance measured by the eddy current probe), the standard deviation σ_x is chosen starting from the typical accuracy values of LCR meters [106, 107].

Figure 4.9 shows the intersection points obtained through the features $\mathrm{Re}\{\bar{\pi}_1\}$, $\mathrm{Im}\{\bar{\pi}_1\}$, $|\bar{\pi}_1|$ and $\angle\bar{\pi}_1$ considering different noise levels equal to $0.1\%, 0.25\%$ and 1% (e.g. the best performances achievable by [106]) for fifty numerical tests. As it can be seen, as the noise level value increases, the intersection points tend to have greater variability. The effect of the noise levels considered is also shown in Figure 4.10. It can be seen that the intersection distribution in the scatter plot on normalized (Δh,σ) plane tends to cover a greater area as the measurement

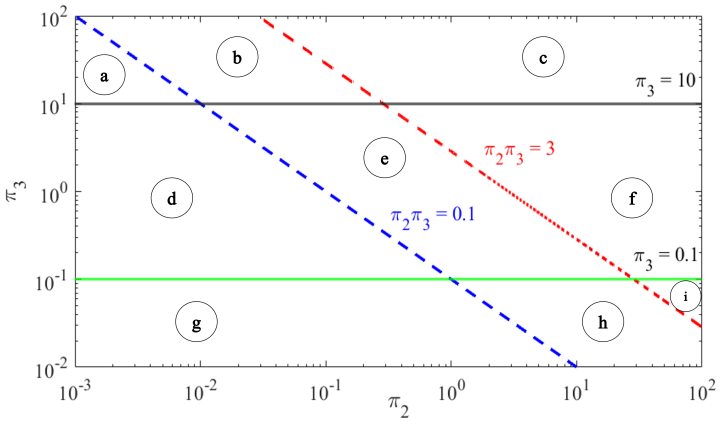

Figure 4.7: The different regions of operations. The basic constraints $\pi_3 \gg 1$, $\pi_2\pi_3 \ll 1$ and $\pi_3 \ll 1$ are represented as $\pi_3 \geq k$, $\pi_2\pi_3 \leq 1/k$ and $\pi_3 \leq 1/k$, being $k \gg 1$. Here $k = 10$ [52].

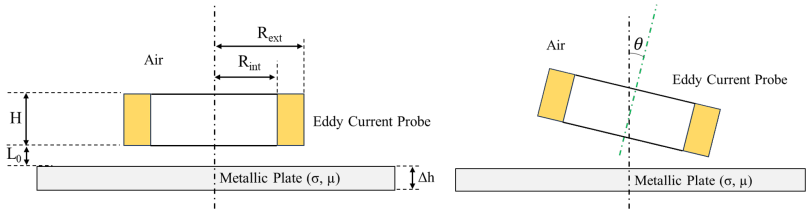

Figure 4.8: Eddy Current Probe placed on a conductive plate with its geometrical characteristics [53].

performance worsens.

In order to realize a quantitative analysis, in Table 4.5, the results of the application of the presented method in the different cases are reported. Specifically, the mean absolute relative error of the estimated quantity (ε_{mean}) and the estimated relative standard deviations on overall absolute relative errors ($std_{\varepsilon_{mean}}$) on a set of fifty numerical tests at $500, 1000, 1500, 2000, 2500$ Hz are reported.

As it can be seen, the method appears to be quite robust with respect to noise. Indeed, the values of ε_{mean} and $std_{\varepsilon_{mean}}$ are reasonably low even for increasing σ_x and compatible with the performance in terms of measurement time, in-line inspections related to the paradigm of the Industry 4.0.

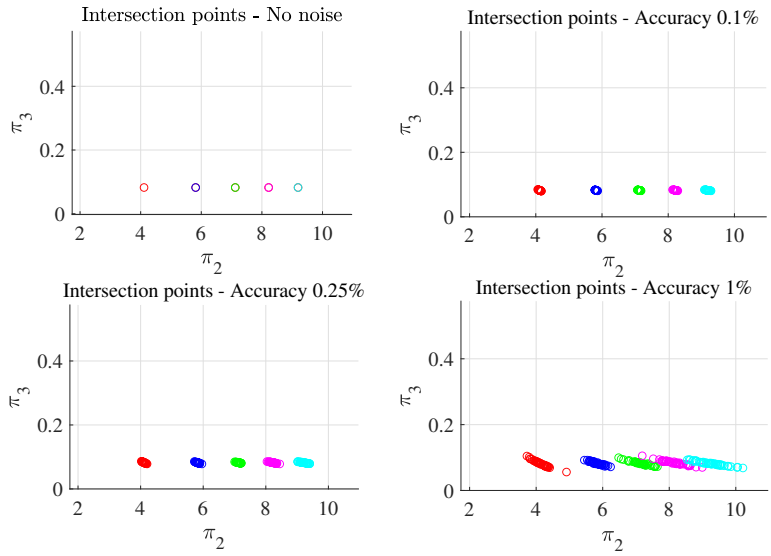

Figure 4.9: Intersection points obtained on π_2, π_3 plane considering a set of fifty numerical tests at 500(red), 1000(blue), 1500(green), 2000(magenta), 2500(cyan) Hz and different noise levels [53].

4.3.4 The measurement procedure

The measurement procedure consists of three main phases subdivided into elementary steps as sketched in Fig. 4.11 and shown in [52].

The first phase is carried out off-line, once the parameters of interest have been defined (e.g. the thickness and electrical conductivity ranges to be estimated, the probe characteristics and the frequency range to be analysed). It is characterised by three phases: parameter definition, numerical simulations and experimental calibration. This step is performed once and is only repeated if one of the defined characteristics (e.g. probe, frequency range, etc.) changes.

The second phase is made in-line and it is characterized by two main steps: the experimental execution of the test at a defined excitation frequency (fixed inside the frequency range defined in Phase 1); the processing of the measured quantities to estimate the thickness and electrical conductivity. With the aim to improve the quality of the thickness and electrical conductivity estimation, Phase 2 can be repeated for different values of the frequency.

Finally, in the third phase, the final estimation of the thickness and electrical conductivity is provided by means of the level curves of Fig. 4.4 or its equivalent

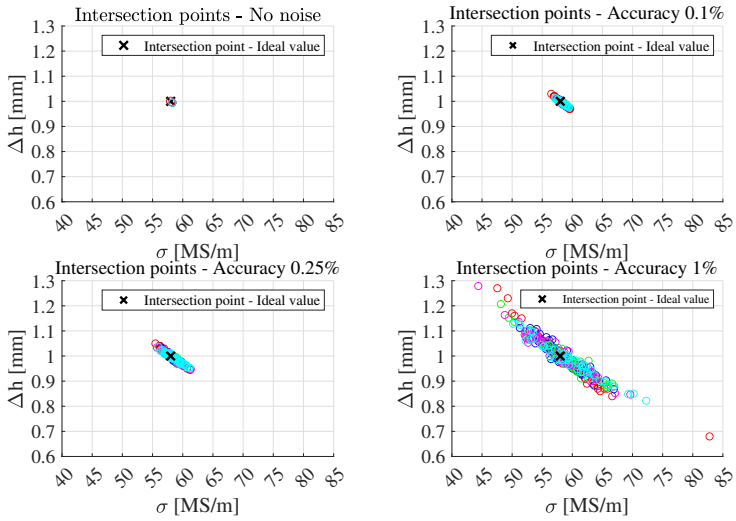

Figure 4.10: Intersection points obtained on σ, Δh plane considering a set of fifty numerical tests at 500(red), 1000(blue), 1500(green), 2000(magenta), 2500(cyan) Hz and different noise levels [53].

of Fig. 4.5, in case of measurement at multiple frequencies.

Details for each individual step are given below.

Phase 1: Off-line activities

1.1 *Parameters definition*

In this step, the characteristics of both the sample under test and the ECP are defined. In particular, the following parameters are prescribed: *(i)* geometry, dimensions and physical parameters of the ECP; *(ii)* thickness and electrical conductivity ranges to be explored; *(iii)* range of the excitation frequencies to be analysed.

The main parameters used in this paper are summarized in Tables 4.3 and 4.4.

1.2 *Numerical simulations*

This step consists in an off-line numerical simulation to evaluate the level curves, given the parameters defined in Step # 1.1. In detail, for each value of thickness and frequency, the corresponding simulated value of $\Delta\dot{Z}_m$ ($\Delta\dot{Z}_{m,sim}$) is obtained using the semi-analytic models developed by Dodd and

Table 4.5: Performance achieved with the considered noise levels.

Cases	Noise levels [%]	$\epsilon_{\Delta h,mean}$[%]	$std_{\epsilon_{\Delta h,mean}}$[%]	$\epsilon_{\sigma,mean}$[%]	$std_{\epsilon_{\sigma,mean}}$[%]
Δh =	0.10	0.49	0.10	0.46	0.11
1[mm], σ =	0.25	0.60	0.34	0.57	0.36
58[MS/m]	1	0.91	0.57	1.38	0.50
Δh =	0.10	0.17	0.05	0.12	0.04
3[mm], σ =	0.25	0.29	0.18	0.27	0.21
20[MS/m]	1	2.64	3.81	2.21	3.23
Δh =	0.10	0.13	0.31	0.06	0.14
5[mm], σ =	0.25	0.74	0.98	0.41	0.39
17[MS/m]	1	2.69	2.27	1.39	1.19

Deeds [83] (other simulation tools can be used without leading the generality of the proposal). Then, the resulting values of the dimensionless groups ($\bar{\pi}_1$, π_2, π_3) are calculated, according to the dimensionless groups listed in Table 4.2. In this phase, it is important to generate dimensionless curves for the higher number of different thicknesses and electrical conductivities. This means to make several simulations changing the thickness and the electrical conductivity (the product $\omega\sigma$) inside the ranges defined in Step # 1.1 with a suitable resolution step allowing to have one level curve for each thickness and $\omega\sigma$ product. In this phase, the desired resolution capability in the $\Delta h - \sigma$ estimation is defined. The time needed to do this task is not an issue since it is made once.

1.3 *Experimental calibration*

In order to use the level curves simulated in Step # 1.2 to estimate unknown thickness and electrical conductivity from experimental results, a suitable experimental calibration phase is needed. The aim is to check the agreement between the simulated and experimental data due to the adopted simulation model, the uncertainty in the knowledge of the geometrical and physical characteristics of the ECP, the experimental noise, the measurement uncertainty, and so on. In particular, considering a number of reference metallic samples with known electrical conductivity and thickness and using the ECP defined in Step # 1.1, several experimental tests have been carried out for each excitation frequency used to create the simulated level curves (Step # 1.2) obtaining the experimental values of $\Delta\dot{Z}_m$ ($\Delta\dot{Z}_{m,exp}$). A calibration factor c is then evaluated by the ratio between numerical and experimental results for each considered frequency:

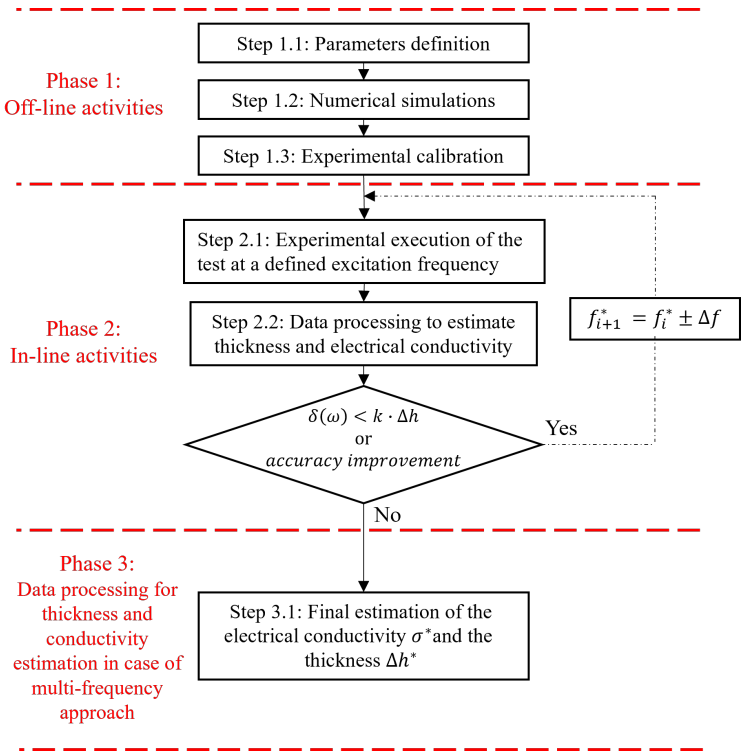

Figure 4.11: Operation flow-chart behind the $\Delta h - \sigma$ estimation process.

$$c(f) = \frac{\Delta \dot{Z}_{m,sim}(f)}{\Delta \dot{Z}_{m,exp}(f)}. \tag{4.17}$$

Phase 2: In-line activities

2.1 *Experimental execution of the test at a defined excitation frequency*

This step consists of the experimental acquisition of the data to evaluate $\Delta \dot{Z}_{m,exp}$. This is an in-line experimental measurement activity performed at a defined excitation frequency (f^*) chosen from the values adopted in Step # 1.1, on a SUT with unknown thickness and electrical conductivity (inside the ranges defined in Step # 1.1). This step can be performed at only one frequency or repeated at other frequency values in order to improve the quality in the measure of the unknown thickness and conductivity.

2.2 *Data processing to estimate thickness and electrical conductivity*

Firstly, to the obtained experimental $\Delta\dot{Z}_{m,exp}(f^*)$, the calibration factor $c(f^*)$ is applied and the check of compliance with the feasibility region defined in Fig. 4.6 is made. Then, according to the dimensionless groups defined in Table 4.2, the $Re\{\bar{\pi}_{1,exp}\}^*$, $Im\{\bar{\pi}_{1,exp}\}^*$, $|\bar{\pi}_{1,exp}|^*$, $\underline{/(\bar{\pi}_{1,exp})^*}$ values are calculated. Each one of these values corresponds to a dimensionless curve on the simulated contour map obtained in Step # 1.2. Finally, the point of intersection of the four level curves is found in order to estimate the π_2^* value for the x-axis coordinate and the π_3^* value for the y-axis coordinate (as represented in the Fig. 4.4 and Fig. 4.5).

Given the π_2^* and the π_3^* estimated quantities, the thickness can be evaluated as $\Delta h^* = D\pi_3^*$ while the electrical conductivity can be evaluated as $\sigma^* = \frac{2\nu_0}{2\pi f^*}\left(\frac{\pi_2^*}{D}\right)^2$.

It is worth noting that phase 2 is repeated at a different frequencies in two possible cases: either for a failure in the check of compliance with the feasibility region or to improve the accuracy of the estimate of the thickness and the electrical conductivity, leveraging measurements from different frequencies.

Phase 3: *Data processing for thickness and electrical conductivity estimation in case of multi-frequency approach*

This last phase is made only if the operator has decided to use more than one frequency to execute the measurement of thickness and conductivity. This choice is made with the purpose to improve the measurement uncertainty since for each frequency can be made a $\Delta h - \sigma$ estimation. So it is possible to make suitable choices for the definition of the final results such us evaluating them as the mean value of the Δh and σ values obtained at the different frequencies.

4.3.5 Case studies and experimental set-up

The experimental tests were carried out on six samples with known thicknesses and electrical conductivities. The main characteristics of the considered samples are shown in Table 4.6 and are contained in the parameter ranges (see Step # 1.1) used to create the simulated dimensionless curves (see Step # 1.2).

The experimental set-up was described in Section 3.6. In addition, the metrological characterization of the proposed measurement method were carried out. In particular, the tests were realized at different excitation frequencies by applying a swept-sine signal to feed the exciting coil (so also the Phase 3 described in subsection 4.3.4 has been carried out). In particular, the considered frequency range was from 300 Hz to 3 kHz, with a frequency step equal to 50 Hz. For each applied sine

Table 4.6: Main characteristics of analyzed samples [52].

Name code	Metal alloy	Electrical conductivity ($\widetilde{\sigma}$) [MS/m]	Thickness ($\widetilde{\Delta h}$) [mm]	sample dimensions [mm x mm]
#a	Aluminium (2024-T3)	17.66	2.03	200 x 200
#b	Copper	58.50	0.98	200 x 200
#c	Aluminium (6061-T6)	28.23	1.97	200 x 200
#d	Aluminium (AW-1050A)	35.27	1.03	250 x 250
#e	Aluminium (AW-1050A)	35.44	2.93	250 x 250
#f	Aluminium (AW-1050A)	35.91	3.98	250 x 250

signal, the RMS current value of 115 mA is considered. The conditioning unit is characterized by a bandpass filter with a bandwidth between 30 Hz and 10 kHz and an amplification gain of 200 for the voltage proportional to the excitation current and 100 for the output voltage on the receiver coil. In order to optimize the data processing in the time domain, the signals digitization is performed by adopting a sampling frequency 1000 times the considered signal frequency and acquiring 4 periods of each signal. A script developed in the MATLAB^{TM} environment, running on a dual-core PC, manages the automation of the whole developed measurement station and performs the signal processing to evaluate the desired quantities. The final outputs are the mutual impedances $\dot{Z}_{m,air}$ and $\dot{Z}_{m,sample}$ considering the tests carried out on the air and the conductive sample respectively.

4.3.6 Experimental characterization of the proposed measurement method

In this subsection the experimental campaign is described. For each considered sample and for each adopted excitation frequency value, 20 repeated measurements were carried out to investigate the repeatability in the estimation of both Δh and σ. To quantitatively analyze the goodness of the proposed method, the following figures of merit have been defined.

- The average of both the thickness ($\overline{\Delta h}_f$) and the electrical conductivity ($\overline{\sigma}_f$) at each frequency, calculated as the average of all the electrical conductivities and thicknesses estimated for the 20 repetitive measurements carried out at each considered frequency.
- The mean absolute relative error of the estimated thickness ($\epsilon_{rf,\Delta h}$) and electrical conductivity ($\epsilon_{rf,\sigma}$) at each frequency with respect to the corresponding known values (see equations (4.18) and (4.19) respectively).

$$\epsilon_{rf,\Delta h} = \frac{|\overline{\Delta h}_f - \widetilde{\Delta h}|}{\widetilde{\Delta h}} \cdot 100 \tag{4.18}$$

$$\epsilon_{rf,\sigma} = \frac{|\overline{\sigma}_f - \widetilde{\sigma}|}{\widetilde{\sigma}} \cdot 100 \tag{4.19}$$

- The standard deviation of the 20 obtained relative errors at each frequency $std_{\epsilon_{rf,\Delta h}}$ and $std_{\epsilon_{rf,\sigma}}$.
- The overall obtained average thickness ($\overline{\Delta h}$) and electrical conductivity ($\overline{\sigma}$): it can be calculated as the average of all the thicknesses and electrical conductivities estimated for each excitation frequency and for each repetition for the considered frequency.
- The mean absolute relative error of the estimated thickness ($\epsilon_{r,\Delta h}$) and electrical conductivity ($\epsilon_{r,\sigma}$) with respect to the nominal thickness and electrical conductivity respectively (see equations (4.20) and (4.21) respectively).

$$\epsilon_{r,\Delta h} = \frac{|\overline{\Delta h} - \widetilde{\Delta h}|}{\widetilde{\Delta h}} \cdot 100 \tag{4.20}$$

$$\epsilon_{r,\sigma} = \frac{|\overline{\sigma} - \widetilde{\sigma}|}{\widetilde{\sigma}} \cdot 100 \tag{4.21}$$

- The estimated absolute standard deviations ($std_{\Delta h}$, std_{σ}) on all the estimated thicknesses and electrical conductivities.
- The estimated relative standard deviations ($std_{\epsilon_{r,\Delta h}}$ and $std_{\epsilon_{r,\sigma}}$) on overall absolute relative errors.

In detail, for all the considered frequencies that fall inside the feasible operating area, Fig. 4.12 shows the behaviour of the mean absolute relative errors $\epsilon_{rf,\Delta h}$ (a), and the corresponding standard deviation $std_{\epsilon_{rf,\Delta h}}$ (b) related to the thickness estimation. The corresponding figures of merit in the case of conductivity estimation are reported in Fig. 4.13 (a) ($\epsilon_{rf,\sigma}$) and Fig. 4.13 (b) ($std_{\epsilon_{rf,\sigma}}$).

As expected, for all the analysed samples, both the error and the standard deviations are generally more significant at low excitation frequencies for both Δh and σ (due to the weakness of the eddy current at those frequency values). Increasing the excitation frequencies, relative error assumes suitable values always lower than 5 % for the thickness and 4 % for the electrical conductivity. Similar behaviors can be observed for the standard deviations (see Fig. 4.12 (b) and Fig. 4.13 (b)). The obtained results prove the suitability of the proposed method to measure both thickness and electrical conductivity with a single frequency measurement. This is confirmed by the minimum values obtained for the errors and standard deviations of both thickness and conductivity that can reach values lower than 0.1 %.

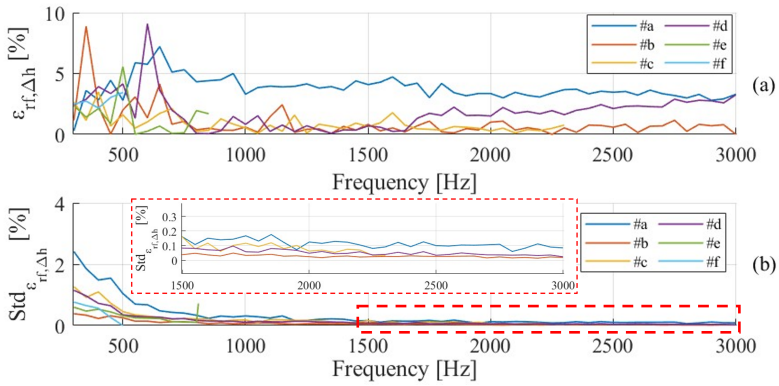

Figure 4.12: (a) Behaviour of the mean relative error ($\epsilon_{rf,\Delta h}$) and (b) the corresponding relative standard deviation ($std_{\epsilon_{rf,\Delta h}}$) for the estimated thicknesses at different frequencies and for all the considered metallic samples.

Several considerations can be made on the suitable choice of the optimal frequency to be used for the single-frequency approach or the range of frequencies to be adopted if the multi-frequency solution is considered. This kind of analysis are outside the scope of this first experimental validation of the proposed method. It will be made in a future work where a deep metrological characterization will be proposed. To complete the analysis of the data related to this first experimental validation, Tables 4.7 and 4.8 show the considered figure of merits in terms of error and standard deviation on the overall measured data (all frequencies and all repetitions) for the thickness and the electrical conductivity estimation respectively. These results can be seen as a possible output of Phase 3 of the proposed method in the case of a multi-frequency approach. Obviously, the mean values shown in the tables are affected by the poorness of the results at the low-frequency values that could be suitably avoided by selecting the frequency ranges.

4.4 Final discussion and remarks

In this research activity was proposed an ECT method for the simultaneous estimation of thickness and electrical conductivity of conductive samples by using the Buckingham's π theorem. The method has been presented from the concept to an experimental validation carried out on metallic samples with different thicknesses (from 1 to 4 mm) and electrical conductivities (from 17.5 to 58.5 MS/m). The method can be applied to either single or multi-frequency data and its negligible

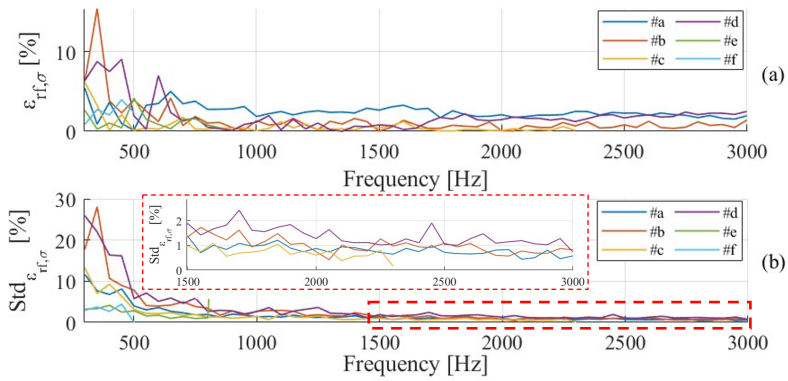

Figure 4.13: (a) Behaviour of the mean relative error ($\epsilon_{rf,\sigma}$) and (b) the corresponding relative standard deviation ($std_{\epsilon_{rf,\sigma}}$) for the estimated thicknesses at different frequencies and for all the considered metallic samples.

computational cost makes it suitable for industrial in-line inspections.

The possibility of applying this method on magnetic materials will also be investigated and developed in future studies. The physical limits of the application of ECT methods on magnetic materials are known in the literature as the relative magnetic permeability has an effect on the depth of penetration of the eddy currents. This issue certainly limits the range of thicknesses that can be analysed, but three different scenarios can be approached: *(i)* in the case of known relative magnetic permeability, the method presented in this work can be applied by replacing the magnetic permeability of the vacuum (μ_0) with the magnetic permeability (μ) in the equations; *(ii)* the double estimation method proposed in this work can be

Table 4.7: Summary of the obtained results for the thickness estimation considering the overall executed tests [52].

Name code	$\widetilde{\Delta h}$ [mm]	$\overline{\Delta h}$ [mm]	$std_{\Delta h}$ [mm]	$\epsilon_{r,\Delta h}$ [%]	$std_{\epsilon_{r,\Delta h}}$ [%]
#a	2.03	2.10	0.18	3.78	0.97
#b	0.984	0.981	0.091	0.40	1.34
#c	1.97	1.98	0.17	0.51	0.71
#d	1.03	1.02	0.14	0.91	1.45
#e	2.93	2.90	0.20	0.96	1.55
#f	3.98	3.87	0.19	2.77	0.97

Table 4.8: Summary of the obtained results for the electrical conductivity estimation considering the overall executed tests [52].

Name code	$\widetilde{\sigma}$ [MS/m]	$\overline{\sigma}$ [MS/m]	std_σ [MS/m]	$\epsilon_{r,\sigma}$ [%]	$std_{\epsilon_{r,\sigma}}$ [%]
#a	17.66	17.27	2.3	2.18	0.86
#b	58.50	58.44	6.8	0.10	2.2
#c	28.23	28.26	4.8	0.11	1.1
#d	35.27	35.77	4.2	1.44	2.1
#e	35.44	35.33	2.1	0.31	1.1
#f	35.91	36.76	2.3	2.38	0.86

applied by considering a different development of the dimensionless groups. In this case, the a priori knowledge of the electrical conductivity (σ) or thickness (Δh) of the analyzed sample will be required; *(iii)* a new method can be developed for the simultaneous estimation of three parameters (σ, Δh and μ) not by means of the intersection of the dimensionless curves but by means of the intersection of dimensionless surfaces.

In addition,a complete metrological characterization with respect of the thickness estimation was also realized and it is described in the next subsection.

4.5 Metrological characterization of the thickness estimation method based on Buckingham's π theorem

After an initial introduction of the Buckingham method applied for the simultaneous estimation of thickness and conductivity, an initial metrological characterisation phase was carried out in order to get to know the full potential of the method proposed in [52]. In addition, Fig. 4.14 shows the versatility of the method and the readiness of the method to be used for both double-estimation methods (as described in the previous section) and single-estimation methods (e.g. methods useful for the single measurement of thickness or electrical conductivity).

In this Section, it was carried out a first metrological characterization of the method described in the previous Sections and in [52]. In particular, the attention is focused on the analysis of the performance in the thickness estimation using single frequency or multiple frequencies approaches, different features to be used in the estimation, and the possibility to adopt data fusion techniques.

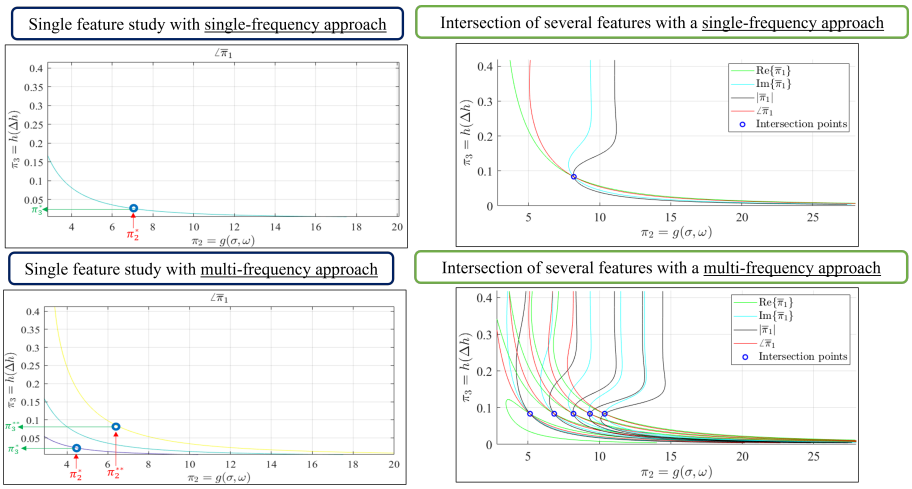

Figure 4.14: Representation of the various estimation methods that can be implemented using a dimensional analysis approach.

4.5.1 Description of the single parameter estimation

The single parameter estimation (in this case the thickness estimation) process can be summarized through the following five-step procedure. This procedure consists of a preliminary phase carried out off-line (Steps 1,2) and a measurement and estimation phase of the unknown thickness carried out on-line (Steps 3,4,5).

- *Step 1: Compute the reference dimensionless curves for the measurement system by means of simulations.*

  This step consists of an off-line simulation phase in which, giving all the parameters involved in the problem (e.g. ECP geometry, the main physical properties of the analyzed sample and the excitation frequencies) the dimensionless curves are evaluated. The parameters summarized in Table 4.3 are used for obtaining the dimensionless curves. In detail, for each value of thickness and excitation frequency, the corresponding value of $\Delta\dot{Z}_m$ is obtained, by means of the numerical simulation carried out simulation tools or semi-analytic models. Then, the resulting values of the π groups (π_1, π_2, π_3) can be calculated.

- *Step 2: Experimental calibration.*

  In order to use the dimensionless curves simulated in Step 1 to estimate unknown thickness from experimental results, a suitable experimental calibra-

tion phase is needed. The goal is to verify the agreement between simulated and experimental data. This phase is necessary due to the uncertainty in the knowledge of the geometric and physical characteristics of the ECP, experimental noise, measurement uncertainty, etc. In particular, considering several reference conductive samples with known electrical conductivity and thickness and using the adopted ECP, different experimental tests have been carried out for each used excitation frequency. In detail, during this experimental test the quantity $\Delta\dot{Z}_{m,exp}$ has been measured. The corresponding simulated values of the reference quantity ($\Delta\dot{Z}_m$) are obtained under the same conditions . A calibration factor "c" (describe in the previous Section) is then evaluated by the ratio between numerical and experimental results for each considered frequency. This step is also performed off-line and only needs to be repeated if the adopted ECP changes.

- *Step 3: Perform frequency-dependent impedance measurements.*

  Given the conductive sample with unknown thickness, the measurements of $\dot{Z}_{m,air}$ and $\dot{Z}_{m,plate}$ are performed at a defined excitation frequency (f^*) chosen inside the values adopted in Step 1. It consists of an on-line experimental measurement step.

- *Step 4: Obtain experimental values of $\phi(\pi_1)^*$ (or $Re(\pi_1)^*$,$Im(\pi_1)^*$, $|(\pi_1)|^*$) and π_2^* and match with the dimensionless curve.*

  Once the test frequency f^* of the excitation signal is fixed, the corresponding value of π_2^* is evaluated. At the same frequency, the value of $\Delta\dot{Z}_m^*$ is evaluated from the $\dot{Z}_{m,air}^*$ and $\dot{Z}_{m,plate}^*$ measured in Step 3 and it is multiplied by the calibration factor "c" calculated in Step 2, allowing to evaluate the $\phi(\pi_1)^*$. The intersection of the dimensionless curve corresponding to the $\phi(\pi_1)^*$ (or $Re(\pi_1)^*$,$Im(\pi_1)^*$, $|(\pi_1)|^*$) value and the vertical line passing through the π_2^* value will identify a corresponding π_3^* quantity.

- *Step 5: Estimation of the unknown thickness Δ^*.*

  Given the π_3^* quantity, the unknown thickness can be evaluated as $\Delta^* = D{\cdot}\pi_3^*$

4.5.2 Obtained experimental results in different working conditions

In this subsection are described the metrological performance of the method in the case of single thickness estimation. The experimental set-up and the case studies were described in subsection 4.3.5 while the considered features and the analyzed excitation frequencies were described in subsection 4.3.6. In order to show the

effect of the thickness of the analyzed samples, Table 4.6 has been reorganized so that the samples analysed are of increasing thickness.

Table 4.9: Analysed samples organised in order of increasing thickness.

Name code	Metal alloy	Electrical conductivity [MS/m]	Thickness ($\overline{\Delta}$) [mm]
#a	Copper	58.50	0.985
#b	Aluminium (AW-1050A)	35.27	1.030
#c	Aluminium (6061-T6)	28.23	1.973
#d	Aluminium (2024-T3)	17.66	2.027
#e	Aluminium (AW-1050A)	35.44	2.927
#f	Aluminium (AW-1050A)	35.91	3.981

Fig. 4.15 shows the behavior of the mean absolute relative errors ($\epsilon_{rf,\Delta h}$) while the corresponding standard deviation ($std_{\epsilon_{rf,\Delta h}}$) related to the thickness estimation is shown in Fig. 4.16.

In Fig. 4.15, as expected, it can be shown that $\epsilon_{rf,\Delta h}$ obtained by single-thickness estimation generally provides better or similar performance if compared to the simultaneous double estimation case [52]. In general, the error reaches larger values for low frequencies and high frequencies, while it reaches smaller errors in the case of medium frequencies. In particular, in the mid-frequency range, it reaches adequate values and is always less than 3%, also considering the dispersion due to repeatability ($std_{\epsilon_{rf,\Delta h}}$). This aspect allows us to confirm that the method can provide good performance for thickness estimation with a single-frequency measurement, with a suitable choice of excitation frequency.

About the standard deviation of the mean absolute relative error ($std_{\epsilon_{rf,\Delta h}}$) shown in Fig. 4.16, the value decreases as the excitation frequency increases; generally, $std_{\epsilon_{rf,\Delta h}}$ in the case of single-thickness estimation is lower than in the case of simultaneous double estimation. The results obtained can be traced back to the theoretical framework in which, if the frequency is too high, the electromagnetic interaction is localised only on the surface of the sample and only thin thicknesses can be analysed correctly. If the frequency is low, the penetration depth of the eddy currents increases and larger thicknesses can be analysed. On the other hand, by using a small excitation frequency, the amplitude of the eddy current in the sample becomes weak, reducing the signal-to-noise ratio of the acquired data (as can be seen from the standard deviation, which is significantly higher than at low frequencies).

From Figs. 4.15-4.16, single-thickness estimation generally performs better in terms of error and repeatability than double simultaneous estimation.

In Table 4.10 are shown the resulting values of $\overline{\Delta}$, $std_{\overline{\Delta}}$, $\epsilon_{r,\Delta h}$ and $std_{\epsilon_{r,\Delta h}}$ for each analyzed sample. It can be shown that considering all the measurements performed in the frequency range considered, the mean absolute relative error is

always lower than 2.3%.

Table 4.10: Summary of the obtained results for the thickness estimation considering the overall executed tests.

Name code	$\widetilde{\Delta}$ [mm]	$\overline{\Delta}$ [mm]	$std_{\overline{\Delta}}$ [mm]	$\epsilon_{r,\Delta h}$ [%]	$std_{\epsilon_{r,\Delta h}}$ [%]
#a	0.985	0.983	0.010	0.23	0.55
#b	1.030	1.043	0.013	1.24	0.61
#c	1.973	1.981	0.027	0.42	0.70
#d	2.027	2.070	0.039	2.12	0.71
#e	2.927	2.890	0.043	1.25	0.94
#f	3.981	3.890	0.092	2.28	0.96

Finally, in view of the application of a single-frequency approach, the performances in terms of accuracy and repeatability are analyzed. Table 4.11 shows the obtained performances by using an "optimal"excitation frequency range ($f_{range,opt}$) for each analyzed sample and for each possible feature analyzable ($Re(\pi_1)$, $Im(\pi_1)$, $|(\pi_1)|$ and $\phi(\pi_1)$). The "optimal"excitation frequency range is defined as the range of frequency where the values of $\epsilon_{r,\Delta h,f}$ and $std_{\epsilon_{rf,\Delta h}}$ are lower than 2.5%.

In Table 4.11 the mean relative error ϵ and its standard deviation $std_{\epsilon_{r,\Delta h}}$ are evaluated as the mean of the values obtained inside the considered optimal frequency range. It is possible to note as ϵ and $std_{\epsilon_{r,\Delta h}}$ do not exceed 2.3% and 0.89%, respectively (except in case #f using the feature $Re(\pi_1)$ for the thickness estimation).

As shown in Table 4.11, the feature $\phi(\pi_1)$ grants a wider optimal frequency range and, usually, allows better performances with respect to the other features in terms of ϵ while the figure of merit $std_{\epsilon_{r,\Delta h}}$ shows a general uniformity of the results. In fact, as shown in Fig.4.2(d), the phase $\phi(\pi_1)$ is the feature that guarantees monotonous trends of the dimensionless curves in a wider range of π_2 and π_3 (so in a wider range of frequency and thickness).

Analyzing the other features, it can be seen that the $Re(\pi_1)$ feature allows better performance for higher frequencies because the dimensionless curves related to this feature have monotonous trends only for high-frequency values (see Fig.4.2(a). With regard to the characteristics $Im(\pi_1)$ and $|(\pi_1)|$, better performance can be obtained for an optimal frequency range concentrated at low frequencies. This is the reason for the general deterioration in performance obtained with these characteristics. In fact, at low frequencies, the eddy currents are lower and, consequently, the experimental data are more affected by noise. Finally, as can also be seen in the #f case, the performance cannot be defined as the multiple intersections of the dimensionless curves do not allow the thickness to be estimated.

Table 4.11: Summary of the best results for the thickness estimation considering the optimal excitation frequency range.

Name code	Features	$\widetilde{\Delta}$ [mm]	$\epsilon_{r,\Delta h}$ [%]	$std_{\epsilon_{r,\Delta h}}$ [%]	$f_{range,opt}$ [Hz]
#a	$Re(\pi_1)$	0.990	0.56	0.29	900 ÷ 3000
	$Im(\pi_1)$	0.973	1.25	0.10	300 ÷ 400
	$\|(\pi_1)\|$	0.975	0.98	0.22	300 ÷ 450
	$\phi(\pi_1)$	0.984	0.11	0.28	500 ÷ 3000
#b	$Re(\pi_1)$	1.053	2.18	0.32	2650 ÷ 3000
	$Im(\pi_1)$	1.020	1.00	0.32	300 ÷ 1150
	$\|(\pi_1)\|$	1.023	0.72	0.46	300 ÷ 650
	$\phi(\pi_1)$	1.032	0.20	0.34	400 ÷ 1400
#c	$Re(\pi_1)$	1.986	0.65	0.87	850 ÷ 1600
	$Im(\pi_1)$	1.952	1.05	0.87	300 ÷ 900
	$\|(\pi_1)\|$	1.988	0.76	0.89	300 ÷ 450
	$\phi(\pi_1)$	1.979	0.30	0.36	400 ÷ 1900
#d	$Re(\pi_1)$	1.989	1.90	0.16	850 ÷ 950
	$Im(\pi_1)$	2.005	1.06	0.40	300 ÷ 750
	$\|(\pi_1)\|$	2.011	0.79	0.56	300 ÷ 550
	$\phi(\pi_1)$	2.034	0.35	0.50	350 ÷ 1350
#e	$Re(\pi_1)$	2.890	1.26	0.24	600 ÷ 700
	$Im(\pi_1)$	2.860	2.28	0.16	300 ÷ 450
	$\|(\pi_1)\|$	2.924	0.09	0.13	400 ÷ 450
	$\phi(\pi_1)$	2.895	1.09	0.29	300 ÷ 850
#f	$Re(\pi_1)$	3.855	3.15	2.22	400 ÷ 450
	$Im(\pi_1)$	N/A	N/A	N/A	N/A
	$\|(\pi_1)\|$	N/A	N/A	N/A	N/A
	$\phi(\pi_1)$	3.957	0.60	0.06	300 ÷ 400

As described in the previous Section, the obtained results allow to confirm the goodness of the method to be applied using a single-frequency measurement after an initial characterization of the measurement system required to define $f_{range,opt}$.

In conclusion, to improve the performance, a possible double-frequency approach could be a good solution. The first frequency estimates a first not-optimal thickness estimation that allows to choose the optimal frequency or the frequency range to be adopted in the second and finale measurement. This aspect makes the method suitable and promising for in-line and real-time applications. Other research activity related to the complete characterization of the method in all the possible operating area are currently an open issue.

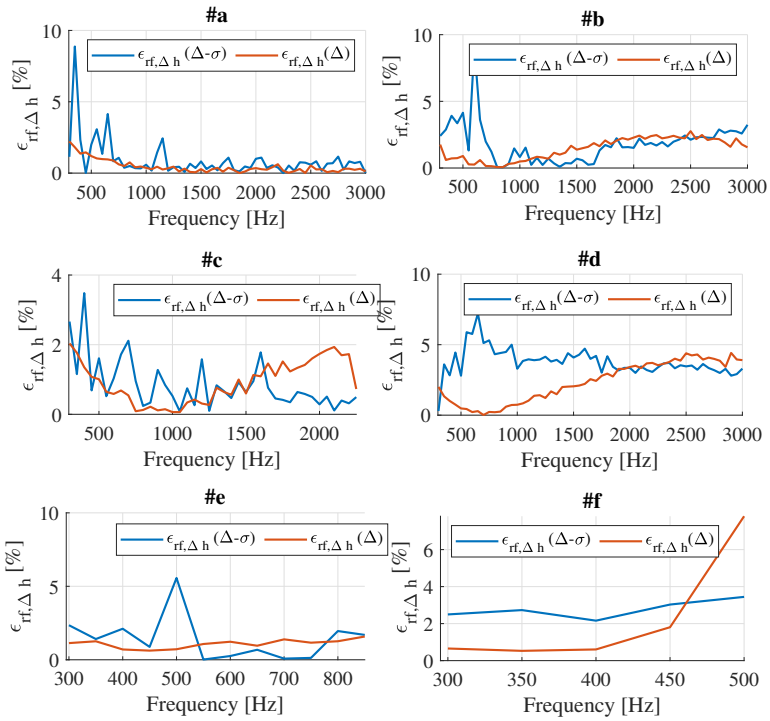

Figure 4.15: Behaviour of the mean absolute relative error ($\epsilon_{rf,\Delta h}$) for the estimated thicknesses at different frequencies and for the considered conductive samples. The blue line represents the $\epsilon_{rf,\Delta h}$ trend in the case of simultaneous double estimation ($\epsilon_{rf,\Delta h}(\Delta - \sigma)$) carried out in the previous Section and in [52], while the red line represents the $\epsilon_{rf,\Delta h}$ trend in the case of single estimation ($\epsilon_{rf,\Delta h}(\Delta)$) [54].

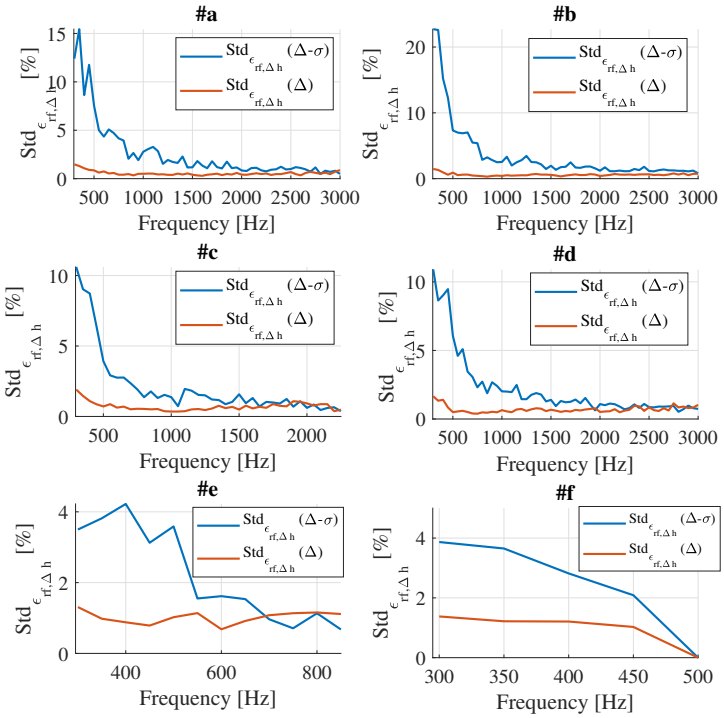

Figure 4.16: Behaviour of the standard deviation of the mean absolute relative error ($std_{\epsilon_{rf,\Delta h}}$) for the estimated thicknesses at different frequencies and for the considered conductive samples. The blue line represents the $std_{\epsilon_{rf,\Delta h}}$ trend in the case of simultaneous double estimation ($std_{\epsilon_{rf,\Delta h}}(\Delta - \sigma)$) carried out in the previous Section and in [52], while the red line represents the $std_{\epsilon_{rf,\Delta h}}$ trend in the case of single estimation ($std_{\epsilon_{rf,\Delta h}}(\Delta)$) [54].

Chapter 5

Enhancing corrosion detection and characterization: an innovative approach with Pot-Core Eddy Current sensor

Corrosion is a widespread problem in various industrial and civil environments. It refers to the deterioration of materials, usually metals, caused by chemical reactions with the surrounding environment [15–17]. It is a massive and costly problem that can lead to structural failure, safety hazards, environmental contamination and significant financial losses [57].

Early detection and characterization of corrosion are crucial in various sectors and they are the basis of the Structural Health Monitoring (SHM) concept [58, 59]. One of the main reasons is safety; in sectors such as aerospace, transport and oil and gas, corrosion can compromise the structural integrity of equipment, vehicles and infrastructure. Early detection of corrosion can help prevent accidents, equipment failures and potential disasters. Other significant factors include cost savings, environmental conservation, longevity of infrastructure and products, etc.

Various methods and techniques are employed for this purpose, including visual inspection [108, 109], chemical material analysis [110, 111], electrochemical meth-

ods[112–115] or Non-Destructive Testing (NDT). Visual testing, chemical material analysis and electrochemical methods (e.g. Electrochemical Impedance Spectroscopy (EIS)) can provide excellent estimates of the corrosion aging and the amount of material lost and the resulting loss of thickness of the sample under test. However, some of these methods, for example the EIS methods, need comparatively expensive equipment and high levels of technical expertise for data analysis [115]. Furthermore, the proposed methods are not in line with the requirements of low-cost, in-situ, remote and real-time testing capability required by the Industry 4.0 paradigm [116, 117].

In recent years, NDT methods are playing an increasingly important role in this context as they meet many of the requirements described above. Different methods related to the Ultrasound testing were proposed [29–31]; they can be used to assess the loss of thickness of metal structures due to corrosion, to detect corrosion hidden under coatings or in hard-to-reach areas and to monitor the progression of corrosion over time with good accuracies. One of the limitations of this method is related to the need to perform the test by manual inspection. This is necessary because the method requires the application of a coupling material to the surface under test. In addition, the measurement is influenced by the roughness of the surface and the cost of surface preparation is a major disadvantage.

Microwave methods were also proposed in [118, 119] with promising results. However, these methods show a strong dependence on the lift-off value, which results in a substantial decrease in measurement sensitivity as the lift-off value increases [118]. In addition, the probe dimension limits the test's speed because it must scan every region with the probe all over the sample surface step by step.

Electromagnetic induction thermography techniques were recently proposed [120, 121]. This technique has the advantages of being non-contact, with a high sensitivity and high resolution also for large lift-off distances, which contributes to on-site detection and characterization. By the way, a high-current supplier is necessary to drive the excitation coil to generate a high-frequency eddy current in the conductive samples. This aspect makes the method unsuitable for portable or remote sensing applications.

In order to realize low-cost and low-power sensors suitable for continuous or periodic monitoring, several studies have been also conducted. In [122], a chipless RFID sensor was developed for corrosion characterization; in particular, through the frequency selective surface and the confidence-weighted averaging feature fusion they obtained promising results.

In this context, ECT methods show to be suitable with the required characteristics. In [123], an in-depth characterization of atmospheric corrosion was carried out. Using Pulsed Eddy Current (PEC), different electrical features were analyzed,

showing the correlation between the features and the corrosion aging. It was shown that even in early corrosion (below 12 months) the trend obtained is of exponential order.

In [124], the authors proposed an innovative excitation technique related to the use of Pulse Modulation Waveform (PWM). They have shown that by combining the PWM with the PEC method, the electrical signals had a larger magnitude with respect to traditional PEC signals. This improvement allowed to obtain a better detection and imaging of subsurface corrosion. With the same technique, the authors have shown the enhancement of the evaluation sensitivity to external corrosion and accuracy of corrosion imaging on non-magnetic pipelines [125]. In [126], they applied PMEC technique for the detection and evaluation of the corrosion undercoating in numerical and experimental environments with the conjunction use of an improved Canny algorithm. Also in this case, they obtained very good results in the reconstruction of the corrosion profile with respect to the classic PEC technique.

A PEC-based system for detecting corrosion in carbon steel pipes that are thermally insulated with a composite coating was proposed in [127]. The novelties proposed by the method are related to the signal processing chain, which involves feature extraction using discrete Fourier and wavelet transforms, followed by compacting the information using principal component analysis. The system uses multi-layer perceptron and machine learning neural network architectures for characterization. This method shown good results with very low processing time (about 35 ms).

A different approach has been applied in [128], in this work the authors proposed a feasibility study for the application of a low-power wireless magnetic eddy current sensor for permanent installation to monitor internal corrosion. In addition, they carried out a characterization of the proposed sensor with respect to the chosen AC excitation frequency.

In this activity, the focus was on the hardware section of the measurement system usually adopted in EC methods. In particular, the aim was to develop a low-cost optimized sensor that can estimate the early stages of superficial and hidden corrosion with good accuracy and low-power consumption. To this purpose, an innovative eddy current pot-cored sensor was proposed [56]. From the other side, a swept-frequency approach was applied in order to analyze the quantities of interest as shown in Chapter 3.

The pot-cored consists of a magnetic shielding ferrite core that has a closed magnetic path. It is used to concentrate the magnetic flux on the surface of the sample under test by decreasing the magnetic flux leakage into the air. In addition, it reduces the edge effects that usually affect the results in EC methods.

In particular, the major contributions of this activity were:

- a numerical and experimental analysis in which a comparison is carried out between the commonly used air-cored sensor and the proposed pot-cored sensor;
- a complete characterization of the proposed pot-cored sensor under different analysis conditions including superficial corrosion, hidden corrosion and corrosion under insulating layers;
- a versatile experimental set–up for the estimation of the corrosion state, based on single-frequency or multi-frequency measurements.

Compared with the scientific works already established in the literature, the sensor proposed in this work offered some advantages. Firstly, the energy content of the excitation signal required to achieve good measurement capability is much lower than with classic air-cored sensors. Secondly, the possibility of using a single-frequency excitation approach allows the sensor to be easily integrated into remote monitoring systems with very low measurement times. Thirdly, the integration of an high sensitive Tunnel Magneto Resistance (TMR) sensor allows the measurement system to carry out analysis of very low excitation frequencies, thus enabling analysis with a greater depth of penetration.

This chapter is organized as follows. In Section 5.1 the rationale behind the implementation of the pot-cored sensor and the proposed sensor are shown. The numerical and experimental analysis comparing the air-cored sensor and the proposed pot-cored sensor, the samples analyzed and the proposed measurement set-up are shown in Section 5.2. In Section 5.3 are shown the performance obtained by the proposed pot-cored sensor in different scenarios like the superficial corrosion, hidden corrosion and corrosion under the insulating layer. Finally, the conclusions are drawn in Section 5.4.

5.1 Rationale behind the implementation of the pot-cored sensor

In this Section the rationale behind the use of the pot-cored sensor is explained. The purpose is to show the advantages linked with the sensor structure.

In recent years, other research groups proposed this kind of sensor. In particular, in [60], the pot-cored sensor was applied for the detection of deep subsurface cracks like holes and notches. They shown in numerical and experimental environments how this particular structure can improve sensitivity by allowing the sensor

to detect defects as deep as 7 mm in the case of stainless steel samples with a thickness of 10 mm.

This sensor was proposed also for the application on multilayered conductive discs in [61]. In this paper, the author proposed this sensor as an example case for a numerical model proposed in closed form using the truncated region eigenvector expansion (TREE) method. In [62] the same author proposed the analytical model derived through the TREE method and an experimental validation of the pot-cored sensor applied for the estimation of conductive thin layers and coatings.

With regard to the poor sensitivity and weak signal of the far-field PEC in the detection of hidden defects, in [63] the authors evaluated the detection performance of far-field PEC sensors with various shielding structures by finite-element simulations.

Without loss of generality, the works presented in the literature emphasized the different advantages related to the use of the pot-core sensor. Specifically, it is possible to define that *(i)* the use of a ferromagnetic core in the case of EC probes can improve the spatial resolution of the measure as it concentrates the magnetic flux around the core and it reduces the edge effects usually problematic in the context of the EC methods [60, 129] and *(ii)* the use of the ferromagnetic shield reduces the amount of magnetic flux leakage into the air by concentrating the flux into the area of interest [60, 130].

Despite recent applications, the potential of using the pot-cored sensor is still largely unexplored in various fields related to the world of EC methods.

In this activity, the proposed pot-cored sensor consists of an excitation coil that is placed inside a ferrite pot [56]. The sensing component is represented by a TMR sensor; this sensor is placed at the center of the ferrite pot structure as shown in Fig. 5.1. The excitation coil consists of 120 turns and the copper wire has a diameter of 0.35 mm. The main geometrical characteristics of the pot-cored sensor are described in Table 5.1 while accurate physical and geometrical characteristics of the adopted ferrite structure are available in [131].

In the next Sections, the application of this sensor in the case study of corrosion detection and characterization will be analyzed numerically and experimentally. The aim is to show the potential and limitations of the pot-cored sensor in this application field.

5.2 Performance comparison air-cored and pot-cored sensors

In this Section, the comparison between the commonly used air-cored and the proposed pot-cored sensors (described in the previous Section) is carried out by

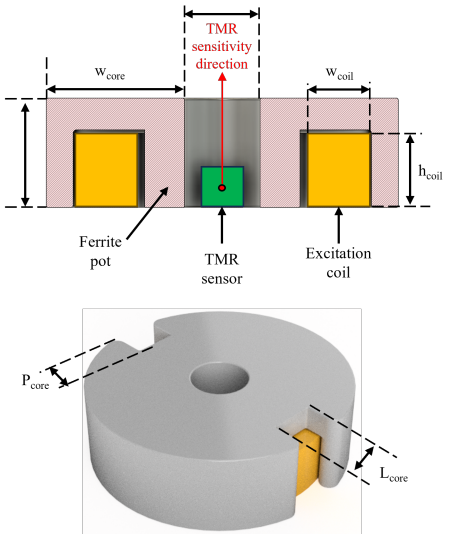

Figure 5.1: Pot-cored sensor representations [56].

means of numerical and experimental analysis.

As concerns numerical comparison, in subsection 5.2.1 an initial analysis was carried out in order to observe the electrical parameters typically analyzed in the context of the EC sensors. In particular, these parameters are related to the distribution of the induced eddy current density and the magnetic field trend.

In subsection 5.2.3, the experimental comparison was carried out on three different cases relating to the corrosion condition: uncorroded sample, sample with the presence of early-stage corrosion (1 month exposure time) and sample with the presence of long-term corrosion (10 months exposure time).

5.2.1 Numerical Comparison

The numerical simulations were performed in COMSOL Multiphysics (version 6.0), employing the AC/DC module and selecting the magnetic fields with frequency domain equations.

The numerical model replicates the adopted experimental air-cored and pot-cored sensors. The excitation coil composing the air-cored sensor has the same geometrical characteristics as the excitation coil composing the pot-cored sensor described in Table 5.1. Instead, the measuring point describing the TMR sensor is located in the centre of the coil as shown in Fig.5.1.

In particular, the measurement point has been considered as the middle point of

Table 5.1: Main geometrical characteristics of the Pot-cored sensor [56].

Parameter	Value [mm]
w_{core}	9.74
h_{core}	7.66
P_{core}	3.60
L_{core}	4.50
k	5.48
w_{coil}	4.52
h_{coil}	5.39

the TMR sensors [132], so in the numerical model, the measurement point will have a lift-off of 3 mm with respect to the analyzed sample. In addition, considering the roughness of the surface, the contact between the sensor and the surface is not optimal; for this reason, a small lift-off of 0.2 mm was also considered for the sensors.

The amplitude of the considered excitation current in all the numerical tests is equal to 50 mA (similar to the experimental case) while the analysis focused on the lowest excitation frequency considered in the experimental studies (e.g. 10 Hz).

The considered sample has dimensions of 100×100 mm^2 with a thickness of 3 mm. The electrical and magnetic characteristics attributed to the samples and implemented in the simulation tool were described in [17]. In particular, the electrical conductivity and relative magnetic permeability of the samples are 4.68 MS/m and 60 respectively.

Regarding the characteristics of the meshes used for the simulation, physics-controlled meshes with an 'extra fine' element size were adopted.

As described above, an initial analysis was conducted taking into account two different parameters: *(i)* the distribution of the induced eddy current density on the sample surface and *(ii)* the magnetic flux in the z-axis direction (e.g. the sensitivity direction considered by the TMR sensor) measured by a measurement point.

Fig. 5.2 and Fig. 5.3 show the distribution of the induced eddy current density on the sample surface by the air-cored and pot-cored sensor, respectively.

From Fig. 5.2 (a), it can be seen that in the case of the air-cored sensor, the highest density of induced eddy currents occurred in the middle of the coil. In addition, the eddy current density also appears to have non-negligible values (half the maximum value) in the area outside the area covered by the coil. On the other

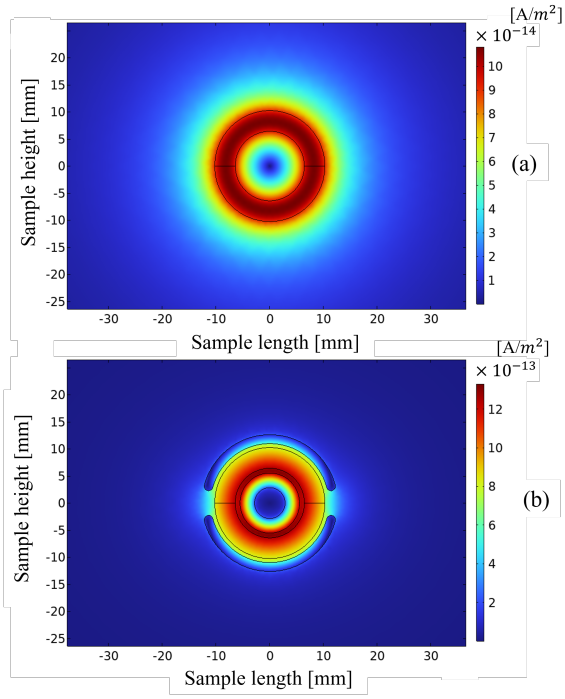

Figure 5.2: Surface representation of the eddy current density distribution at excitation frequency 10 Hz: (a) air-cored sensor; (b) pot-cored sensor.

hand, in Fig. 5.2 (b), it can be seen that for the pot-cored sensor the highest density of induced eddy current occurred at the magnetic core which composes the structure of the pot; thus guaranteeing greater spatial resolution. In addition, the eddy current density is highly negligible in the external area of the shield that composes the pot structure.

Performing a quantitative comparison of the analyzed quantities, it can be seen in Fig. 5.3 that, in the areas of interest, the density of the induced eddy current in the case of the pot-cored sensor provides values ten times higher than with the classic air-cored sensor. This indicates that, with the pot-cored sensor, more magnetic field is gathered in the sample and its magnetism gathering effect is optimal.

Fig. 5.4 analyzes the magnetic flux distribution with respect to the sensitivity axis of the TMR sensor considered (z-axis) in the case of both sensor types studied.

In particular, the trend of the magnetic flux generated in the case of the air-cored sensor can be analyzed from Fig.5.4 (a). From the trends obtained, it can be

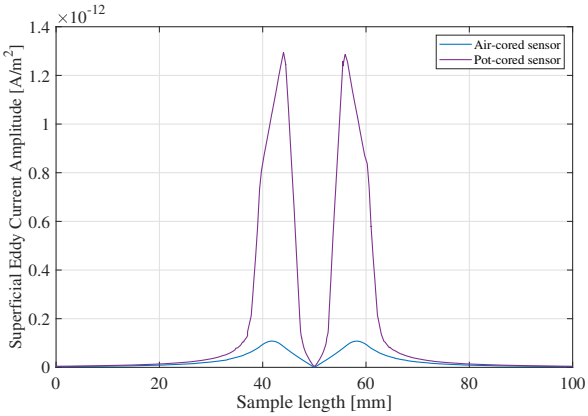

Figure 5.3: Representation of the superficial eddy current density distribution at excitation frequency 10 Hz for the compared sensors.

observed that the flux lines are concentrated below the area covered by the sensor but, at the same time, many flux lines leak into the air in the areas surrounding the sensor.

Observing the magnetic flux lines generated by the pot-cored sensor (Fig. 5.4 (b)), it can be seen that the magnetic flux lines are totally concentrated within the structure of the pot and the area of the sample covered by the pot-cored sensor. In addition, the intensity of the magnetic flux in correspondence of the sample area subtended by the sensor is ten times greater than in the case of the air-cored sensor.

From the comparison results, it is therefore possible to confirm what was defined in Section 5.1. In fact, it is observed that the application of the pot structure on the EC sensors can improve the spatial resolution as it concentrates the magnetic flux around the core, reduces the edge effects and the shield composing the pot structure allows the reduction of magnetic flux leakage into the air allowing to concentrate it into the area covered by the sensor.

In the following subsection, the case studies, the experimental set-up and the experimental comparison are shown as described at the beginning of this Section. The aim is to show the performance of the considered sensors from a metrological point of view.

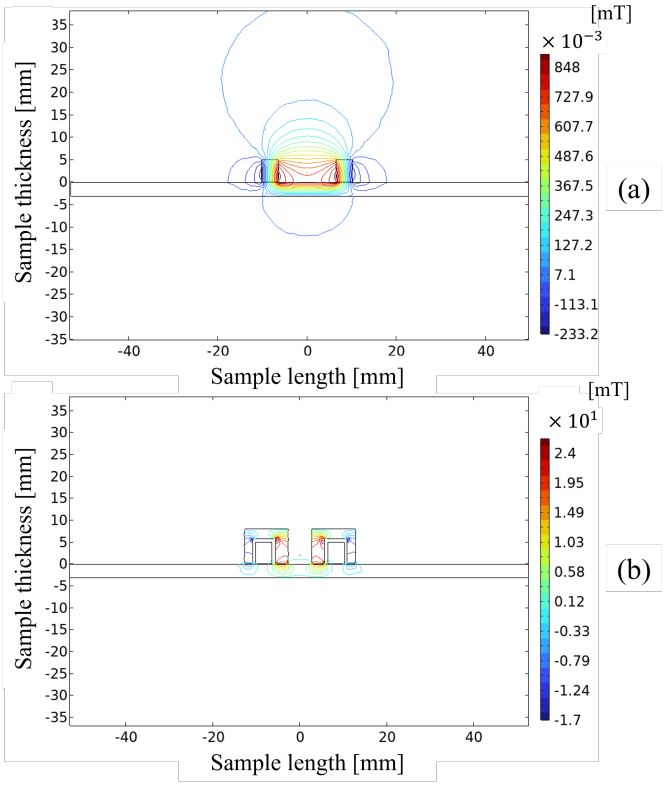

Figure 5.4: Representation of the magnetic flux distribution in the z-axis direction (B_z) at excitation frequency 10 Hz : (a) air-cored sensor; (b) pot-cored sensor.

5.2.2 Considered case studies and experimental set-up

During the experimental study, several uncoated and coated S275 steel samples were tested with different exposure times to corrosive conditions. In particular, the considered exposure times are 1, 3, 6, 10 and 12 months as listed in Table 5.2.

The steel S275 is suitable for numerous structural and general engineering applications. All mild steel samples had dimensions of $300 \times 150\ mm^2$, with a thickness of 3 mm. These mild steel samples were covered with plastic tape, except for the central area (approx. $30 \times 30\ mm^2$ as shown in Fig. 5.5), to keep the rest of the steel as a clean region. After the tape was applied, these samples were exposed to a marine atmosphere for different periods (1, 3, 6, 10 and 12 months) to form different stages of atmospheric corrosion. Corrosion progress is the chemical reaction by which metal degrades in a specific environment over the exposure time and

Table 5.2: List of the considered case studies [56].

Metal alloy	Exposure time	Uncoated	Coated
Mild steel S275	No corrosion	x	x
	1 month	x	x
	3 months		x
	6 months		x
	10 months	x	x
	12 months		x

includes the change in corrosion layer properties [123]. Subsequently, some of the samples were covered by 150 μm non-conductive paint as uniformly as possible. S275 steel samples with uniform corrosion produced by atmospheric exposure were supplied by International Paint [123].

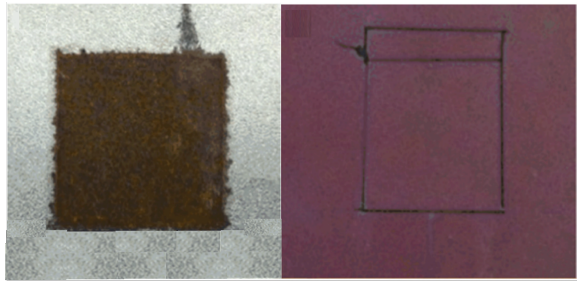

(a) (b)

Figure 5.5: Representation of the corroded area in the case of (a) uncoated and (b) coated sample [56].

For the first part of the study related to the experimental comparison between the air-cored and the pot-cored sensors, three samples were analyzed without the application of the non-conductive paint (uncoated samples). In particular, three cases were analyzed concerning the absence of corrosion, corrosion after 1 month and after 10 months of exposure times. These samples were characterized in terms of average corrosion heights using a laser profilometry in [118]. The corrosion height for the 1 month and 10 months uncoated samples is 43.86 μm and 70.99 μm respectively.

In the second part of the study related to the characterization of the pot-cored sensor, described in Section 5.3, all samples covered by the paint layer were analyzed

(coated samples).

Regarding the experimental set-up, the schematic block diagram is shown in Fig. 5.6. The experimental set-up is composed by the following components: a management and processing unit, an acquisition and generation board, a shunt resistor, a signal amplifier, a power supply and a pot-cored sensor.

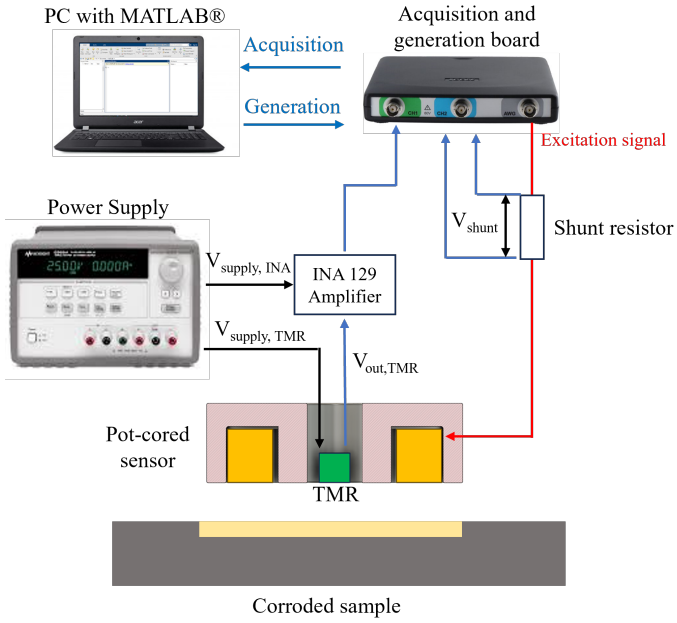

Figure 5.6: Block diagram of the adopted experimental set-up [56].

The proposed pot-cored sensor is shown in Fig. 5.1 and main characteristics are described in Table 5.1 and in Section 5.1. As mentioned above the sensing component consists in a TMR sensor. The TMR sensor is an ultra-high sensitive linear sensor model 2905 produced by 'Multi dimension'. The sensitivity of the sensor is declared to be from 45 to 65 $mV/V/Oe$, characteristics in terms of linearity and sensitivity in AC framework were provided in [133] meanwhile the geometrical characteristics are available in [132].

The TMR sensor is fed by a Keysight E381A power supply with a DC voltage of 6 V while the output signal is amplified by a Texas Instruments INA 129 signal amplifier that is fed by the Keysight E381A with a differential DC voltage of $\pm$ 16 V. A shunt resistor is used to indirectly measure the excitation current feeding the excitation coil. The nominal resistance value of the resistor is 1 Ω with 1% tolerance. Both signals (amplified TMR sensor output signal and voltage of the shunt

resistor) are acquired by the Acquisition board TIE-PIE Engineering Handyscope HS5-540XMS-W5 with a sampling frequency of 100 times the frequency of the exciting signal and 14 bits of resolution. The generation channel of the TIE-PIE represents the generation board and it is used to excite the excitation coil with a sinusoidal swept-frequency signals. The range of frequencies of interest was from 10 Hz to 2000 Hz, with a resolution of 10 Hz and with a root mean square current value of ≈ 50 mA. The management and processing unit includes a MATLAB algorithm running on a dual-core PC for processing the acquired data and managing the acquisition and generation. The processing consists of performing the fast Fourier transform (FFT) for frequency analysis. In addition, it is worth noting that 10 experimental tests were repeated in all case studies in order to define an acceptable number of cases.

5.2.3 Experimental Comparison

This Section shows an experimental comparison between the considered sensors in terms of measurement repeatability, amplitude of the measured quantities, sensitivity and power consumption. The samples previously described in subsection 5.2.2 will be analyzed in this subsection (no corrosion, 1 month and 10 months exposure times).

Two remarks should be made with respect to the measured quantities by the TMR sensor: *(i)* the experimental results will not be normalized in relation to sensitivity but the output voltage of the TMR sensor will be adopted; *(ii)* the TMR sensor was used in the linear condition and its linearity is guaranteed even under alternating magnetic flux conditions as shown in [133].

Further information relates to the amplitude of the excitation current value. As the generation system is voltage impressed, a constant excitation current amplitude is not guaranteed over the entire frequency range analyzed. For these reasons, the analyzed quantity will result from the ratio between the output voltage of the TMR sensor and the current measured by the shunt resistor as shown in Eq. 5.1. The measured quantities are represented in complex form because both of them consist of module and phase obtained by FFT during the signal elaboration.

$$\Delta\dot{G} = \dot{G}_{sample} - \dot{G}_{air} = \frac{\bar{V}_{TMR,sample}}{\bar{I}_{shunt,sample}} - \frac{\bar{V}_{TMR,air}}{\bar{I}_{shunt,air}}. \tag{5.1}$$

In this study, the analysis was carried out over the entire excitation frequency range considered (e.g. from 10 Hz to 2000 Hz).

In Fig. 5.7 and Fig. 5.8 are shown the experimental results obtained using the air-cored sensor and the pot-cored sensor, respectively. In particular, the complex plane of the average trend of the 10 tests performed for each case study is shown.

In this case, the sensors were placed on the corroded area, so the simplest case of superficial corrosion was considered.

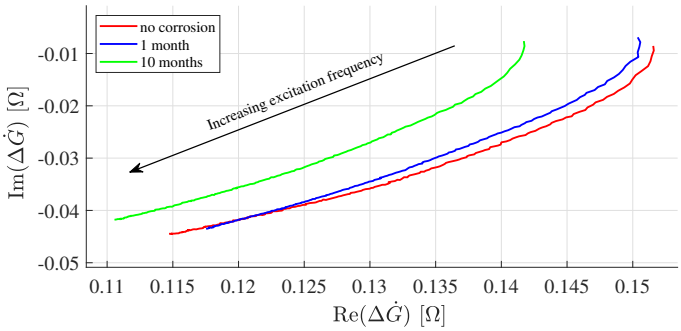

Figure 5.7: Average trends obtained using the air-cored sensor for superficial corrosion on uncoated samples in the different analyzed cases (no corrosion, 1 month exposure time and 10 months exposure time).

From Fig. 5.7 it can be seen that the average trends obtained in the case from the air-cored sensor do not allow a clear distinction between an uncorroded sample and an early corrosion of 1 month while an advanced corrosion state (10 months exposure time) is clearly evident. On the other hand, the average trends obtained by pot-cored sensor (see Fig. 5.8) show a clear distinction between the different corrosion aging. In contrast to what is shown by the air-cored sensor, the pot-cored appears to be particularly sensitive in detecting early-stage corrosions.

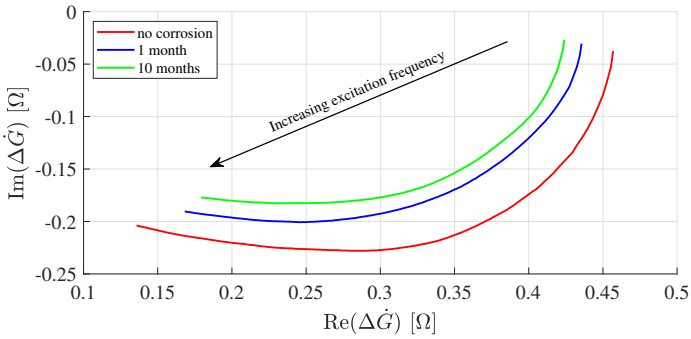

Figure 5.8: Average trends obtained using the pot-cored sensor for superficial corrosion on uncoated samples in the different analyzed cases (no corrosion, 1 month exposure time and 10 months exposure time).

An analysis was carried out also considering the effect of the measurement

repeatability on the quantities of interest ($\mathrm{Re}(\Delta\dot{G})$ and $\mathrm{Im}(\Delta\dot{G})$). For the same measurement set-up and, consequently, for the same measurement resolution, the magnitude of the measured quantities plays an important role in the detection and characterization of the corrosion state.

In order to show this aspect, in Fig. 5.9 and Fig. 5.10 is represented the uncertainty range with 95% confidence level of the measured quantities using the air-cored and the pot-cored sensors respectively. It can be seen that the effect of measurement standard deviations makes it impossible to distinguish between a no-corrosion state and an early-stage corrosion state in the case of air-cored sensor measurements. The low repeatability therefore makes the sensor capable of detecting a long-term corrosion state but not suitable for characterizing it. On the other hand, the pot-cored sensor has very good measurement repeatability which, combined with the clearly distinct trends of the measured quantities, promise excellent performance in terms of characterizing a corrosion state.

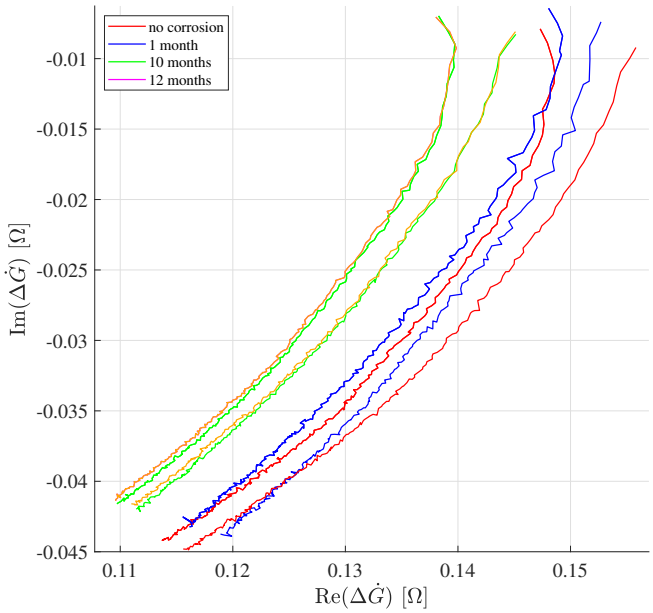

Figure 5.9: Uncertainty range with 95% confidence level of $\mathrm{Re}(\Delta\dot{G})$ and $\mathrm{Im}(\Delta\dot{G})$ measured by the air-cored sensor for superficial corrosion on uncoated samples in the different analyzed cases (no corrosion, 1 month exposure time and 10 months exposure time) [56].

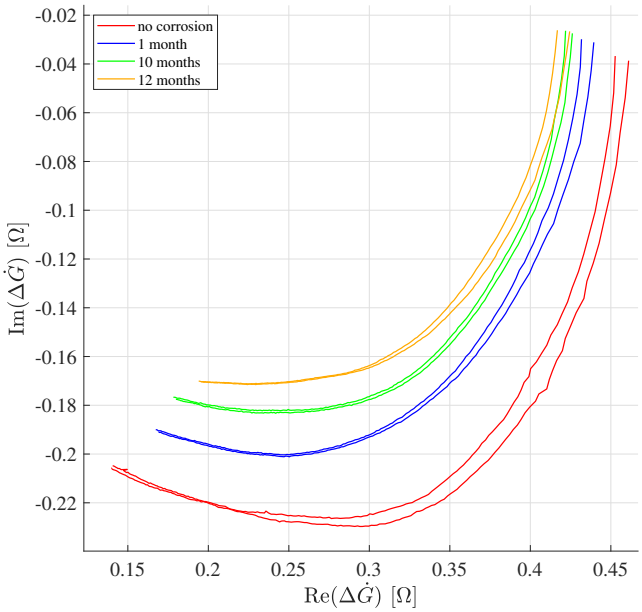

Figure 5.10: Uncertainty range with 95% confidence level of $\mathrm{Re}(\Delta\dot{G})$ and $\mathrm{Im}(\Delta\dot{G})$ measured by the pot-cored sensor for superficial corrosion on uncoated samples in the different analyzed cases (no corrosion, 1 month exposure time and 10 months exposure time) [56].

A comparison in a quantitative way of the amplitudes of the measured quantities $\mathrm{Re}(\Delta\dot{G})$ and $\mathrm{Im}(\Delta\dot{G})$ is realized. The amplitudes measured by the pot-cored sensor are greater by a multiplication factor of approximately $1-8$ compared to the air-cored sensor.

In Fig. 5.11 the ratio of the quantities of interest between the two sensors considered is shown in detail. In particular, over the range of excitation frequencies considered, it is possible to note how the ratio in the case of $\mathrm{Re}(\Delta\dot{G})$ reaches values equal to 3 while in the case of $\mathrm{Im}(\Delta\dot{G})$ the ratio reaches values equal to 8. The ratios reach their maximum value in the case of low frequencies, confirming the predisposition of the pot-cored sensor for use at low excitation frequencies and thus guaranteeing the application of the sensor also for thick structures.

An analysis of the sensitivity of the two sensors with respect to the range of excitation frequencies was also carried out. In particular, the sensitivity of the $\mathrm{Re}(\Delta\dot{G})$ and $\mathrm{Im}(\Delta\dot{G})$ quantities was analyzed as shown in Eq. 5.2 and Eq. 5.3

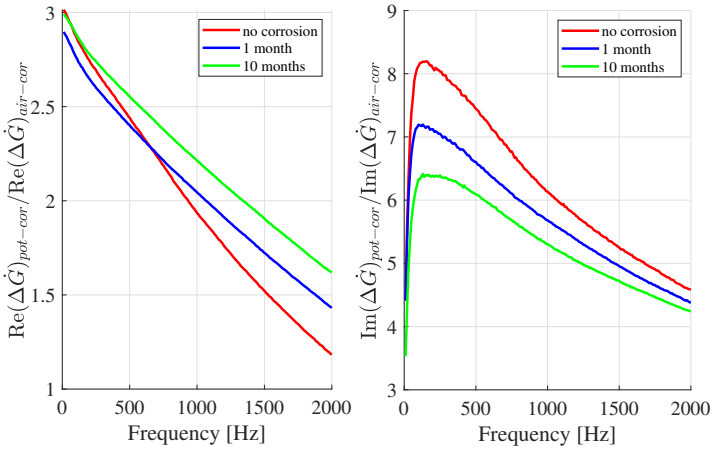

Figure 5.11: Average trends for the ratio between pot-cored and air-cored sensors of $\mathrm{Re}(\Delta\dot{G})$ and $\mathrm{Im}(\Delta\dot{G})$ for superficial corrosion on uncoated samples in the different analyzed cases (no corrosion, 1 month exposure time and 10 months exposure time).

respectively. In addition, the obtained results are represented in Fig. 5.12.

$$S_{real} = \frac{d(Re(\Delta\dot{G}))}{df} \tag{5.2}$$

$$S_{imag} = \frac{d(Im(\Delta\dot{G}))}{df} \tag{5.3}$$

As can be seen from Fig. 5.12, the sensitivity of the proposed pot-cored sensor is about ten times higher in the case of the quantity S_{real} in all the considered frequency range.

Similar results are obtained in the case of the quantity S_{imag}; the sensitivity is about ten times higher using the pot-cored sensor. In this case, the pot-cored sensor guarantees greater sensitivity up to an excitation frequency of 500 Hz. Again, the good performance of the sensor at low excitation frequencies are well emphasized.

Finally, considering the power consumption of the sensors, the average root mean square value of the absorbed excitation current of the air-cored sensor in the considered frequency range is 67.14 mA with a standard deviation of 0.139 mA, whereas the pot-cored sensor has an average value of 55.54 mA with a standard deviation of 6.21 mA. Generally, the pot-cored sensor absorbs a lower excitation current than the classic air-cored sensor while still achieving better metrological performance.

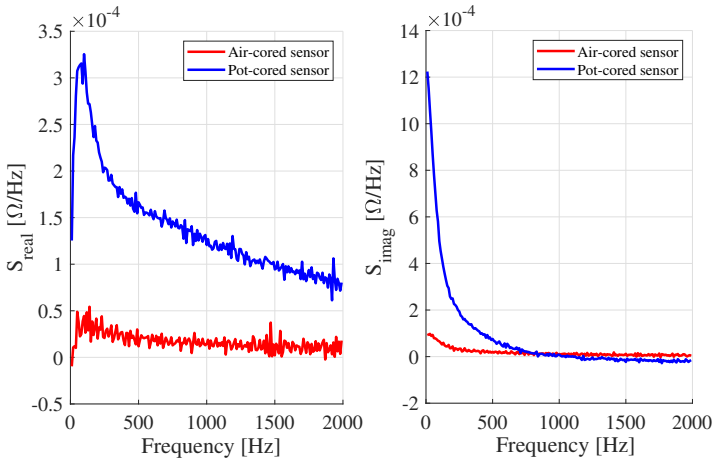

Figure 5.12: Average sensitivities S_{real} and S_{imag} trends obtained in the case of air-cored and pot-cored sensors with respect to the frequency excitation [56].

In conclusion, from the numerical and experimental results, it can be stated that the use of the pot-cored sensor can improve the metrological characteristics of the measurement set-up compared to the use of the classic air-cored sensor. In the next Section, a detailed experimental analysis of the performance achievable by the pot-cored sensor with respect to the considered scenarios will be carried out.

5.3 Experimental performance of the pot-cored sensor and discussion

This Section shows the performance of the proposed pot-cored sensor in different scenarios. In particular, three scenarios are referred to concerning *(i)* the superficial corrosion, *(ii)* the hidden corrosion and *(iii)* the corrosion under the insulating layer. The different scenarios analyzed are schematically represented in Fig. 5.13.

In all case studies, the coated samples described in subsection 5.2.2 were analyzed, the electrical parameters adopted for the execution of the experimental test have been described also in subsection 5.2.2 and analyzed quantities have been described in subsection 5.2.3.

5.3.1 First scenario: Superficial corrosion

In this framework, as superficial corrosions were analyzed, the entire set of available excitation frequencies (from 10 Hz to 2000 Hz) was investigated. The aim is to

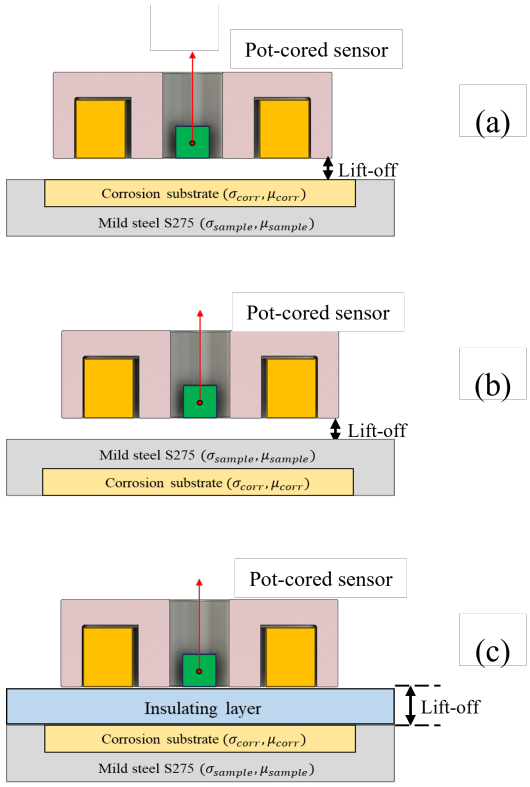

Figure 5.13: Schematic representation of the considered scenarios: (a) superficial corrosion case, (b) hidden corrosion case and (c) corrosion under the insulating layer case [56].

observe the two measured quantities ($\mathrm{Re}(\Delta\dot{G})$, $\mathrm{Im}(\Delta\dot{G})$) in order to define in which case the best performance are obtained.

In Fig. 5.14 are shown the average trends of the 10 repeated tests performed for each case study using the pot-cored sensor, each marker represents an analysed excitation frequency.

As can be seen, the trends obtained in the analyzed frequencies show a very good sensitivity of the sensor with respect to the considered corrosion aging. In particular, the trends are clearly distinct for low excitation frequencies where the sensor shows greater sensitivity (as shown in Fig. 5.12) while they tend to overlap as the excitation frequency increases due to the decreasing of sensitivity and depth of penetration (described in Eq. 2.1).

In order to show the goodness of the pot-cored sensor and to carry out a metro-

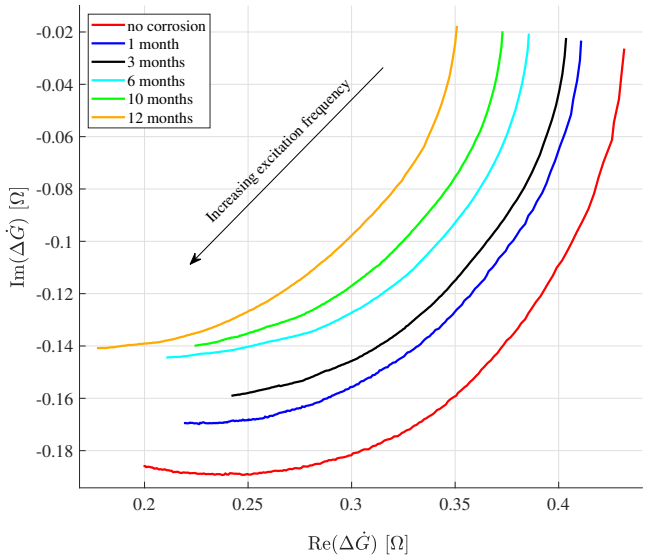

Figure 5.14: Average trends obtained using the pot-cored sensor for superficial corrosion on coated samples in all the considered analyzed cases [56].

logical analysis, the fitted lines of the average values obtained by $\mathrm{Re}(\Delta\dot{G})$ and $\mathrm{Im}(\Delta\dot{G})$ at the minimum, the maximum and middle frequencies of the adopted range (10 Hz, 1000 Hz and 2000 Hz) are represented in Fig.5.15 and Fig. 5.16. In addition, the repeatability of the obtained values is represented in the figures, in fact, the standard deviation is also represented using the vertical bars.

In both the figures, the solid lines represent the fitted lines for the considered case studies, which are fitted according to the power function (as already established in [123]):

$$C = At^n + q, \tag{5.4}$$

where, t is the exposure time in months, C are the features $\mathrm{Re}(\Delta\dot{G})$ and $\mathrm{Im}(\Delta\dot{G})$ after t, A are the features in the first month, q is the offset and n is a constant.

From Fig. 5.15 it is possible to analyze the behavior of the $\mathrm{Re}(\Delta\dot{G})$ feature as the excitation frequencies change. In particular, this feature shows to be in line with the exponential trend for low excitation frequencies while as the excitation frequency increases, the trends do not respect this particular trend. The low performance obtained for high frequencies can be attributed to the decrease of the amplitude of the measured quantity and the decrease in sensor sensitivity. In ad-

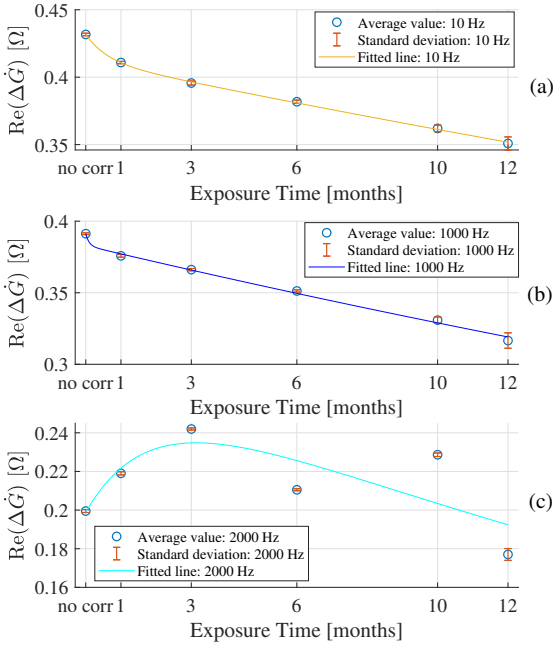

Figure 5.15: Measured average values, relative standard deviation and fitted lines of $\mathrm{Re}(\Delta\dot{G})$ for the coated samples [56].

dition, it can be seen that the standard deviation of the acquired signals is very low; it allows good measurement repeatability guaranteed by the sensor.

In contrast, the $\mathrm{Im}(\Delta\dot{G})$ feature in Fig, 5.16 shows good agreement with the expected exponential trends at all frequencies considered. Differently from the $\mathrm{Re}(\Delta\dot{G})$ feature, this one shows greater sensitivity to changes in corrosion exposure time as the considered excitation frequency increases.

As shown in Fig. 5.15 and 5.16, the slope of the fitted lines decreases over exposure time. Similar trends were obtained in [118, 123], this suggests that the behaviour of the atmospheric corrosion is a convergent process related to the chemical process [134]. The values of the equation coefficients that make up Eq. 5.4 are shown in Table 5.3.

From the results, it is important to highlight that the two features can allow the characterization of corrosion aging even with a single excitation frequency approach obviously respecting the feature limits shown. This turns out to be a great advantage with a view to a low-power consumption remote application.

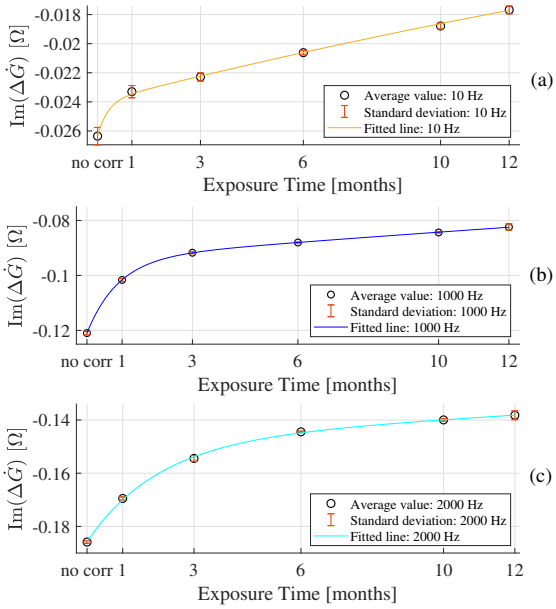

Figure 5.16: Measured average values, relative standard deviation and fitted lines of $\mathrm{Im}(\Delta\dot{G})$ for the coated samples [56].

5.3.2 Second scenario: Hidden corrosion

In the case of hidden corrosion, the depth of penetration of eddy currents plays a key role in the eventual detection and characterization of the corrosion state. In particular, considering the electrical conductivity, the magnetic permeability and the thickness of the analyzed samples, an appropriate set of excitation frequencies must be selected.

The electrical conductivity and relative magnetic permeability were considered equal to 4.68 MS/m and 60 respectively for the mild steel sample and 0.75 MS/m and 4 respectively for the corrosion layer [123].

Applying Eq. 2.1, it is possible to define that the applicable frequencies must be less than or equal to 100 Hz. For this reason, frequencies from 10 Hz to 100 Hz with the frequency resolution equal to 10 Hz will be shown in the representation of experimental results.

Fig. 5.17 shows the average trends obtained from the repeated tests on the different analyzed samples. In this case, it can be seen that the sensor allows the detection of the corrosion layer but does not allow to identify the accurate corrosion aging.

Table 5.3: Fitted values of the exponential coefficient [56].

			Excitation frequency [Hz]		
		Coefficient	10	1000	2000
Features	$\mathrm{Re}(\Delta\dot{G})$	A	-0.0182	-0.0097	N/A
		n	0.5852	0.7933	N/A
		q	0.4309	0.3893	N/A
	$\mathrm{Im}(\Delta\dot{G})$	A	0.0024	0.0211	0.0205
		n	0.4926	0.2382	0.3488
		q	-0.0262	-0.1211	-0.1864

On the other hand, it is possible to clearly note the non-corroded state, the corroded state distinguished by short-term exposure time (1, 3, 6 months) and long-term exposure time (10, 12 months). The results are related to the percentage of material loss that occurs for aged corrosion as shown in [134].

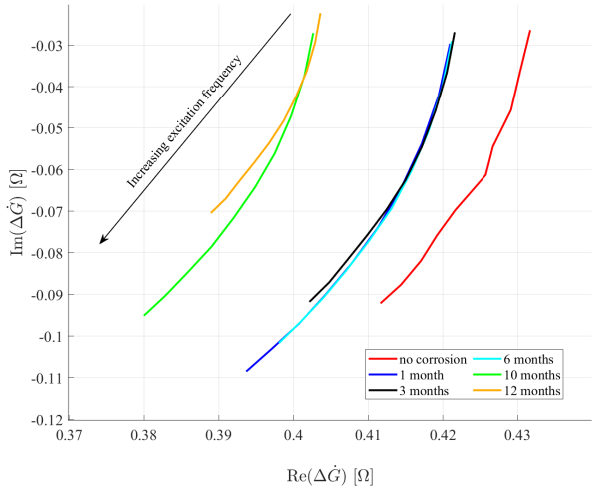

Figure 5.17: Average trends obtained using the pot-cored sensor for hidden corrosion on coated samples in all the considered analyzed cases [56].

In conclusion, in the case of hidden corrosion, the sensor shows a good ability to perform corrosion detection and to classify the various samples with corrosion aging classes (no corrosion, short-term and long-term exposure time).

5.3.3 Third scenario: Corrosion under insulating layer

With a view to applying the measurement system in real scenarios, the metrological performance of the pot-cored sensor were also analyzed in the detection and characterization of corrosion under insulating layer.

In particular, a commercial insulating layer applied for corrosion prevention [135] was placed on the corroded area of the considered samples. The insulating layer has a thickness equal to 2 mm and the pot-cored sensor was placed on its as shown in Fig. 5.13 (c).

As already performed in subsection 5.3.1 (superficial corrosions), the entire set of excitation frequencies (from 10 Hz to 2000 Hz) was investigated. Also in this case, the two measured quantities ($\mathrm{Re}(\Delta\dot{G})$, $\mathrm{Im}(\Delta\dot{G})$) are analyzed in order to define the best operating conditions.

Fig. 5.18 shows the average trends obtained from the repeated tests on the different samples analyzed. From the figure, it can be seen that the trends obtained are in line with the trends achieved in the case of superficial corrosion. In this case, however, it is possible to see that the performance has generally decreased from a qualitative point of view. Specifically, it is possible to note how the overlapping of the trends occurs at lower frequencies than in the case of superficial corrosion (as can be seen in the 1-3 months and 10-12 months cases).

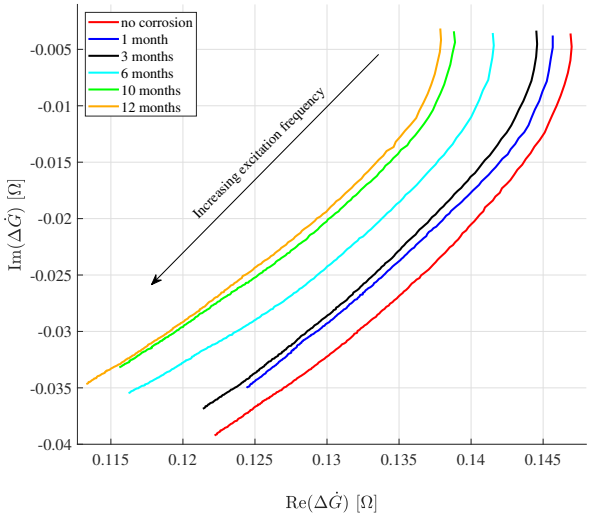

Figure 5.18: Average trends obtained using the pot-cored sensor for corrosion under an insulating layer on coated samples in all the considered analyzed cases [56].

Fig. 5.19 and Fig. 5.20 show the fitted lines of the mean values obtained by $\mathrm{Re}(\Delta\dot{G})$ and $\mathrm{Im}(\Delta\dot{G})$ at the minimum, the maximum and middle frequencies of the adopted range (10 Hz, 1000 Hz and 2000 Hz) as already done in subsection 5.3.1. The standard deviation of the values obtained is represented in the figures by means of vertical bars.

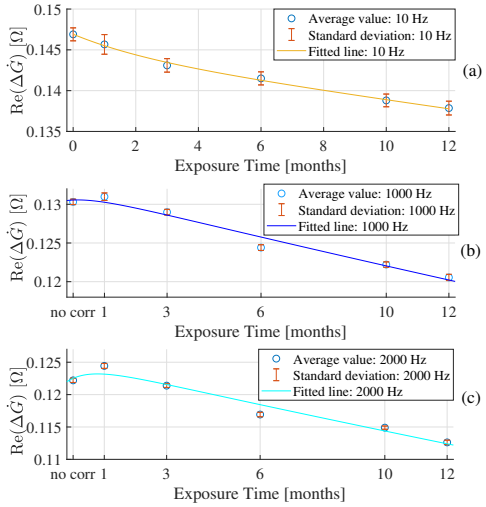

Figure 5.19: Measured average values, relative standard deviation and fitted lines of $\mathrm{Re}(\Delta\dot{G})$ in the case of corrosion under insulating layer [56].

By analyzing the feature $\mathrm{Re}(\Delta\dot{G})$ (see Fig. 5.19), it is possible to define that the feature can guarantee generally good performance. However, it is possible to observe that the measured amplitudes have decreased and the relative standard deviations have increased. As already mentioned, this phenomenon can be attributed to the increasing lift-off between the sensor and the analyzed sample. In addition, it is possible to observe particular overlaps related to the mean value added to the standard deviation between the uncorroded sample and the corrosion with 1 month of exposure time.

On the other hand, the feature $\mathrm{Im}(\Delta\dot{G})$ (see Fig. 5.20) shows no sensitivity under these conditions to corrosion states considered. The results are in fact very repeatable but not accurate; this feature seems not to be suitable for the characterization of the corrosion aging in this scenario. However, looking at the trends obtained in both 1000 Hz and 2000 Hz cases (Fig. 5.20 (b)-(c)), the feature can be adopted for corrosion detection because it shows a clear difference in terms of mean value and standard deviation.

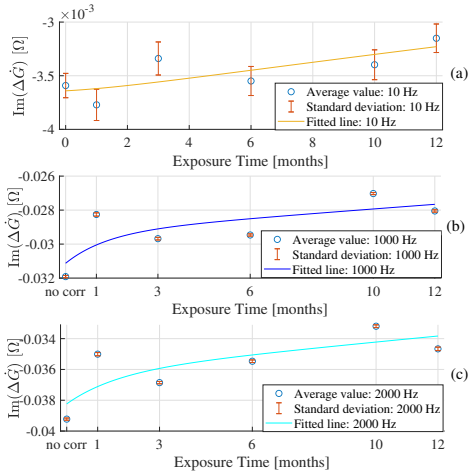

Figure 5.20: Measured average values, relative standard deviation and fitted lines of $\mathrm{Im}(\Delta\dot{G})$ in the case of corrosion under insulating layer [56].

In summary, in this section was possible to observe the performance of the proposed sensor in the case of measurements under insulating layer conditions. It was possible to see that the performance of the $\mathrm{Re}(\Delta\dot{G})$ feature allows to perform detection and characterization of different corrosion aging in all the considered set of excitation frequencies. However, this feature does not appear to be particularly sensitive in the case of short-term corrosion as in the case of 1 month exposure time.

On the contrary, the $\mathrm{Im}(\Delta\dot{G})$ feature does not turn out to be particularly sensitive under these conditions and thus does not allow the correct characterization of corrosion aging. It was possible to show, however, that as the excitation frequency increases (1000 Hz-2000 Hz cases), this feature allows detection between a corroded or uncorroded material. The general decrease in performance observed for this feature can be attributed to a clear decrease in magnetic coupling between the sensor and the sample under test due to the increase in lift-off distance.

5.4 Final discussion

This activity proposed the application of a pot-cored sensor in the detection and characterization of corrosion states [56]. In particular, numerical and experimental comparisons were carried out between the air-cored and the proposed pot-cored sensors in order to show the advantages obtainable through the use of the proposed

sensor.

From the numerical results, it was possible to define how the pot-cored sensor is able to generate higher surface eddy currents and concentrate higher magnetic flux on the analyzed sample. From an experimental point of view, it was shown that the proposed sensor can measure quantities of interest 3 to 8 times larger than a normal air-cored sensor, and its high sensitivity for low excitation frequencies was demonstrated. It has also been shown that the best metrological performance of the proposed sensor are achieved using lower excitation currents.

In a second phase, the pot-cored sensor was applied in several case studies related to surface, hidden and under-insulating layer corrosion. It was observed that the sensor performs very well in terms of characterizing corrosion aging in the case of superficial corrosions. For hidden corrosions, it was shown how the sensor is capable of detection and characterization by corrosion classes: short-term exposure time and long-term exposure time.

Finally, for under-layer corrosion, it was shown that the sensor has a decrease in its performance but is still able to detect (for both the analyzed features) and characterize (only for one analyzed feature) corrosion states.

It has been shown that the pot-cored sensor allows for good measurement repeatability which, combined with the clearly distinct trends of the measured quantities, promises good performance in terms of characterizing a corrosion state using a single-frequency or multi-frequency excitation measurement methods.

Furthermore, this sensor is promising for application in Structural Health Monitoring in relation to the detection and characterization of corrosion states due to the low-power consumption shown in this activity. Finally, the low power consumption required to achieve this performance has been demonstrated, making the sensor a good candidate for portable applications or remote measurement systems.

Chapter 6

Summary and conclusions

The research activity carried out in the field of Non-Destructive Testing, and specifically in the area of NDE 4.0, has led to the development of various solutions relating to thickness measurements, electrical and magnetic parameters of metallic materials, and detection and characterization of corrosion states using Eddy Current methods. The constant industrial demand for low cost, good accuracy and low measurement time monitoring and measurement systems has led to the need to develop experimental set-ups, models and measurement methods to meet these demands.

In particular, two different solutions for estimating the thickness of metallic materials were proposed in this activity.

The first solution focused on optimizing methods presented in the scientific literature in the past that guaranteed good measurement accuracies but did not meet industrial requirements in terms of analysis range and measurement time. This solution gave rise to three different methods which, combined, achieve the required metrological performance. The easy integration with the industrial world led to the patent realization on this activity. In particular, with reference to an accuracy level of 4% (level stated in reference papers), solutions were developed to achieve such accuracy over a wider thickness range (0.5 - 4 mm) and measurement times of less than 3 seconds.

The second proposed solution concerns the introduction of dimensional analysis into the NDT&E world for the first time. The strength of the proposed method lies in being able to reduce the number of variables that usually describe the problems being addressed. This method guaranteed excellent measurement performance in the case of simultaneous estimation of the thickness and electrical conductivity of metallic materials. In fact, relative errors of less than 4% were obtained for thickness estimation and errors of less than 2.5% for electrical conductivity estimation.

In addition, this method is promising in the case of numerical and artificial intelligence applications as the reduction in the number of variables involved can lead to an optimisation of analysis and processing times. Also in this case, considering the possible integration into the industrial framework, the methods was deposited for a patent request.

It is useful to make a few brief remarks regarding the applicability of the two measurement systems proposed. The measurement systems proposed in Chapter 3 and in Chapter 4 can be described as complementary and can be applied appropriately in relation to work contexts. For the measuring system proposed in Chapter 3, the final application could be addressed to a portable measurement system where the analysis of the metallic sample can be carried out on the field by means of experimental calibration. In contrast, the measurement system proposed in Chapter 4 requires an initial numerical simulation phase, so the system also needs the support of a numerical simulator. For this reason the measurement system is oriented within a production plant where very short measurement times are required.

Regarding the corrosion detection and characterization, a research activity related to the development of a pot-cored sensor was proposed. This sensor allowed good measurement repeatability and promised good performance in terms of characterizing a corrosion condition using a single-frequency or multi-frequency excitation measurement methods (as applied in the previous activities). Furthermore, the sensor was promising for remote application in Structural Health Monitoring due to the low-power consumption shown in Chapter 5.

Future developments concern the extension of the Buckingham's π theorem to structures composed by multiple layers, problems where the liftoff is unknown or analysis on magnetic materials. The goal is also to show the advantages using the Buckingham's π theorem on the other NDT&E usually applied in the industrial framework. In a following phase, the application of this methods could be also analyzed on anisotropic materials like composite materials.

Regarding the corrosion activity, future studies concern a useful data fusion strategy to exploit the potential of the two features proposed in the activity. In addition, a possible application of the electrical signatures (related to the features considered) can be addressed in the context of artificial intelligence algorithms.

Bibliography

[1] Albert Albers et al. “Procedure for Defining the System of Objectives in the Initial Phase of an Industry 4.0 Project Focusing on Intelligent Quality Control Systems”. In: *Procedia CIRP* 52 (2016). The Sixth International Conference on Changeable, Agile, Reconfigurable and Virtual Production (CARV2016), pp. 262–267. ISSN: 2212-8271. DOI: https://doi.org/10.1016/j.procir.2016.07.067.

[2] Stella Hrehova, Jozef Husár, and Lucia Knapčíková. “Production Quality Control Using the Industry 4.0 Concept”. In: *Future Access Enablers for Ubiquitous and Intelligent Infrastructures*. Ed. by Dragan Perakovic and Lucia Knapcikova. Cham: Springer International Publishing, 2021, pp. 193–202.

[3] Parkash Tambare et al. “Performance Measurement System and Quality Management in Data-Driven Industry 4.0: A Review”. In: *Sensors* 22.1 (2022). ISSN: 1424-8220. DOI: 10.3390/s22010224.

[4] Erhan Baran and Tulay Korkusuz Polat. “Classification of Industry 4.0 for Total Quality Management: A Review”. In: *Sustainability* 14.6 (2022). ISSN: 2071-1050. DOI: 10.3390/su14063329.

[5] Mridul Gupta et al. “Advances in applications of Non-Destructive Testing (NDT): A review”. In: *Advances in Materials and Processing Technologies* 8.2 (2022), pp. 2286–2307. DOI: 10.1080/2374068X.2021.1909332.

[6] Bing Wang et al. “Non-destructive testing and evaluation of composite materials/structures: A state-of-the-art review”. In: *Advances in Mechanical Engineering* 12.4 (2020), p. 1687814020913761. DOI: 10.1177/1687814020913761.

[7] G. Betta et al. “Thickness Measurements with Eddy Current and Ultrasonic Techniques”. In: *Sensors and Microsystems*. Ed. by G. et al. Di Francia. Cham: Springer International Publishing, 2020, pp. 387–394. ISBN: 978-3-030-37558-4. DOI: 10.1007/978-3-030-37558-4_58.

[8] Weiying Cheng. "Thickness Measurement of Metal Plates Using Swept-Frequency Eddy Current Testing and Impedance Normalization". In: *IEEE Sensors Journal* 17.14 (2017), pp. 4558–4569. DOI: 10.1109/JSEN.2017.2710356.

[9] Ermanno Pinotti and Ezio Puppin. "Simple Lock-In Technique for Thickness Measurement of Metallic Plates". In: *IEEE Transactions on Instrumentation and Measurement* 63.2 (2014), pp. 479–484. DOI: 10.1109/TIM.2013.2278999.

[10] S.B. Pankade, D.S. Khedekar, and C.L. Gogte. "The influence of heat treatments on electrical conductivity and corrosion performance of AA 7075-T6 aluminium alloy". In: *Procedia Manufacturing* 20 (2018). 2nd International Conference on Materials, Manufacturing and Design Engineering (iCMMD2017), 11-12 December 2017, MIT Aurangabad, Maharashtra, INDIA, pp. 53–58. ISSN: 2351-9789. DOI: https://doi.org/10.1016/j.promfg.2018.02.007.

[11] Eli Vandersluis and Comondore Ravindran. "Effects of solution heat treatment time on the as-quenched microstructure, hardness and electrical conductivity of B319 aluminum alloy". In: *Journal of Alloys and Compounds* 838 (2020), p. 155577. ISSN: 0925-8388. DOI: https://doi.org/10.1016/j.jallcom.2020.155577.

[12] A. Celzard et al. "Electrical conductivity of anthracites as a function of heat treatment temperature". In: *Carbon* 38.8 (2000), pp. 1207–1215. ISSN: 0008-6223. DOI: https://doi.org/10.1016/S0008-6223(99)00246-8.

[13] Koichi Mizukami, Yudai Watanabe, and Keiji Ogi. "Eddy current testing for estimation of anisotropic electrical conductivity of multidirectional carbon fiber reinforced plastic laminates". In: *Composites Part A: Applied Science and Manufacturing* 143 (2021), p. 106274. ISSN: 1359-835X. DOI: https://doi.org/10.1016/j.compositesa.2021.106274.

[14] Koichi Mizukami and Yudai Watanabe. "A simple inverse analysis method for eddy current-based measurement of through-thickness conductivity of carbon fiber composites". In: *Polymer Testing* 69 (2018), pp. 320–324. ISSN: 0142-9418. DOI: https://doi.org/10.1016/j.polymertesting.2018.05.043.

[15] Upeksha Chathurani Thibbotuwa, Ainhoa Cortés, and Andoni Irizar. "Small Ultrasound-Based Corrosion Sensor for Intraday Corrosion Rate Estimation". In: *Sensors* 22.21 (2022). ISSN: 1424-8220. DOI: 10.3390/s22218451.

[16] Song Ding et al. "Characterisation and evaluation of paint-coated marine corrosion in carbon steel using eddy current pulsed thermography". In: *NDT & E International* 130 (2022), p. 102678. ISSN: 0963-8695. DOI: https://doi.org/10.1016/j.ndteint.2022.102678.

[17] Yunze He et al. “Steel Corrosion Characterization Using Pulsed Eddy Current Systems”. In: *IEEE Sensors Journal* 12.6 (2012), pp. 2113–2120. DOI: 10.1109/JSEN.2012.2184280.

[18] Fei Yuan et al. “Investigation of DC Electromagnetic-Based Motion Induced Eddy Current on NDT for Crack Detection”. In: *IEEE Sensors Journal* 21.6 (2021), pp. 7449–7457. DOI: 10.1109/JSEN.2021.3049551.

[19] Andrea Bernieri et al. “Crack Shape Reconstruction in Eddy Current Testing Using Machine Learning Systems for Regression”. In: *IEEE Transactions on Instrumentation and Measurement* 57.9 (2008), pp. 1958–1968. DOI: 10.1109/TIM.2008.919011.

[20] Andrea Bernieri et al. “Crack Depth Estimation by Using a Multi-Frequency ECT Method”. In: *IEEE Transactions on Instrumentation and Measurement* 62.3 (2013), pp. 544–552. DOI: 10.1109/TIM.2012.2232471.

[21] Abdessalem Benammar, Redouane Drai, and Abderrezak Guessoum. “Detection of delamination defects in CFRP materials using ultrasonic signal processing”. In: *Ultrasonics* 48.8 (2008), pp. 731–738. ISSN: 0041-624X. DOI: https://doi.org/10.1016/j.ultras.2008.04.005.

[22] X. Lu, Q. Yi, and G. Y. Tian. “A Comparison of Feature Extraction Techniques for Delamination of CFRP Using Eddy Current Pulse-Compression Thermography”. In: *IEEE Sensors Journal* 20.20 (2020), pp. 12415–12422. DOI: 10.1109/JSEN.2020.2993154.

[23] Johannes Vrana et al. “Introduction to NDE 4.0”. In: *Handbook of Nondestructive Evaluation 4.0*. Ed. by Norbert Meyendorf et al. Cham: Springer International Publishing, 2022, pp. 3–30. ISBN: 978-3-030-73206-6. DOI: 10.1007/978-3-030-73206-6_43.

[24] Debejyo Chakraborty and Megan E. McGovern. “NDE 4.0: Smart NDE”. In: *2019 IEEE International Conference on Prognostics and Health Management (ICPHM)*. 2019, pp. 1–8. DOI: 10.1109/ICPHM.2019.8819429.

[25] Marija Bertovic and Iikka Virkkunen. “NDE 4.0: New Paradigm for the NDE Inspection Personnel”. In: *Handbook of Nondestructive Evaluation 4.0*. Ed. by Norbert Meyendorf et al. Cham: Springer International Publishing, 2022, pp. 239–269. ISBN: 978-3-030-73206-6. DOI: 10.1007/978-3-030-73206-6_9.

[26] Ali Bastas. “Comparing the probing systems of coordinate measurement machine: Scanning probe versus touch-trigger probe”. In: *Measurement* 156 (2020), p. 107604. ISSN: 0263-2241. DOI: https://doi.org/10.1016/j.measurement.2020.107604.

[27] Zhifeng Zhang et al. “A new laser displacement sensor based on triangulation for gauge real-time measurement”. In: *Optics & Laser Technology* 40.2 (2008), pp. 252–255. ISSN: 0030-3992. DOI: https://doi.org/10.1016/j.optlastec.2007.04.009.

[28] Young-Man Choi, Hongki Yoo, and Dongwoo Kang. “Large-area thickness measurement of transparent multi-layer films based on laser confocal reflection sensor”. In: *Measurement* 153 (2020), p. 107390. ISSN: 0263-2241. DOI: https://doi.org/10.1016/j.measurement.2019.107390.

[29] Renaldas Raisutis, Rymantas Kazys, and Liudas Mazeika. “Ultrasonic Thickness Measurement of Multilayered Aluminum Foam Precursor Material”. In: *IEEE Transactions on Instrumentation and Measurement* 57.12 (2008), pp. 2846–2855. DOI: 10.1109/TIM.2008.927208.

[30] Morana Mihaljević et al. “Measurement uncertainty evaluation of ultrasonic wall thickness measurement”. In: *Measurement* 137 (2019), pp. 179–188. ISSN: 0263-2241. DOI: https://doi.org/10.1016/j.measurement.2019.01.027.

[31] Jiannan Zhang et al. “Non-Destructive Evaluation of Coating Thickness Using Water Immersion Ultrasonic Testing”. In: *Coatings* 11.11 (2021). ISSN: 2079-6412. DOI: 10.3390/coatings11111421.

[32] W. Yin and A.J. Peyton. “Thickness measurement of non-magnetic plates using multi-frequency eddy current sensors”. In: *NDT & E International* 40.1 (2007), pp. 43–48. ISSN: 0963-8695. DOI: https://doi.org/10.1016/j.ndteint.2006.07.009.

[33] Wuliang Yin and Kai Xu. “A Novel Triple-Coil Electromagnetic Sensor for Thickness Measurement Immune to Lift-Off Variations”. In: *IEEE Transactions on Instrumentation and Measurement* 65.1 (2016), pp. 164–169. DOI: 10.1109/TIM.2015.2479106.

[34] Mingyang Lu et al. “A Novel Compensation Algorithm for Thickness Measurement Immune to Lift-Off Variations Using Eddy Current Method”. In: *IEEE Transactions on Instrumentation and Measurement* 65.12 (2016), pp. 2773–2779. DOI: 10.1109/TIM.2016.2600918.

[35] Mengbao Fan et al. “Pulsed eddy current thickness measurement using phase features immune to liftoff effect”. In: *NDT & E International* 86 (2017), pp. 123–131. ISSN: 0963-8695. DOI: https://doi.org/10.1016/j.ndteint.2016.12.003.

[36] Haowen Wang et al. “A Novel Pulsed Eddy Current Criterion for Non-Ferromagnetic Metal Thickness Quantifications under Large Liftoff”. In: *Sensors* 22.2 (2022). ISSN: 1424-8220. DOI: 10.3390/s22020614. URL: https://www.mdpi.com/1424-8220/22/2/614.

[37] Nalika Ulapane et al. "Surface Representation of Pulsed Eddy Current Sensor Signals for Improved Ferromagnetic Material Thickness Quantification". In: *IEEE Sensors Journal* 21.4 (2021), pp. 5413–5422. DOI: 10.1109/JSEN.2020.3034571.

[38] Giulia Di Capua et al. "Optimization of an ECT-based method for the thickness measurement of metallic plates". In: *2022 IEEE 9th International Workshop on Metrology for AeroSpace (MetroAeroSpace)*. 2022, pp. 368–373. DOI: 10.1109/MetroAeroSpace54187.2022.9856384.

[39] Alessandro Sardellitti et al. "An Eddy-Current Testing Method for Measuring the Thickness of Metallic Plates". In: *IEEE Transactions on Instrumentation and Measurement* 72 (2023), pp. 1–10. DOI: 10.1109/TIM.2023.3269781.

[40] Alessandro Sardellitti et al. "A Fast ECT Measurement Method for the Thickness of Metallic Plates". In: *IEEE Transactions on Instrumentation and Measurement* 71 (2022), pp. 1–12. DOI: 10.1109/TIM.2022.3188029.

[41] Giulia Di Capua et al. ""Thickness measuring device using eddy currents and corresponding measurement method". In: PA099929EP01. 2023. URL: Patent%20pending%20to%20the%20European%20Patent%20Office.

[42] Peipei Zhu et al. "A novel machine learning model for eddy current testing with uncertainty". In: *NDT & E International* 101 (2019), pp. 104–112. ISSN: 0963-8695. DOI: https://doi.org/10.1016/j.ndteint.2018.09.010.

[43] Matthew Belding, Alireza Enshaeian, and Piervincenzo Rizzo. "Nondestructive rail neutral temperature estimation based on low-frequency vibrations and machine learning". In: *NDT & E International* 137 (2023), p. 102840. ISSN: 0963-8695. DOI: https://doi.org/10.1016/j.ndteint.2023.102840.

[44] Seongcheol Ryu, Seong-Hyun Park, and Kyung-Young Jhang. "Plastic properties estimation of aluminum alloys using machine learning of ultrasonic and eddy current data". In: *NDT & E International* 137 (2023), p. 102857. ISSN: 0963-8695. DOI: https://doi.org/10.1016/j.ndteint.2023.102857.

[45] John Cecil Gibbings. *Dimensional analysis*. Springer Science & Business Media, 2011.

[46] Howard Georgi. "Generalized dimensional analysis". In: *Physics Letters B* 298.1 (1993), pp. 187–189. ISSN: 0370-2693. DOI: https://doi.org/10.1016/0370-2693(93)91728-6.

[47] Pengfei Hu and Chia-kan Chang. "Research on optimize application of Buckingham Pi theorem to wind tunnel test and its aerodynamic simulation verification". In: *Journal of Physics: Conference Series* 1507.8 (2020), p. 082047. DOI: 10.1088/1742-6596/1507/8/082047.

[48] Raymond Chong Ong Tang et al. “Review on design factors of microbial fuel cells using Buckingham’s Pi Theorem”. In: *Renewable and Sustainable Energy Reviews* 130 (2020), p. 109878. ISSN: 1364-0321. DOI: https://doi.org/10.1016/j.rser.2020.109878. URL: https://www.sciencedirect.com/science/article/pii/S1364032120301714.

[49] G. Maheedhara Reddy and V. Diwakar Reddy. “Theoretical Investigations on Dimensional Analysis of Ball Bearing Parameters by Using Buckingham Pi-Theorem”. In: *Procedia Engineering* 97 (2014). ”12th Global Congress on Manufacturing and Management” GCMM - 2014, pp. 1305–1311. ISSN: 1877-7058. DOI: https://doi.org/10.1016/j.proeng.2014.12.410.

[50] W.D. Curtis, J.David Logan, and W.A. Parker. “Dimensional analysis and the pi theorem”. In: *Linear Algebra and its Applications* 47 (1982), pp. 117–126. ISSN: 0024-3795. DOI: https://doi.org/10.1016/0024-3795(82)90229-4. URL: https://www.sciencedirect.com/science/article/pii/0024379582902294.

[51] E. Buckingham. “On Physically Similar Systems; Illustrations of the Use of Dimensional Equations”. In: *Phys. Rev.* 4 (4 1914), pp. 345–376. DOI: 10.1103/PhysRev.4.345. URL: https://link.aps.org/doi/10.1103/PhysRev.4.345.

[52] Antonello Tamburrino et al. “Old but not obsolete: Dimensional analysis in nondestructive testing and evaluation”. In: *NDT & E International* (2023), p. 102977. ISSN: 0963-8695. DOI: https://doi.org/10.1016/j.ndteint.2023.102977.

[53] Antonello Tamburrino et al. “Application of dimensional analysis to ECT in the era of NDE 4.0”. In: *International Journal of Applied Electromagnetics and Mechanics, accepted for publication* (2023).

[54] Alessandro Sardellitti et al. “Metrological characterization of an ECT method for thickness estimation based on dimensional analysis”. In: *2023 IEEE 10th International Workshop on Metrology for AeroSpace (MetroAeroSpace)*. 2023, pp. 441–446. DOI: 10.1109/MetroAeroSpace57412.2023.10189992.

[55] Antonello Tamburrino et al. ““Eddy-current multi-parameter measurement device and corresponding measurement method”. In: PA101889IT01. 2023. URL: Patent%20pending%20to%20the%20Italian%20Patent%20Office.

[56] Alessandro Sardellitti et al. “An optimized Eddy Current sensor for corrosion detection and characterization”. In: *IEEE Transactions on Instrumentation and Measurement, submitted for publication* (2023).

[57] U.M. Angst. “Challenges and opportunities in corrosion of steel in concrete”. In: *Materials and Structures volume* 51.4 (2018). DOI: https://doi.org/10.1617/s11527-017-1131-6.

[58] Dongming Feng and Maria Q. Feng. "Computer vision for SHM of civil infrastructure: From dynamic response measurement to damage detection – A review". In: *Engineering Structures* 156 (2018), pp. 105–117. ISSN: 0141-0296. DOI: https://doi.org/10.1016/j.engstruct.2017.11.018.

[59] Francisco J. Pallarés et al. "Structural health monitoring (SHM) and Nondestructive testing (NDT) of slender masonry structures: A practical review". In: *Construction and Building Materials* 297 (2021), p. 123768. ISSN: 0950-0618. DOI: https://doi.org/10.1016/j.conbuildmat.2021.123768.

[60] Zenghua Liu et al. "Development of a Bidirectional-Excitation Eddy-Current Sensor With Magnetic Shielding: Detection of Subsurface Defects in Stainless Steel". In: *IEEE Sensors Journal* 18.15 (2018), pp. 6203–6216. DOI: 10.1109/JSEN.2018.2844957.

[61] Grzegorz Tytko. "Measurement of multilayered conductive discs using eddy current method". In: *Measurement* 204 (2022), p. 112053. ISSN: 0263-2241. DOI: https://doi.org/10.1016/j.measurement.2022.112053.

[62] Grzegorz Tytko. "Eddy Current Testing of Conductive Coatings Using a Pot-Core Sensor". In: *Sensors* 23.2 (2023). DOI: https://doi.org/10.3390/s23021042.

[63] Binfeng Yang et al. "Magnetic field shielding technique for pulsed remote field eddy current inspection of planar conductors". In: *NDT & E International* 90 (2017), pp. 48–54. ISSN: 0963-8695. DOI: https://doi.org/10.1016/j.ndteint.2017.05.001.

[64] K.O. Kim. "Effects of manufacturing defects on the device failure rate". In: *Journal Korean Stat. Soc.* 43 (2022), pp. 481–495. DOI: 10.1016/j.jkss.2013.02.003.

[65] Wei Lin, Pan Li, and Xiongyao Xie. "A Novel Detection and Assessment Method for Operational Defects of Pipe Jacking Tunnel Based on 3D Longitudinal Deformation Curve: A Case Study". In: *Sensors* 22.19 (2022). ISSN: 1424-8220. DOI: 10.3390/s22197648.

[66] Anton du Plessis and William P. Boshoff. "A review of X-ray computed tomography of concrete and asphalt construction materials". In: *Construction and Building Materials* 199 (2019), pp. 637–651. ISSN: 0950-0618. DOI: https://doi.org/10.1016/j.conbuildmat.2018.12.049.

[67] Johann Kastner and Christoph Heinzl. "X-ray Computed Tomography for Non-destructive Testing and Materials Characterization". In: *Integrated Imaging and Vision Techniques for Industrial Inspection: Advances and Applications*. Ed. by Zheng Liu et al. Springer London, 2015. ISBN: 978-1-4471-6741-9. DOI: 10.1007/978-1-4471-6741-9_8.

[68] *UNI ISO 18434-1:2011, Machine condition monitoring and diagnostics - Thermography - Part 1: General procedures, Available online (accessed on 21 September 2023).* URL: https://store.uni.com/uni-iso-18434-1-2011.

[69] *UNI EN 16714-2:2016, Non-destructive testing - Thermographic testing - Part 2: Instrumentation, Available online (accessed on 21 September 2023).* URL: https://store.uni.com/uni-en-16714-2-2016.

[70] *EN 13018:201, Non-destructive testing - Visual testing - General principles, Available online (accessed on 21 September 2023).* URL: https://standards.iteh.ai/catalog/standards/cen/8c59398f-2658-4799-b9c5-2e529c1102e6/en-13018-2016.

[71] *ISO 3452-1:2021, Non-destructive testing - Penetrant testing - Part 1: General principles, Available online (accessed on 21 September 2023).* URL: https://store.uni.com/iso-3452-1-2021.

[72] *Deep penetrating eddy currents and probes.* URL: https://www.ndt.net/search/docs.php3?id=3740.

[73] Wei Kent (Hsin-Yu), Qiu Chang-Hua, and Primrose Ken. "Super-sensing technology: industrial applications and future challenges of electrical tomography". In: *Philosophical transactions of the royal society A* (2016). DOI: 10.1098/rsta.2015.0328.

[74] M. Wang, T.F. Jones, and R.A. Williams. "Visualization of Asymmetric Solids Distribution in Horizontal Swirling Flows Using Electrical Resistance Tomography". In: *Chemical Engineering Research and Design* 81.8 (2003). Particle Technology, pp. 854–861. ISSN: 0263-8762. DOI: https://doi.org/10.1205/026387603322482095.

[75] R. Giguère et al. "Characterization of slurry flow regime transitions by ERT". In: *Chemical Engineering Research and Design* 86.9 (2008), pp. 989–996. ISSN: 0263-8762. DOI: https://doi.org/10.1016/j.cherd.2008.03.014.

[76] Lionel Pullum et al. "High concentration suspension pumping". In: *Minerals Engineering* 19.5 (2006), pp. 471–477. ISSN: 0892-6875. DOI: https://doi.org/10.1016/j.mineng.2005.08.010.

[77] T.L. Rodgers and A. Kowalski. "An electrical resistance tomography method for determining mixing in batch addition with a level change". In: *Chemical Engineering Research and Design* 88.2 (2010), pp. 204–212. ISSN: 0263-8762. DOI: https://doi.org/10.1016/j.cherd.2009.08.003.

[78] Wisarn Yenjaichon et al. "In-line jet mixing of liquid–pulp–fibre suspensions: Effect of concentration and velocities". In: *Chemical Engineering Science* 75 (2012), pp. 167–176. ISSN: 0009-2509. DOI: https://doi.org/10.1016/j.ces.2012.03.012.

[79] Wisarn Yenjaichon et al. "Characterisation of gas mixing in water and pulp-suspension flow based on electrical resistance tomography". In: *Chemical Engineering Journal* 214 (2013), pp. 285–297. ISSN: 1385-8947. DOI: https://doi.org/10.1016/j.cej.2012.10.057.

[80] Artur J Jaworski and Tomasz Dyakowski. "Application of electrical capacitance tomography for measurement of gas-solids flow characteristics in a pneumatic conveying system". In: *Measurement Science and Technology* 12.8 (2001), p. 1109. DOI: 10.1088/0957-0233/12/8/317.

[81] Meng Sun et al. "Mass flow measurement of pneumatically conveyed solids using electrical capacitance tomography". In: *Measurement Science and Technology* 19.4 (2008), p. 045503. DOI: 10.1088/0957-0233/19/4/045503.

[82] Lamb Horace. "On waves in an elastic plate". In: *Proceeding of the Royal Society A* 19.4 (1917), p. 045503. DOI: 10.1098/rspa.1917.0008.

[83] CV Dodd and WE Deeds. "Analytical solutions to eddy-current probe-coil problems". In: *Journal of applied physics* 39.6 (1968), pp. 2829–2838.

[84] *EN 485-4:2000, Available online (accessed on 4 July 2022)*. URL: https://infostore.saiglobal.com/en-gb/standards/ds-en-485-4-2000-462686%5C_saig%5C_ds%5C_ds%5C_1042214/.

[85] Andrea Bernieri et al. "Multifrequency Excitation and Support Vector Machine Regressor for ECT Defect Characterization". In: *IEEE Transactions on Instrumentation and Measurement* 63.5 (2014), pp. 1272–1280. DOI: 10.1109/TIM.2013.2292326.

[86] Andrea Bernieri et al. "Multi-frequency Eddy Current Testing using a GMR based instrument". In: *International Journal of Applied Electromagnetics and Mechanics* 39.1-4 (2012), pp. 355–362. DOI: 10.3233/JAE-2012-1482.

[87] M.R. Eslahchi, Mehdi Dehghan, and Sanaz Amani. "The third and fourth kinds of Chebyshev polynomials and best uniform approximation". In: *Mathematical and Computer Modelling* 55.5 (2012), pp. 1746–1762. ISSN: 0895-7177. DOI: https://doi.org/10.1016/j.mcm.2011.11.023.

[88] Hiroshi Akima. "A New Method of Interpolation and Smooth Curve Fitting Based on Local Procedures". In: *J. ACM* 17.4 (1970), pp. 589–602. ISSN: 0004-5411. DOI: 10.1145/321607.321609.

[89] Hiroshi Akima. "A Method of Bivariate Interpolation and Smooth Surface Fitting Based on Local Procedures". In: *Commun. ACM* 17.1 (1974), pp. 18–20. ISSN: 0001-0782. DOI: 10.1145/360767.360779.

[90] F. N. Fritsch and R. E. Carlson. "Monotone Piecewise Cubic Interpolation". In: *SIAM Journal on Numerical Analysis* 17.2 (1980), pp. 238–246. ISSN: 00361429. URL: http://www.jstor.org/stable/2156610 (visited on 09/01/2023).

[91] John Cecil Gibbings. *Dimensional analysis*. Springer Science & Business Media, 2011.

[92] Howard Georgi. "Generalized dimensional analysis". In: *Physics Letters B* 298.1 (1993), pp. 187–189. ISSN: 0370-2693. DOI: https://doi.org/10.1016/0370-2693(93)91728-6.

[93] Giuseppina Ciulla, Antonino D'Amico, and Valerio Lo Brano. "Evaluation of building heating loads with dimensional analysis: Application of the Buckingham π theorem". In: *Energy and Buildings* 154 (2017), pp. 479–490. ISSN: 0378-7788. DOI: https://doi.org/10.1016/j.enbuild.2017.08.043. URL: https://www.sciencedirect.com/science/article/pii/S0378778817318157.

[94] H.O. Fatoyinbo. "8 - Microfluidic devices for cell manipulation". In: Woodhead Publishing Series in Biomaterials (2013). Ed. by Xiujun (James) Li and Yu Zhou, pp. 283–350. DOI: https://doi.org/10.1533/9780857097040.3.283. URL: https://www.sciencedirect.com/science/article/pii/B9780857096975500086.

[95] Pengfei Hu and Chia-kan Chang. "Research on optimize application of Buckingham Pi theorem to wind tunnel test and its aerodynamic simulation verification". In: *Journal of Physics: Conference Series* 1507.8 (2020), p. 082047. DOI: 10.1088/1742-6596/1507/8/082047.

[96] Luigi Russo et al. "Application of Buckingham π theorem for scaling-up oriented fast modelling of Proton Exchange Membrane Fuel Cell impedance". In: *Journal of Power Sources* 353 (2017), pp. 277–286. ISSN: 0378-7753. DOI: https://doi.org/10.1016/j.jpowsour.2017.03.116.

[97] Ravindranadh Bobbili, V. Madhu, and A.K. Gogia. "Modelling and analysis of material removal rate and surface roughness in wire-cut EDM of armour materials". In: *Engineering Science and Technology, an International Journal* 18.4 (2015), pp. 664–668. ISSN: 2215-0986. DOI: https://doi.org/10.1016/j.jestch.2015.03.014.

[98] Pu Huang et al. "An Eddy Current Testing Method for Thickness and Conductivity Measurement of Non-magnetic Material". In: *IEEE Sensors Journal* (2022), pp. 1–1. DOI: 10.1109/JSEN.2022.3151365.

[99] Chun-Yeon Lin, Yi-Chin Wu, and Megan Teng. "Development of a Magnetic Eddy-Current Sensing System For Simultaneous Estimation of Electrical Conductivity and Thickness in Non-Ferrous Metal Plates". In: *IEEE/ASME Transactions on Mechatronics* (2022), pp. 1–12. DOI: 10.1109/TMECH.2022.3199821.

[100] Kok-Meng Lee et al. "Coupled Parametric Effects on Magnetic Fields of Eddy-Current Induced in Non-Ferrous Metal Plate for Simultaneous Estimation of Geometrical Parameters and Electrical Conductivity". In: *IEEE Transactions on Magnetics* 53.10 (2017), pp. 1–9. DOI: 10.1109/TMAG.2017.2715831.

[101] Cheng-Chi Tai, James H. Rose, and John C. Moulder. "Thickness and conductivity of metallic layers from pulsed eddy-current measurements". In: *Review of Scientific Instruments* 67.11 (1996), pp. 3965–3972. DOI: 10.1063/1.1147300.

[102] Weiying Cheng and Ichiro Komura. "Simulation of Transient Eddy-Current Measurement for the Characterization of Depth and Conductivity of a Conductive Plate". In: *IEEE Transactions on Magnetics* 44.11 (2008), pp. 3281–3284. DOI: 10.1109/TMAG.2008.2001613.

[103] Mingyang Lu et al. "Determination of the Magnetic Permeability, Electrical Conductivity, and Thickness of Ferrite Metallic Plates Using a Multifrequency Electromagnetic Sensing System". In: *IEEE Transactions on Industrial Informatics* 15.7 (2019), pp. 4111–4119. DOI: 10.1109/TII.2018.2885406.

[104] J.C. Benedyk. "3 - Aluminum alloys for lightweight automotive structures". In: *Materials, Design and Manufacturing for Lightweight Vehicles*. Ed. by P.K. Mallick. Woodhead Publishing Series in Composites Science and Engineering. Woodhead Publishing, 2010, pp. 79–113. ISBN: 978-1-84569-463-0. DOI: https://doi.org/10.1533/9781845697822.1.79.

[105] Manabu Nakai and Takehiko Eto. "New aspect of development of high strength aluminum alloys for aerospace applications". In: *Materials Science and Engineering: A* 285.1 (2000), pp. 62–68. ISSN: 0921-5093. DOI: https://doi.org/10.1016/S0921-5093(00)00667-5.

[106] *Gwinstek Impedance Analyzer. Available on-line (accessed on 21 September 2023)*. URL: https://www.gwinstek.com/en-global/products/downloadSeriesDownNew/10096/742e.

[107] *Keysight Impedance Analyzer. Available on-line (accessed on 21 September 2023)*. URL: https://www.keysight.com/us/en/product/E4980A/precision-lcr-meter-20-hz-2-mhz.html.

[108] Blossom Treesa Bastian et al. "Visual inspection and characterization of external corrosion in pipelines using deep neural network". In: *NDT & E International* 107 (2019), p. 102134. ISSN: 0963-8695. DOI: https://doi.org/10.1016/j.ndteint.2019.102134.

[109] Luciane Soares et al. “A Visual Inspection Proposal to Identify Corrosion Levels in Marine Vessels Using a Deep Neural Network”. In: *2021 Latin American Robotics Symposium (LARS), 2021 Brazilian Symposium on Robotics (SBR), and 2021 Workshop on Robotics in Education (WRE)*. 2021, pp. 222–227. DOI: 10.1109/LARS/SBR/WRE54079.2021.9605400.

[110] F. El-Taib Heakal, S.A. Rizk, and A.E. Elkholy. “Characterization of newly synthesized pyrimidine derivatives for corrosion inhibition as inferred from computational chemical analysis”. In: *Journal of Molecular Structure* 1152 (2018), pp. 328–336. ISSN: 0022-2860. DOI: https://doi.org/10.1016/j.molstruc.2017.09.079.

[111] Jian Zhang et al. “Chemical analysis of the initial corrosion layer on pipeline steels in simulated CO2-enhanced oil recovery brines”. In: *Corrosion Science* 65 (2012), pp. 397–404. ISSN: 0010-938X. DOI: https://doi.org/10.1016/j.corsci.2012.08.045.

[112] A. Nishikata, Y. Ichihara, and T. Tsuru. “An application of electrochemical impedance spectroscopy to atmospheric corrosion study”. In: *Corrosion Science* 37 (1995), pp. 897–911. DOI: 10.1016/0010-938X(95)00002-2.

[113] J. Wang et al. “The corrosion mechanisms of carbon steel and weathering steel in SO 2 polluted atmospheres”. In: *Materials Chemistry and Physics - MATER CHEM PHYS* 47 (1997), pp. 1–8. DOI: 10.1016/S0254-0584(97)80019-3.

[114] Yuantai Ma, Ying Li, and Fuhui Wang. “Corrosion of low carbon steel in atmospheric environments of different chloride content”. In: *Corrosion Science - CORROS SCI* 51 (2009), pp. 997–1006. DOI: 10.1016/j.corsci.2009.02.009.

[115] G. Salvago, G. Bollini, and P. Cavalotti. “Electrochemical Evaluation of Localized Corrosion Probability in Stainless Steel”. In: *Materials Science Forum - MATER SCI FORUM* 289-292 (1998), pp. 933–954. DOI: 10.4028/www.scientific.net/MSF.289-292.933.

[116] G. Dutta et al. “Digitalization priorities of quality control processes for SMEs: a conceptual study in perspective of Industry 4.0 adoption”. In: *Journal of Intelligent Manufacturing* 32 (2021). DOI: https://doi.org/10.1007/s10845-021-01783-2.

[117] Radu Godina and João C. O. Matias. “Quality Control in the Context of Industry 4.0”. In: *Industrial Engineering and Operations Management II*. Ed. by João Reis, Sandra Pinelas, and Nuno Melão. Cham: Springer International Publishing, 2019, pp. 177–187. ISBN: 978-3-030-14973-4. DOI: https://doi.org/10.1007/978-3-030-14973-4_17.

[118] Hong Zhang et al. “Evaluation of Atmospheric Corrosion on Coated Steel Using K -Band Sweep Frequency Microwave Imaging”. In: *IEEE Sensors Journal* 16.9 (2016), pp. 3025–3033. DOI: 10.1109/JSEN.2016.2522983.

[119] Ruslee Sutthaweekul and Gui Y. Tian. “Steel Corrosion Stages Characterization Using Open-Ended Rectangular Waveguide Probe”. In: *IEEE Sensors Journal* 18.3 (2018), pp. 1054–1062. DOI: 10.1109/JSEN.2017.2775521.

[120] Song Ding et al. “Characterisation and evaluation of paint-coated marine corrosion in carbon steel using eddy current pulsed thermography”. In: *NDT & E International* 130 (2022), p. 102678. ISSN: 0963-8695. DOI: https://doi.org/10.1016/j.ndteint.2022.102678.

[121] Ruizhen Yang et al. “Through coating imaging and nondestructive visualization evaluation of early marine corrosion using electromagnetic induction thermography”. In: *Ocean Engineering* 147 (2018), pp. 277–288. ISSN: 0029-8018. DOI: https://doi.org/10.1016/j.oceaneng.2017.09.023.

[122] Adi Mahmud Jaya Marindra and Gui Yun Tian. “Chipless RFID sensor for corrosion characterization based on frequency selective surface and feature fusion”. In: *Smart Materials and Structures* 29.12 (2020), p. 125010. DOI: 10.1088/1361-665X/abbff4.

[123] Yunze He et al. “Steel Corrosion Characterization Using Pulsed Eddy Current Systems”. In: *IEEE Sensors Journal* 12.6 (2012), pp. 2113–2120. DOI: 10.1109/JSEN.2012.2184280.

[124] Yong Li et al. “Pulse-modulation eddy current inspection of subsurface corrosion in conductive structures”. In: *NDT & E International* 79 (2016), pp. 142–149. ISSN: 0963-8695. DOI: https://doi.org/10.1016/j.ndteint.2016.02.001.

[125] Yong Li et al. “Pulse-modulation eddy current probes for imaging of external corrosion in nonmagnetic pipes”. In: *NDT & E International* 88 (2017), pp. 51–58. ISSN: 0963-8695. DOI: https://doi.org/10.1016/j.ndteint.2017.02.009.

[126] Bei Yan et al. “Recognition and evaluation of corrosion profile via pulse-modulation eddy current inspection in conjunction with improved Canny algorithm”. In: *NDT & E International* 106 (2019), pp. 18–28. ISSN: 0963-8695. DOI: https://doi.org/10.1016/j.ndteint.2019.05.007.

[127] Manoel M. Silva et al. “Intelligent embedded system for decision support in pulsed eddy current corrosion detection using Extreme Learning Machine”. In: *Measurement* 185 (2021), p. 110069. ISSN: 0263-2241. DOI: https://doi.org/10.1016/j.measurement.2021.110069.

[128] Rukhshinda Wasif et al. “Development of Permanently Installed Magnetic Eddy Current Sensor for Corrosion Monitoring of Ferromagnetic Pipelines”. In: *Applied Sciences* 12.3 (2022). ISSN: 2076-3417. DOI: 10.3390/app12031037.

[129] Dario J. Pasadas et al. "ECT in composite materials using double excitation coils and resonant excitation/sensing circuits". In: *Measurement* 161 (2020), p. 107859. ISSN: 0263-2241. DOI: https://doi.org/10.1016/j.measurement.2020.107859.

[130] Deqiang Zhou et al. "Influence of metallic shields on pulsed eddy current sensor for ferromagnetic materials defect detection". In: *Sensors and Actuators A: Physical* 248 (2016), pp. 162–172. ISSN: 0924-4247. DOI: https://doi.org/10.1016/j.sna.2016.07.029.

[131] *Ferrite core geometrical, electrical and magnetic characteristics, Available online (accessed on 4 August 2023).* URL: Available:%20https://www.tdk-electronics.tdk.com/inf/80/db/fer/p%5C_22%5C_13.pdf.

[132] *TMR2905 Ultra High Sensitivity TMR linear sensor, Available online (accessed on 4 August 2023).* URL: Available:%20http://www.dowaytech.com/en/1401.html.

[133] A. Bernieri et al. "Characterization of a TMR Sensor for EC-NDT Applications". In: *Sensors*. Ed. by Bruno Andò et al. Cham: Springer International Publishing, 2019, pp. 229–236. ISBN: 978-3-030-04324-7.

[134] R. E. Melchers. "Transition from Marine Immersion to Coastal Atmospheric Corrosion for Structural Steels". In: *CORROSION* 63 (2007), pp. 500–514. DOI: https://doi.org/10.5006/1.3278401.

[135] *Ancorro VE for corrosion prevention & sealing (accessed on 4 July 2022).* URL: Available:%20https://www.ancorro.com/ANCORRO%5C_VE%5C_Stretch%5C_22.

[136] J. Blitz and G. Simpson. *Ultrasonic Methods of Non-destructive Testing*. Non-Destructive Evaluation Series. Springer Netherlands, 1995. URL: https://books.google.it/books?id=d3WWect9zQEC.

[137] W. Lester and Jr. Schmerr. *Fundamentals of Ultrasonic Nondestructive Evaluation*. Springer Series in Measurement Science and Technology. Springer Cham, 2016. DOI: https://doi.org/10.1007/978-3-319-30463-2.

[138] David J. Penney, James H. Sullivan, and David A. Worsley. "Investigation into the effects of metallic coating thickness on the corrosion properties of Zn–Al alloy galvanising coatings". In: *Corrosion Science* 49.3 (2007), pp. 1321–1339. ISSN: 0010-938X. DOI: https://doi.org/10.1016/j.corsci.2006.07.006.

[139] Y. Zhao et al. "Simultaneous determination of the coating thickness and its longitudinal velocity by ultrasonic nondestructive method". In: *NDT & E International* 43.7 (2010), pp. 579–585. ISSN: 0963-8695. DOI: https://doi.org/10.1016/j.ndteint.2010.06.001.

[140] Jean-Pierre Fouque et al. “Waves in Layered Media”. In: *Wave Propagation and Time Reversal in Randomly Layered Media*. New York, NY: Springer New York, 2007, pp. 33–60. DOI: 10.1007/978-0-387-49808-9_3.

Appendices

Appendix A

Buckingham's π theorem in Ultrasonic Non-Destructive Testing

A.1 Introduction and general mathematical setting

Ultrasonic Non Destructive Testing is a set of methods which exploits high frequency mechanical waves to reveal the presence of material flaws or to measure the thickness of samples under test. The frequency employed in testing are typically in the range 500 kHz – 20 MHz [82, 136]. In this note, we describe an example of application of Buckingham's π theorem to this kind of problems.

From a general perspective the propagation of ultrasonic waves is modelled by the wave equation in fluid and by the Navier equation in solid. Specifically, let us consider an ideal compressible fluid (Ideal compressible fluid can be considered as an elastic body the internal energy of which depends only on the mass density of the body. Therefore, the variational principles formulated for elastic bodies are valid for compressible fluids as well), the pressure field is governed by the following PDE [137].

$$\nabla^2 p = \frac{1}{c^2}\frac{\partial^2 p}{\partial t^2} + f = 0 \tag{A.1}$$

where p is the pressure, c the speed of sound in fluid and f is a scalar body force term. In solids, let $\mathbf{u}$ the displacement vector, the governing equation is [137].

$$\mu\nabla^2\mathbf{p} + (\lambda+\mu)\nabla(\nabla\cdot\mathbf{u}) + \mathbf{f} = \rho\frac{\partial^2\mathbf{u}}{\partial t^2}, \tag{A.2}$$

where λ, μ are the Lame constants, ρ the solid density and $\mathbf{f}$ is the body force vector. The above equation is valid under the hypothesis of small displacement and velocity gradient. It is worth noting that it is possible to substitute the two Lame constants with the Young's modulus E and the Poisson's ratio ν by the following relationships

$$\lambda = \frac{E\nu}{(1+\nu)(1-2\nu)}) \tag{A.3}$$

$$\mu = \frac{E}{2(1+\nu)} \tag{A.4}$$

A.2 Simultaneous estimation of coating thickness and longitudinal velocity

In this Section, a specific application of ultrasonic non destructive testing is presented as a possible target problem for the application of Buckingham's theorem. Specifically, the goal is to measure the thickness of surface coatings. This feature plays an important role since coating thickness affects various properties of the coating such as corrosion protection [138]. Traditionally, the thickness is estimated by the time-of-flight method. This method is suitable for sufficiently thick coating, in order to guarantee that echoes from the front and back surfaces of the material are well-separated.

Recently, new techniques are introduced to overcome this problem. In particular, a promising technique consists in measuring the reflection coefficient R. Let us consider the case of study in Figure A.1. We assume that material properties of water and substrate are known. The goal is to retrieve the thickness of the coating. The currently available methods are capable to do that under the hypothesis that the sound velocity in the coating is known. But in different practical scenario both the coating thickness and the longitudinal velocity are unknown, so the need of simultaneous estimation of these features [139].

In [140], the analytic expression for the complex reflection coefficient at normal incidence is derived

$$R = \frac{R_{12} + R_{23}exp(2ik_{2z}d)}{1 + R_{12}R_{23}exp(2ik_{2z}d)} \tag{A.5}$$

where R_{12} and R_{23} are the reflection coefficients at interfaces 1 and 2 of Figure A.1, d is the coating thickness and k_{2z} is the (eventually complex) wave number.

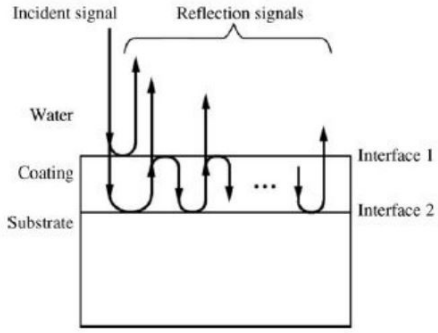

Figure A.1: Coating on a certain substrate immersed in water.

The reflection coefficients R_{12} and R_{23} are assumed to be known and they can be expressed as

$$R_{12} = \frac{\rho_2 c_2 - \rho_1 c_1}{\rho_2 c_2 + \rho_1 c_1} \tag{A.6}$$

$$R_{23} = \frac{\rho_3 c_3 - \rho_2 c_2}{\rho_3 c_3 + \rho_2 c_2} \tag{A.7}$$

The subscripts 1, 2 and 3 denote water, coating and substrate, respectively. ρ is the material density and c the longitudinal velocity. We assume that ρ_1, ρ_3, c_1, c_3 are known. The measured quantity is the magnitude of R, that is

$$|R(f)| = \sqrt{\frac{(R_{12} + R_{23}exp(-2\alpha d))^2 - 4R_{12}R_{23}exp(-2\alpha d)sin^2(2\pi f c_2/d)}{(1 + R_{12}R_{23}exp(-2\alpha d))^2 - 4R_{12}R_{23}exp(-2\alpha d)sin^2(2\pi f c_2/d)}} \tag{A.8}$$

with

$$k_{2z}(f) = \frac{2\pi f}{c_2} + \alpha(f). \tag{A.9}$$

From the above equations, it is easy to identify the physical quantities influencing the measured quantity, i.e.

$$|R(f)| = g(f, c_1, c_2, c_3, d, \alpha, \rho_1, \rho_2, \rho_3). \tag{A.10}$$

Table A.1: Dimensional variables in multi-layered material reflection. We denote with M, L and T mass, length and time, respectively.

Number	Parameter	Symbol	Fundamental dimensions
1	frequency	f	$[L^0M^0T^{-1}]$
2	density of first medium	ρ_1	$[L^{-3}M^1T^0]$
3	density of second medium	ρ_2	$[L^{-3}M^1T^0]$
4	density of third medium	ρ_3	$[L^{-3}M^1T^0]$
5	velocity in first medium	c_1	$[L^{-1}M^0T^{-1}]$
6	velocity in second medium	c_2	$[L^{-1}M^0T^{-1}]$
7	velocity in third medium	c_3	$[L^{-1}M^0T^{-1}]$
8	attenuation coefficient	α	$[L^{-1}M^0T^0]$
9	coating thickness	d	$[L^1M^0T^{-1}]$

Table A.2: Fundamental dimensions from monomial products of the repeating variables.

Product	Dimension
$1\ /\ \alpha$	[L]
$1\ /\ f$	[T]
$\rho\ /\ \alpha^3$	[M]

A.3 Application of the Buckingham's π theorem in this case study

In order to apply Buckingham's π theorem, the first step is to identify the repeating variables. The physical quantities involved are listed in Table A.1 with their fundamental dimensions. We choose as repeating variables α, ρ_1 and f.

They represent a feasible choice because the fundamental dimensions can be expressed in term of monomial products of the repeating variables (see Table A.2), the repeating variables are independent, arbitrary nontrivial monomial products do not generate dimensionless quantities, indeed, the kernel of the matrix

$$\begin{bmatrix} -1 & 0 & -3 \\ 0 & -1 & 0 \\ 0 & 0 & 1 \end{bmatrix}$$

made by the coefficients of the foundamental dimensions for the repeating variable is $\mathbf{0}$. Finally, they are not depending variables.

Table A.3: List of π groups for the case of interest.

Dimensionless groups		
$\pi_1 = \frac{\alpha c_2}{f}$	$\pi_2 = d\alpha$	$\pi_3 = \frac{\alpha c_1}{f}$
$\pi_4 = \frac{\alpha c_3}{f}$	$\pi_5 = \frac{\rho}{\rho_1}$	

Let us define $\rho = [\rho_1, \rho_2, \rho_3]$, the π groups obtained are the listed in Table A.3. Since π_3, π_4 and π_5 are known, we can write:

$$R(f) = g(\pi_1, \pi_2) = g(\frac{\alpha c_2}{f}, d\alpha). \tag{A.11}$$